Measurements and modelling of the tidal salt intrusion along the Waihou River

A thesis

submitted in partial fulfilment

of the requirements for the degree

of

Master of Science (Research) in Earth Sciences

at

The University of Waikato

by

Brooke James

KO TE TANGATA

THE UNIVERSITY OF
WAIKATO
Te Whare Wānanga o Waikato

2024

Abstract

Salt intrusions can exist within rivers and are influenced by shape of an estuary and tidal and river flows. Incoming tidal water moves into a region of freshwater influence which can have a strong influence on biological and geochemical properties in the water column. These features constitute a transition zone with spatially and temporally varying dynamics. As such, it is challenging to correctly represent these features in numerical hydrodynamic and sediment transport models. We report field observations of the salt intrusion processes in the Waihou River estuary in New Zealand. Most of the research that has been conducted thus far on the Waihou River has centred around sediment transport, gold mining impacts, water quality and fish populations and there is a lack of systematic collection of vertical water property data. Measurements of water column properties (salinity, temperature and turbidity) were taken at different tidal stages and river flows and used to track the movement and characteristics of the salt intrusion. In-situ water samples were collected and used to form a calibration for suspended sediment concentrations. The salinity intrusion was observed to intrude to 7.2-11.8 km (at 1 PSU) upstream from the mouth of the river. The estuary exhibited both mixed and stratified conditions, with a clear salt wedge shape observed for only one out of five surveys. The salinity intrusion length appeared to be primarily controlled by the by river flow, with a shorter intrusion length and stronger stratification occurring for higher river flows. Greater turbidity was observed within the marine water compared to fluvial waters, and turbidity was greater near the bed implying that the primary delivery mechanism of sediment to the lower reaches of the river is import from the offshore or intertidal marine regions. Numerical hydrodynamic modelling using Delft 3D was undertaken and was compared to the field data. While the model had previously been calibrated for water levels and velocity in two-dimensions, the adapted 3D version of the model did not accurately predict the structure or extent of the salinity intrusion. Model results under-estimated the salinity intrusion, which was attributed to over-mixing of the water column, however, the performance improved when a lower value for horizontal eddy diffusivity was used. This work emphasises the need to obtain vertically resolved data sets to allow for robust calibration of numerical models, which are commonly used in environmental management decisions.

Acknowledgements

The long road to finishing my thesis has come to an end, without the support of many, this would not have been possible.

I would like to express my gratitude to my supervisor Dr Julia Mullarney, thank you so much for all your help, wisdom and support on this journey to completing my masters.

I would also like to extend my appreciation to Dr Stephen Hunt for assistance on the project and the numerical model.

I am thankful to Waikato Regional Council for funding this project, and I also would like to acknowledge the financial support I received from the Broad Memorial Fund.

I would also like to thank the field technicians and boat skippers, particularly Holly Fergusson, Bonnie Lewis, Katherine Rowe, Warrick Powrie and Ben Roche for their assistance in collection of the field data. As well as Chris Eager for help setting up instruments.

Big thanks to my fellow students and friends including Shahab and Nicole who gave up their time to assist with collection of the field data, and Vinay and Dr Bérengère for helping with coding and modelling when I needed it.

Lastly, a special thanks to my lovely family, amazing friends Starsha and Charlotte, and my kind and helpful partner Nico, for all supporting me throughout this process, I am very appreciative of your kindness and encouragement. I couldn’t have done this without you all.

Table of contents

List of figures

List of tables

Chapter 1: Introduction

1.1 Background

1.1.1 Fluvial to marine transition zone

The Fluvial to Marine Transition Zone (FMTZ) occurs where a river meets the coastal ocean. The FMTZ is a dynamic region, which is subject to both marine and riverine forcing processes. These processes influence flows, mixing, salinity structures, and sediment transport and deposition (Gugliotta et al., 2017; La Croix et al., 2019). The FMTZ can extend upstream from the river mouth for up to hundreds of kilometres in large rivers, e.g. ~100 kms in the Fraser River, British Columbia, western Canada (La Croix & Dashtgard, 2015), or ~400 kms in the Fly River, Papua New Guinea (Dalrymple et al., 2003). Similarly, the region of freshwater influence can also extend seawards in deltas, thus affecting sedimentation and marine processes offshore, in some cases up to hundreds of kilometres, e.g. ~102 km seawards of the Mekong River, Southeast Asia (Gugliotta et al., 2017; Loisel et al., 2014). The extent of the area affected depends on the relative strength of the tidal and fluvial processes. Note the FMTZ denotes the region in which flows and processes are still affected by cyclical motion of tides; however, the extent of the salt intrusion upriver is typically much shorter.

The FMTZ and adjacent estuarine regions are commonly areas where humans interact strongly with the environment. Two thirds of major cities around the world are built around estuaries, modifying and impacting the estuaries and their hydrodynamic regimes (McKeon et al., 2020). In general, estuaries are sediment traps characterised by high rates of deposition of fluvial and marine sediments, and therefore contain a lot of nutrients and organic matter, creating a productive environment. The tidal influence combined with mixing between fresh and salt water creates biodiverse unique habitats and ecosystems. These ecosystems can act as a buffer for storm surges, and can be used by Māori and surrounding communities for many purposes including transport and recreation (Barbier et al., 2008; Costanza et al., 1997).

1.1.2 Dynamics within the FMTZ

Flows within the FMTZ close to the river mouth can fall within several classifications based on the salinity stratification within the estuary or river. The intrusion of the salinity landwards through an estuary is influenced by depth and width of an estuary and river system. Salinity structures help to define different estuary types as stratification controls the mixing of water types, salinity, sediment, nutrients, and pollutants (McKeon et al., 2020). The different regimes can be broadly classified by the ratio of the volume of river input (R) to the tidal volume (V) exchanged over a tidal cycle. For larger values of this ratio (>1), a salt wedge can form. As the salt water intrudes up the river, the freshwater flows above the salt water as the salt water is denser than the fresh water, gravity acts on the difference in densities, creating a wedge-like shape (Geyer & Farmer, 1989; McKeon et al., 2020; Poggioli & Horner-Devine, 2015). A strong halocline separates the freshwater layer and the saltwater layer and acts as the interface between these two layers (Kurup et al., 1998). In order for the salt wedge shape to be maintained, the river discharge must be strong enough to force a strong gradient between the two water types, maintaining the stratification against the tidal mixing and wind induced turbulence (Geyer & Farmer, 1989; Krvavica et al., 2021). At the point when a salt wedge is arrested, the inertial and frictional forces balance the baroclinic pressure gradient, allowing the interfacial structure to hold a semi-steady shape (Geyer & Farmer, 1989).

Flow within the salt wedge system is subcritical during flood tides, as the bottom flow is directed landwards, and the tidal flow and bathymetry interacts in such a way as to create pronounced transient forcing of stratified flow. During this time, the pycnocline is steady and there is little interfacial exchange. The baroclinic pressure gradient influences the maximum velocity difference during subcritical flows. During ebbing tides, the flow can be supercritical as the tidal currents reinforce average outflow from an estuary, meaning that the flow velocity is larger than the wave velocity as the bottom flow is directed back out to sea. Supercritical flow increases shear instability which leads to considerable vertical mixing, with the strength of mixing influenced by bottom friction. As shear increases during ebb flow and the flow becomes supercritical, the salt wedge shape collapses to a mixed or partially stratified estuary (Geyer & Farmer, 1989).

For smaller values of the ratio of river to tidal volumes, a mixed estuary may form, either partially mixed (intermediate R/V ratios) or well-mixed (for small R/V ratios). The partially mixed estuaries exhibit both vertical and lateral stratification, while well-mixed estuaries only show significant lateral stratification. In both cases the strength of the density gradients is controlled by shear, turbulence and vertical mixing. Overall, lower river flows and strong tidal currents result in weakly stratified intrusions (Krvavica et al., 2021).

Salt intrusions are also connected with the estuarine turbidity maximums (ETM). The ETM is where a peak in suspended matter and sediments is found in meso-, micro-, and hyper- tidal estuaries (Manning et al., 2010) which typically occurs in brackish water close to the head of the salt intrusion. Tidal conditions influence the formation of ETMS. Residual gravitation circulation dominates during neap tides when estuaries are stratified. Horizontal tidal currents and tidal asymmetry dominate during spring tides. Asymmetry may be caused by the bathymetry and topography of an estuary which leads to distortion of the tidal curve. The tidal asymmetry causes transport of sediments into the estuary, also known as tidal pumping. Tidal pumping is more significant than residual gravitational circulation (Manning et al., 2010). The ETM is maintained by the interaction between tidal pumping, and sediment settling and re-entrainment during the tidal cycle. The location of the ETM is controlled by tidal conditions and the magnitude of tidal pumping (Manning et al., 2010). A second ETM can also exist in the lower end of an estuary. The second ETM can be short-lived or semi-permanent and is correlated with different trapping mechanisms, such as deep-water areas which trap fine sediments during ebb tides, with spring tides re-suspending the deposited sediments. Sediments can also be deposited on intertidal flats, trapping more sediments between tides (Manning et al., 2010).

1.1.3 Ecological implications

The pycnocline acts as a barrier for mass transport, therefore, the bottom salt layer is isolated from the top fresh layer and mixing between the top and bottom of the water column is less likely to occur. This barrier then influences the distribution of chemicals, biological variables and affects water quality. Ecologically, the salt wedge or intrusion can act as unique habitat for fish species and aquatic organisms as this physical barrier prevents eggs, larvae, and juvenile fish from entering the freshwater layer and transporting back to sea, thus, the eggs and larvae are retained within the estuary (Victoria Government Department of Sustainability and Environment, 2008). Similarly, oxygen is not mixed into the bottom layer, often resulting in anoxia in the bottom layer. Additionally, sediment can also be transported upstream, contained within the bottom landward moving layer, carrying marine sediments further upstream (Kurup et al., 1998). This transport may result in smothering of bottom dwelling organisms, and affect light penetration to the floor, thus, affecting water quality.

1.1.4 Introduction to the Waihou River

The Waihou River is located in the North Island of New Zealand. An example of a FMTZ within in New Zealand can be found in the first 15-20 kms from the mouth of the Waihou River. The name of the Waihou stands for “fresh water” or “newly formed river”, also named “Thames” by Captain Cook until the 1940’s when the river was officially named Waihou (Land Information New Zealand, n.d.; Schofield, 1966). The Waihou River starts in Putāruru and flows through the Hauraki Plains, alongside the Kaimai ranges, and debouches into the Firth of Thames. The estuary that exists at the Waihou river is a river mouth estuary under category B – tidal river mouth (NIWA, 2007). Category B estuaries have simple shapes and are subtidal. The volume of river flow is usually greater than the tidal volume entering the estuary, therefore these estuaries are usually well flushed. When category B estuaries are deep, an estuarine circulation pattern can develop, balancing the outflowing freshwater with the inflowing seawater entraining beneath the freshwater, creating a salt wedge (Hume et al., 2007). The mouth of the Waihou River estuary is 700 m wide (Schueder et al., 2017).

The majority of the research and past investigations on the Waihou River have examined the suspended sediment transport and deposition (Roche, 2022) and fish population studies (Fish & Game Auckland/Waikato, 2022; NZ Fishing, n.d.) within the river, and influences of activities such as goldmining and the impacts on the river water quality and sediments (Ahmed, 2020; Clement et al., 2017; Webster, 1995). There exist some studies which obtain water property data by the Waikato Regional Council; however, as noted in Schueder et al. (2017) there is a lack of systematic studies of vertically resolved water property data such as salinity, temperature, and turbidity.

1.1.5 Knowledge gaps

As noted above, there exists limited knowledge about the characteristics and dynamics of the intrusion of sea water into the Waihou River. In particular, the variability of the vertical structure of flows within the river across the full range of river flows and tidal conditions is not well established, for example, it is unknown whether a salt wedge exists on any or all of the tides, or the proportion of time in which the river is partially or well-mixed. These data gaps need to be resolved to determine whether a numerical model of the system should be 2D or 3D in order to accurately predict the structure and extent of the intrusion of marine water. Moreover, it is necessary to correctly represent the dynamics under present forcing conditions before considering how the system may respond to changes under climate changes scenarios.

1.1.6 Research aim

The primary aim of this thesis is to explore and explain the dynamics of the salt intrusion within the Waihou River. The work will fill in a crucial data gap by presenting measurements of water column properties such as temperature, depth, salinity, and turbidity/suspended sediment concentration across a number of surveys and different conditions. The data will be used to track movement and characteristics of the salt wedge and/or salinity intrusion along the Waihou River. The data will then be compared to predictions from a numerical model of the region to provide an indication of model performance. The work will also investigate the sensitivity of model predictions to a range of numerical parameters.

1.1.7 Thesis structure

This thesis is comprised of five chapters; this first chapter starts as a general introduction to the thesis. A literature review of the study area is presented in Chapter 2, providing more context on the site-specific setting and some information from past investigations in these areas. The third chapter comprises the field, laboratory methods and the setup of the numerical model. The fourth chapter presents the results of the field measurements, laboratory and data analysis, and numerical model runs. Finally, the results are discussed and summarised in Chapters 5 and 6, respectively, along with recommendations for avenues of future research.

Chapter 2: Literature review of field site

2.1 The Firth of Thames

The Firth of Thames (FOT) is a shallow marine meso-tidal embayment in the North Island of New Zealand (Figure 2.1). The FOT is about 800 km^2 and 35 m deep at the deepest part towards the north end (McLeod et al., 2012). The FOT experiences mixed semi-diurnal tides and tidal current speeds are usually less than or equal to 0.2 m.s^{-1} on the intertidal flats. Opposing southwest and northeast winds drive residual circulation in both clockwise and anticlockwise directions. The northerly winds create small waves which affect the intertidal mudflats. Due to the large tidal range and estuarine processes trapping the large sediment input from the rivers, extensive intertidal mudflats have formed, with an area of 70 km^2 and width of 5 km, located in the southern end of the FOT (Swales et al., 2015).

The Thames climate is classified as Cfb according to the Köppen–Geiger climate classification which is also known as an oceanic climate and is humid and temperate. This geographic setting means there is generally cool summers and mild winters with a narrow temperature range. The average annual rainfall for the FOT is 1,141 mm, the wettest month is July, and the driest month is January, with monthly averages of 148 mm and 65 mm, respectively. The median annual temperature is ~14-15 ^{o}C with a median of ~24 ^{o}C in summer and a median of 5-6 ^{o}C in August, based on the 1981-2010 normal period (Chappell, 2013).

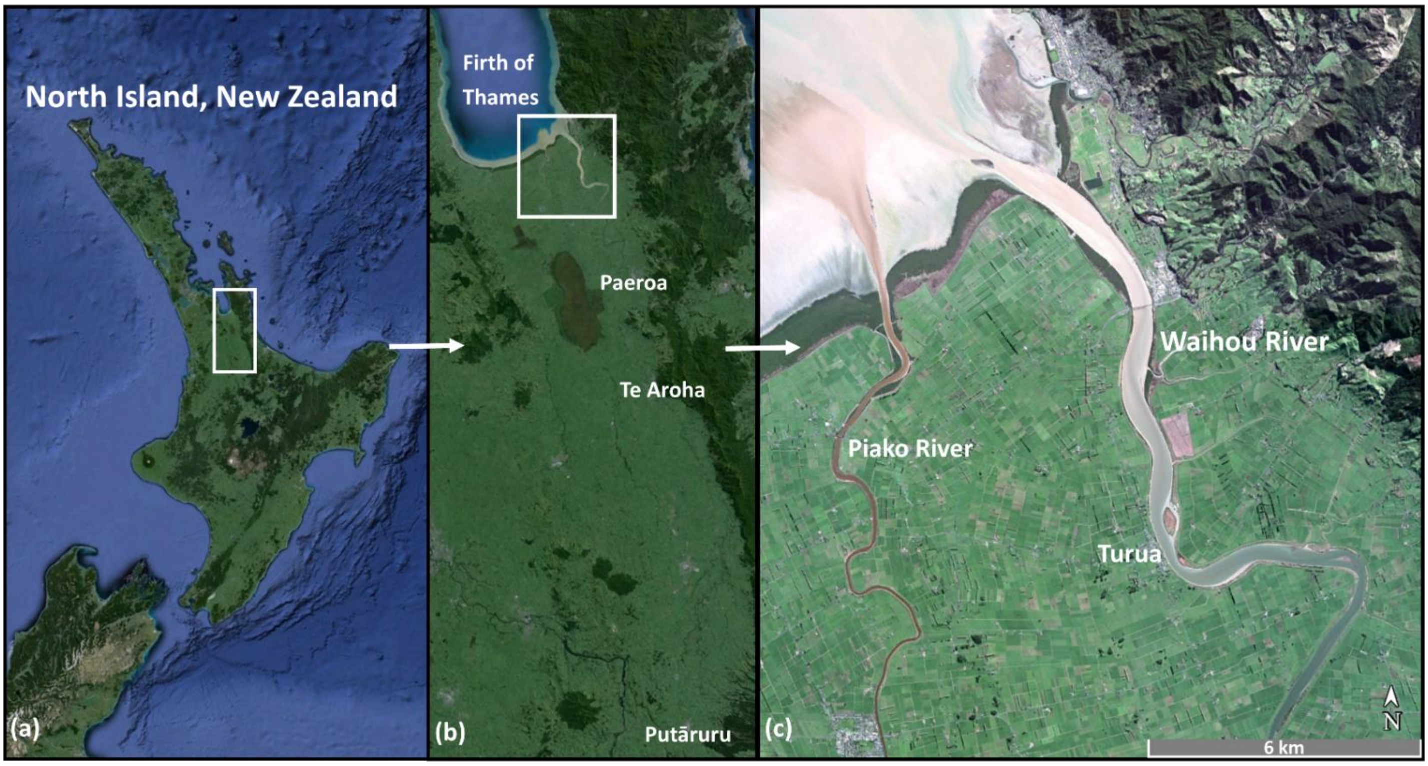

Figure 2.1: Location of the study site relative to New Zealand Aotearoa (a). Key towns located near the river (Puke bridge is located at Paeroa) (b), and the Waihou River estuary (c). Images from Google Earth.

2.2 Sediment input into the Firth of Thames

The FOT receives most of its sediment from the Piako River and the Waihou River. The sediment type coming from these rivers are fined grained terrestrial sediments that come from agricultural lands in the Hauraki catchment which has an area of 3,600 km^2. The sediment input into FOT creates a turbidity gradient, with the most turbid water in the southern area and the least turbid in the northern area (McLeod et al., 2012). The Waihou River has been delivering sediment into FOT for 20,000 years, the Waihou and Piako Rivers deliver a combined total of ~190,000 t of sediment per year (Hicks et al., 2011).

Estuarine circulation traps the suspended sediment coming from the rivers inside the FOT (Swales et al., 2007). As a result of sediment trapping, the shoreline near the mouth of these rivers has been prograding for the last 6,500 years and has a progradation rate of 1.7 m per year (Swales et al., 2007). Mangroves stabilize sediments, enhancing mud accumulation, an expanding mangrove habitat at the FOT and Waihou River may contribute to the progradation of the shoreline. The mangroves cover 11 km^2 of a former intertidal mudflat, extending 1 km seaward of the shoreline that existed in 1952. The Hauraki catchment was covered in podocarp-hardwood forests and freshwater marshes and Kahikatea forests before humans arrived. Once Māori arrived, riverbank forests were cleared and once Europeans arrived, there were huge amounts of deforestation and gold mining, and logging was common in the Coromandel. Due to the land use changes and the reduction in land cover in the Hauraki catchment, sediment load into the FOT increased (Swales et al., 2007).

The fine sediment input into the FOT creates negative impacts on organisms such as Green-lipped mussels, which used to inhabit the FOT before dredge fishing from 1910-1968 removed their reef habitat. Since then, this species has struggled to repopulate due to loss of habitat. The increase in sediment has contributed to changes in sea floor type to being more muddy and decreasing the water quality. These environmental changes have resulted in the mussels having slower growth rates and poorer health conditions than mussels in other regions around New Zealand (McLeod et al., 2012). Increase in sedimentation to the FOT has also produced large intertidal flats perfect for mangrove habitat, and indeed, mangroves have expanded rapidly in the FOT for the past 70 years (Horstman et al., 2018). While mangroves do provide fish habitats and increase water quality, the presence of trees promotes a change in the substrate from sandy to muddy which causes biodiversity loss as well as changing of benthic community structures (Horstman et al., 2018).

2.3 Waihou River and geochemical processes

The Waihou river is 175 km long (Statistics New Zealand, 2006), and is fed by many tributaries from the Kaimai ranges with a catchment area of 1,977 km^2 (Waikato Regional Council, n.d.). The Waihou River begins in Putāruru, where the stream is fed by ground water (Schueder et al., 2017). The river starts small and water quality is good in the upper reaches. The river flows through mostly farmland and wetland areas, and widens downstream, with many small towns located near the river (Figure 2.1 and Figure 2.2). The catchment consists of mainly pasture and agricultural (58% of total land use) land-uses and some urban areas, including indigenous and planted forests (37% of total land use) in the upper reaches of the river (Schueder et al., 2017). Towns that are within the river catchment includes Putāruru, Te Aroha, Paeroa, Thames, Matamata, and Turua (Waikato Regional Council, n.d.). The river drastically widens 10 km upstream from the mouth of the river and water quality decreases downstream until the river eventually flows into Firth of Thames.

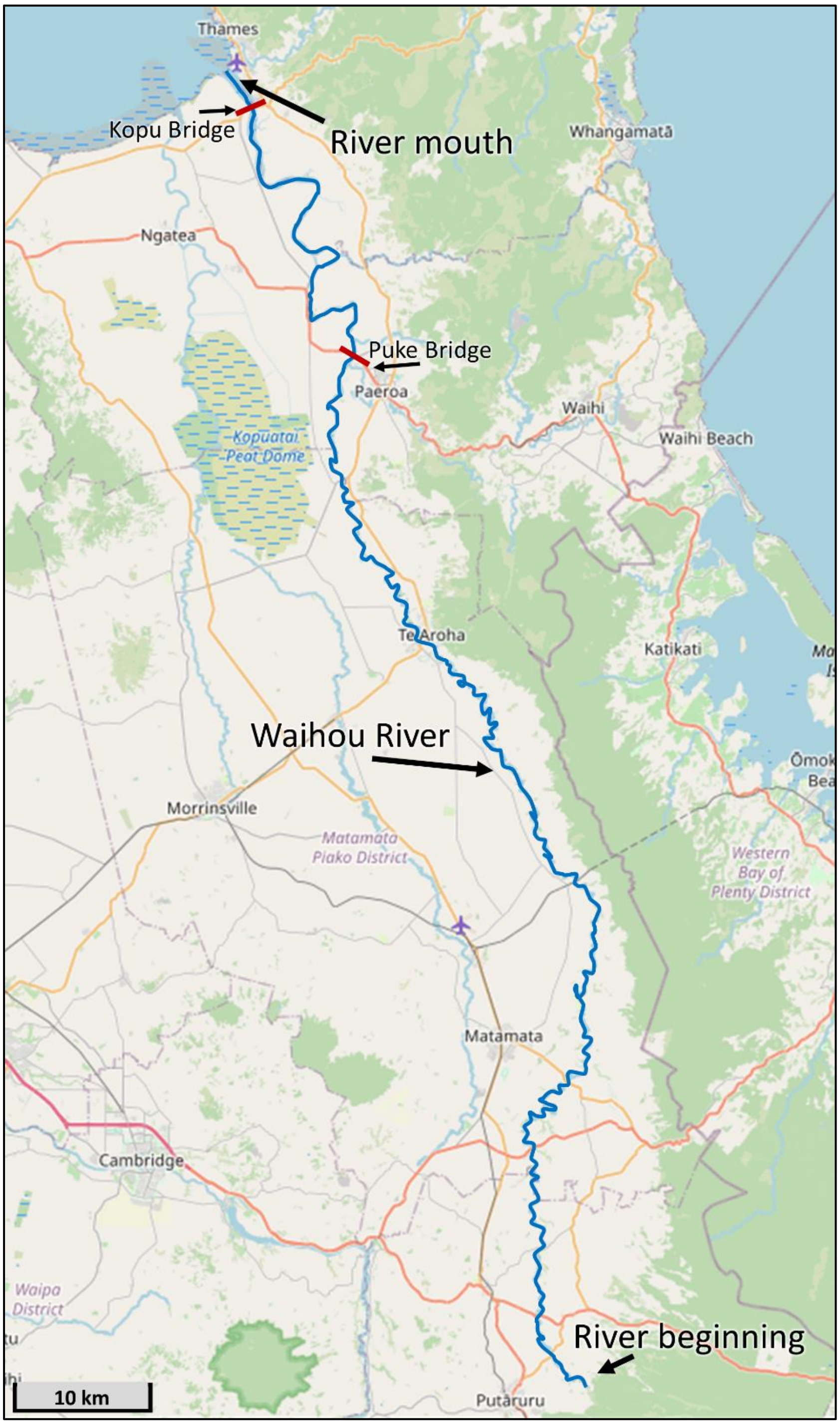

Figure 2.2: Map of the entire Waihou River, map image sourced from https://www.topomap.co.nz/

The estuary area of the river is also where the river is the deepest. The river is used for recreational purposes such as fishing. Aquatic life such as Rainbow Trout and Whitebait can be fished during Whitebait season from October to November at the mouth of the river (Fish & Game Auckland/Waikato, 2022). Whitebait are juvenile fish from 6 different species, also known as migratory galaxiids (Department of Conservation, n.d.). Other common aquatic species that can be found in the Waihou River are eel, flounder, mullet, sharks, and snapper.

The water quality has been influenced by many processes, such as uses of surrounding land and activities including urban, farmland and goldmining. The gold rush during the 1860s and 70s resulted in goldmine tailings entering the Waihou river which are potentially toxic to aquatic life. The Ohinemuri river is a tributary that feeds into the Waihou River near Paeroa, mining by product was discharged straight into the Ohinemuri, unrestrained from 1875 to the 1950s (Ahmed, 2019; Clement et al., 2017; Webster, 1995). The discharges contained mercury, cyanide, copper, zinc, manganese, lead, and arsenic (Ahmed, 2019; Clement et al., 2017). Silt built up along the channels as a result, narrowing the river channel. Due to the constricted channel, floods occurred regularly, deposited mine tailings into surrounding floodplains and farmland. In 1910 the government started a control programme, reducing the use of the river as a sludge channel. A large flood in 1907 deposited a layer of yellow-brown mine tailings over the flood plains, which contained high concentrations of metals such as Lead (Pb), Arsenic (As), and Copper (Cu) (Clement et al., 2017). By 1910 there was an estimated 2,200,000 Mg of mine waste within the riverbed. The heavy metals pose a moderate risk to aquatic organisms, especially in the Ohinemuri River and near the Ohinemuri and Waihou confluence. The metals are unlikely to be remobilised and transported all the way through to the FOT, unless there is another large flood such as the one that occurred in 1907 (Clement et al., 2017).

There are aquifers near the Waihou River such as aquifers Tauranga Group Sediments (21), Hinuera Formation (25), Coromandel Volcanic (26), and Coromandel Sand (27) (GNS Science, 2021) (Figure 2.3).

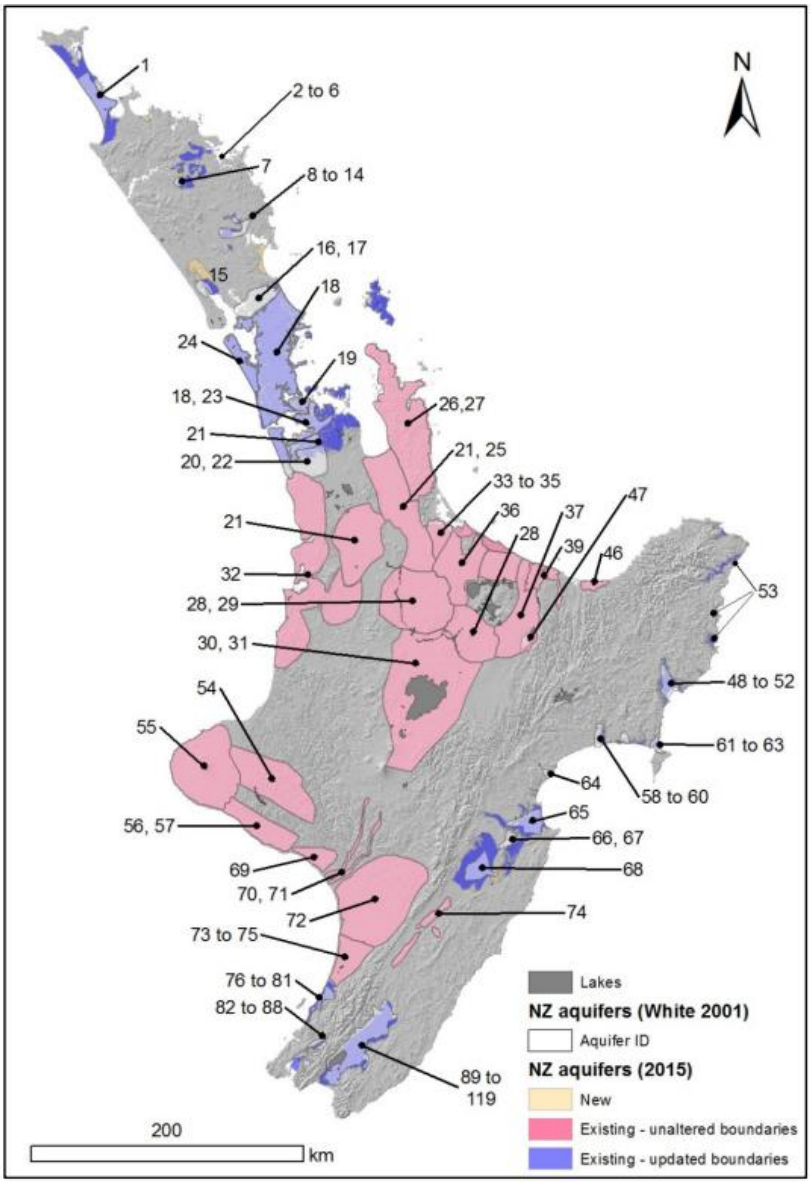

Figure 2.3: Map of the North Island of New Zealand, displaying location of aquifers. Figure from GNS Science, (2021).

Many communities near the Waihou River rely on groundwater for their fresh water supply, (the known bores in the vicinity are shown Figure 2.4). Increased demand of this freshwater source, especially over summer, poses a risk for saltwater intrusion into the aquifers. The aquifers in the Hauraki plains are recharged by rain fall on the Hauraki Plains (Waikato Regional Council, 2023). Sea level changes can cause changes in the positions of the fresh-salt water interface in confined aquifers, salt water can intrude into aquifers by lateral intrusion from the ocean, upward intrusion from deeper saline zones of groundwater systems, or by downward intrusion from coastal waters such as estuaries (Barlow & Reichard, 2009).

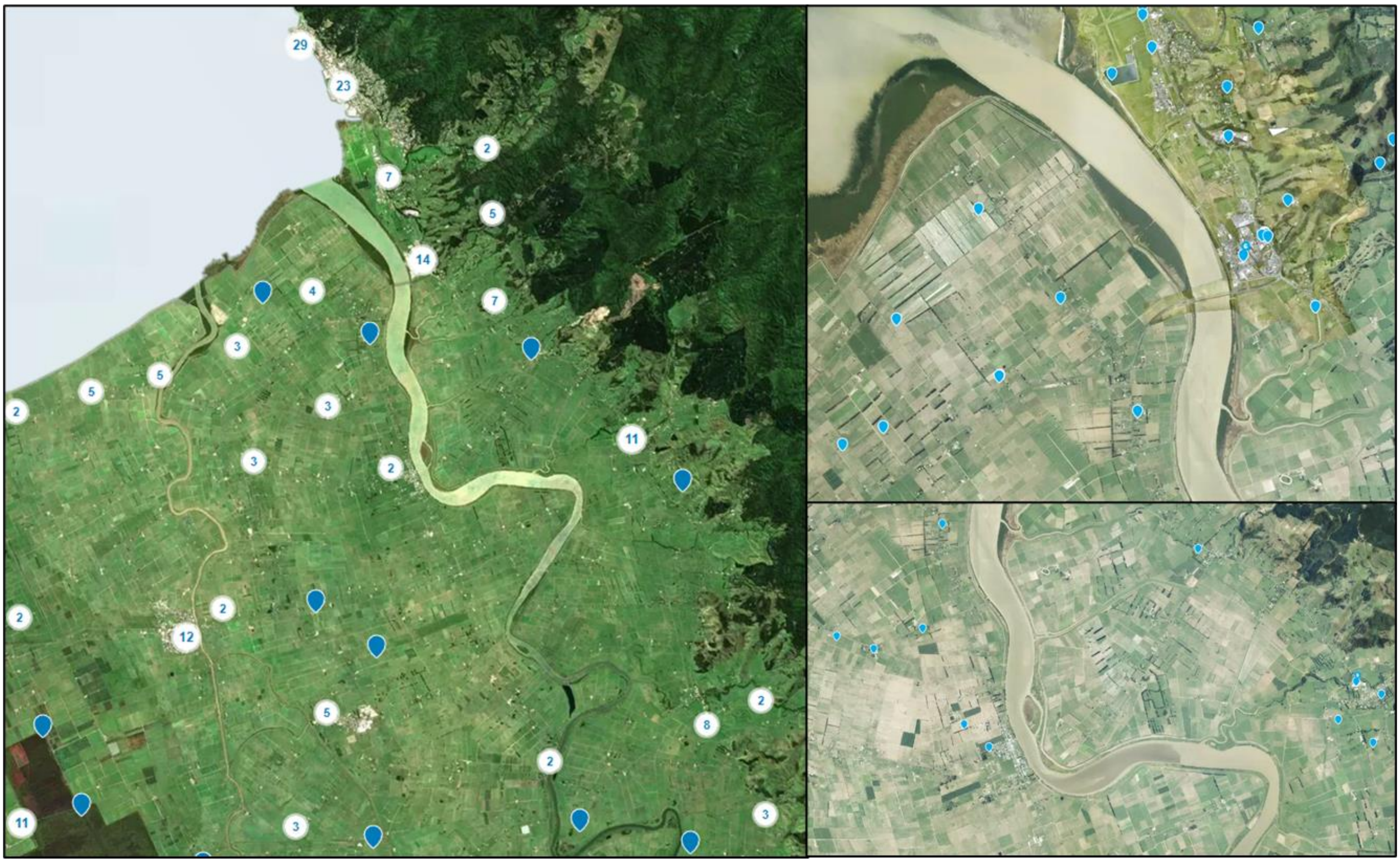

Figure 2.4: Bores located near the Waihou River (blue and white markers) retrieved on January 5th, 2024, from Wells Aotearoa New Zealand (https://wellsnz.teurukahika.nz/wells/map).

2.4 Previous data sets and investigations

In this section, we report results from four key studies exploring hydrodynamics, water quality, sediment transport and morphology of the Waihou River and surrounding floodplains. These studies further underscore the knowledge and data gaps. The report *Climate changes, impacts and implications to NZ, case study on Firth of Thames and Lower Waihou River, by McBride et al., (2016),* aims were to improve climate predictions, and understand and identify key steps, limitations, responses, and options for mitigation. The report focusses on the lower Waihou River and the Firth of Thames, using 3D hydrodynamic and sedimentation models as well as a mangrove cover model (McBride et al., 2016). The study *Piako and Waihou River estuaries – Deltares, Waikato Regional Council, by Schueder et al., (2017),* is an observational study focussing on water quality in estuaries. Both of the Waihou and Piako River estuaries were experiencing water quality problems, including high nutrients, low dissolved oxygen and botulism. The authors aimed to understand causes of these issues but found there was a lack of physical, chemical, and biological data on these estuaries, such as density stratification, estuarine circulation and transport, primary production, and sediment transport (Schueder et al., 2017). Therefore, the Waikato Regional Council looked to understand these fundamentals to aid in future management efforts in improving the water quality. The report uses previously published data sets on the estuaries, and continuous flow records from the Waikato Regional Council (Schueder et al., 2017). The thesis *Sedimentology and Hydrodynamic Trends in the FMTZ of the Waihou River, by Ben Roche., (2022)* aimed to take quantitative measurement of sediment deposits along the fluvial to marine transition zone (FMTZ) in the Waihou River, to look at how mud deposition is influenced by the FMTZ, mixing, flocculation, flow speed etc. The aims also included investigating how the mud deposits are preserved in deep vs shallow channels, and the diversity of mud facies across cross sections of the river. Roche wanted to discover if dynamically deposited mud can be observed in a sedimentary system and linked to flow processes, and if these processes can be used to constrain position of deposits along the FMTZ. Roche used oceanographic observations paired with sedimentological data that was collected from the channel within the FMTZ (Roche, 2022). The thesis *Distribution of mine waste along Waihou River Flood Plains, by Tofeeq Ahmed, (2020)* investigated floodplain contamination due to mine waste that entered the Ohinemuri River and Tui Stream, which are tributaries of the Waihou River, during mining periods between 1895 and 1910 and mapped metal concentrations in the Waihou river flood plain.

2.4.1 Hydrodynamics

McBride et al. (2016) used a 3D hydrodynamic and sediment model as well as a mangrove cover model to investigate the consequences of climate change on the lower Waihou River. These climate drivers included the effects of sea level rise, increases in wave height and storm surges, changes in air temperature, rainfall, and drought frequency. In particular, in New Zealand the sea level is rising 2.14 +/- 0.47 mm per year (McBride et al., 2016), and wave height and storm surges are predicted to increase by an order of 1-5%. Based on RCP8.5 (average of several climate models), the Waikato region may experience an increase in average air temperature, up to 3.3 ^{o}C in the summer, a change in average rain fall by +3 %^{2} in summer and -6%^{2} in spring, an increase in the occurrence of hot days (T_{max} > 25 ^{o}C) from 23.6 days/yr currently to 84 days/yr at the end of the century, a decrease in cold nights (T_{min} < 0 ^{o}C) from 15.3 nights/yr to 1.9 nights/yr at the end of the century, and an increase in dry days (< 1mm precipitation/day) by 5-10 days per year, an increase in 99th percentile rainfall by 5-10%, and a decrease in 99th percentile wind speed by 0-5%. Lastly, an increase in drought duration and intensity by 25-35% is also predicted (McBride et al., 2016).

The modelling predicted that for sea level rises of 1 m, the salinity in the Waihou River during flood tide would extend 5 km further upstream. The report concludes that the flow of the river does not have much effect on the salinity intrusion, with the main driver being sea level rise. River flooding modelling suggests that the Waihou River tidal limit would move 6 km further upstream with a 0.5 m sea level rise, while a 1 m sea level rise suggests the tidal limit would move a further 3 km upstream (McBride et al., 2016).

Similarly, a report by Schueder et al. (2017) explored two models that were built for regions that include the Piako and Waihou Rivers. The first model is a 3D hydrodynamic model for the Firth of Thames created by Knight and Beamsley (2013). The second model is discussed in the water quality section below. The Knight and Beamsley model (using a Semi-impilicit Eulerian-Lagrangian Finite Element model code) was calibrated and found that generally performed well but under-predicted high tide and over-predicted low tide. The majority of the current velocities were well predicted, with the exception of a systematic under-prediction at around 1 m above the bed. The model did not perform well in terms of salinity predictions at the mouths of the Piako and Waihou Rivers, with systematic over-predictions of salinity which were attributed to uncertainty with river discharge boundary conditions (Schueder et al., 2017). The report also noted a lack of observational data, in particular, salinity, velocity profiles, and bathymetry for further upstream (Schueder et al., 2017). More recent work by Roche (2022) showed that for observations of a 3-week duration, the salinity in the lower estuary varied from marine to fresh over each tidal cycle, while at 2.7 km upstream of the mouth, the saline intrusion only reached this extent during spring tides and lower river flows. In terms of velocities, peak flow speeds were seaward, with velocities decreasing landwards. Peak flow speeds were highest during flood tides on the seaward side of the estuary (marine dominated) and were fastest during ebb tides on the landward side of the estuary (fluvially dominated) (Roche, 2022).

Roche (2022) found that at 13.8 km upriver from the mouth, tidal fluctuations were 2.2-3.3 m above the bed, current velocities were 0-0.5 m.s^{-1}, maximum values occurred during storm water discharge and the currents were influenced by the tides. At 9.8 km upriver from the mouth, temperature was 16.25-20.5 ^{o}C, and salinity was >0.1-9.8 PSU. At 6.4 km upriver from the mouth, water levels were 2.33-2.55 m above bed level, current velocities were 0-0.6 m.s^{-1} and changed direction with the tidal cycle, outgoing speeds were slightly faster than incoming speeds. At 2.7 km upriver from the mouth, water temperatures were 16.85-22 ^{o}C, warm water came from the FOT and cooler (by 1^{o}C) temperatures from the fluvial waters, salinity ranged from 0.5-30.5 PSU, maximum salinity was during flood tides, current velocities were 0-0.8 m.s^{-1}, and speeds were faster during flood and slower during ebb. At the river mouth, water levels were 2.3-3.7 m, current velocities were 0-0.6 m.s^{-1}, and flood current velocities were greater than ebb current velocities.

2.4.2 *Water quality and contaminants*

A study by Schueder et al. (2017), used observations to examine water quality in the Piako and Waihou River estuaries from 2009-2015.

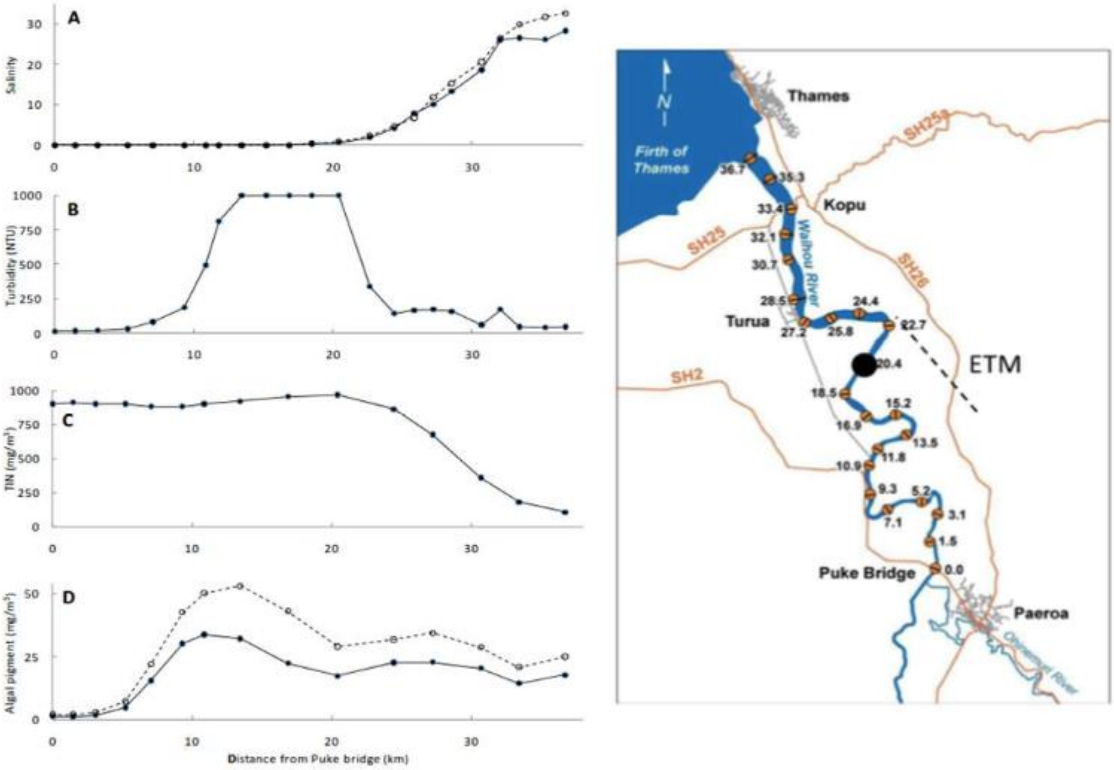

Figure 2.5: Figure from Schueder et al. (2017), showing measurements of salinity, turbidity, total inorganic nitrogen (TN), and algal pigment of the Waihou River estuary taken by Bill Vant 2011.

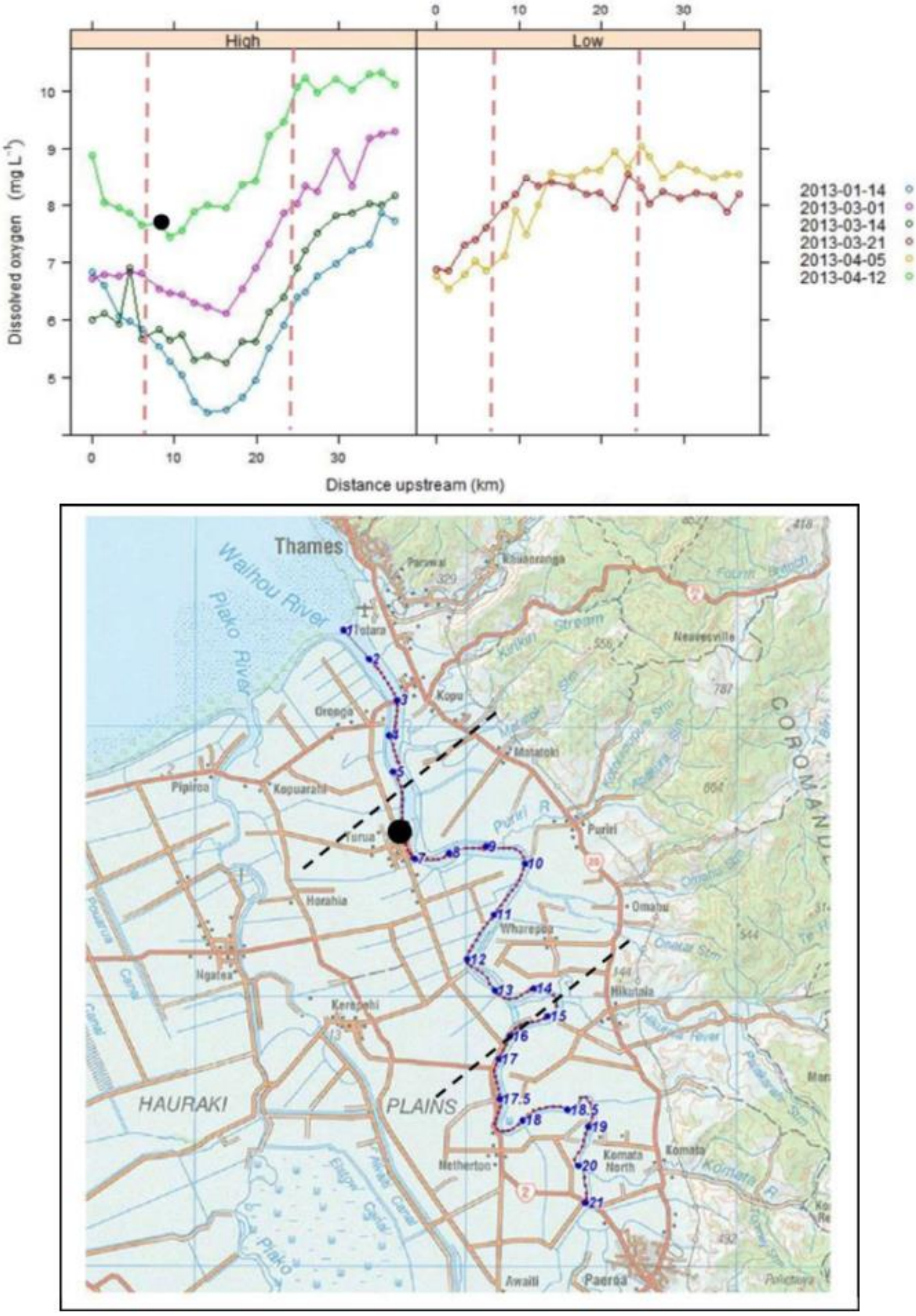

Figure 2.6: Figure from Schueder et al. (2017), showing dissolved oxygen measurements taken from sites along the Waihou River estuary by Franklin & Smith (2014).

The report by Schueder et al. (2017), noted that in an early set of measurements by Bill Vant, in 2009-2010, turbidity and algae content were found to be concentrated in the maximum turbidity zone.

Moreover, there were significantly low dissolved oxygen levels in sites near Turua and Warf Road while, the upstream reaches displayed high dissolved oxygen. These data were supplemented by measurements of the dissolved oxygen in the river in 2014 by Franklin and Smith. The authors found that dissolved oxygen levels were exceptionally low within the ETM (estuarine turbidity maximum), and that dissolved oxygen levels were lower during hightide compared to low tide. Average dissolved oxygen was continuously low throughout the summer months, even during low tide. During high discharge events, there was an increase in dissolved oxygen, with a dilution in turbidity and algae, and a decrease in temperature, with these changes attributed due to the mountainous environment within the catchment, as well as the groundwater input into the river (Schueder et al., 2017). Usually, tidal ranges and tidal lengths influence the intensity of the ETM in an estuary, with long tidal ranges having increased residence times, and larger tidal ranges reducing residence times in the ETM. Thus, it could be expected that the Waihou River estuary would have a weak ETM due to its short tidal length and meso-tide; however, in contrast, the reports results indicate that the ETM has low dissolved oxygen levels, lower than ecologically acceptable saturations and turbidity levels over 800 NTU (Schueder et al., 2017). Numerical modelling using a WFD-explorer model for the Hauraki Plains was conducted by Weeber et al. (2016). The results predicted TN (total nitrogen) and TP (total phosphorus) loads, with reasonably high degrees of similarity between predicted and water quality measurements. However, Schueder et al. (2017) concluded that the 1D model was not suitable for predicting transport of water quality constituents in the estuary owing to the 3D nature of the flows and stratification. Moreover, their report again emphasized that there was insufficient data to provide a more comprehensive understanding of the estuarine system.

Ahmed (2020) investigated mine waste within the Waihou catchment. The waste included metals such as Cu, Zn, Mn, Pb, and As and entered tributaries (designated as sludge channels) of the Waihou river from 1895-1910. Floods washed these metal contaminants into surrounding farmland destroying crops and grass paddocks, as well as destroying fish stocks down stream. However, Ahmed (2020) reported minimum migration downstream to the Firth of Thames as the contaminants are reduced in the downstream flood plains. The highly contaminated areas remained close to the initial sites, such as no further than Paeroa near the Ohinemuri river, and the output of the Tui Stream near Te Aroha (Ahmed, 2020). Another study on heavy metal contaminants from the goldmining era by Webster, (1995) collected measurements and samples in the Waihou River and tributaries to investigate trace metal contamination and transportation. Webster (1955) found that trace metals were transported within the Waihou catchment in dissolved and particulate form. In the Ohinemuri River and Tui Stream, trace metals were transported as dissolved metal ions and complexes or as bound to sediments. Cu, Pb, As, and Zn concentrations in sediments are higher in the tributaries than in the estuary. Mn and Cr found in the estuary is not derived from the tributaries. The metals measured were detected within the estuary, flocculation of the suspended sediments occurred due to higher pH and salinity in the sea water than the fresh water, leaving little dissolved Fe and Mn in solution. In the lower estuary it was found that Fe, Pb, and Zn entirely and Mn, As and Cu partially bound to suspended sediments, and as the sediments flocculate (aggregate) and settle to the estuary floor, the trace metal concentration in the bed sediments increases. Therefore, most of the metals that are transported to the estuary remain trapped unless removed by transport of sediments out of the estuary (Webster, 1995).

2.4.3 Sediment transport and morphology

McBride et al. (2016) climate change predictions for sediment transport discharging from the Waihou River into the Firth of Thames indicate that the sediment plume stays near the mouth of the river during calm weather, but when there are high winds, there is a greater dispersion of the sediment plume.

Roche (2022) found that at 13.8 km upriver from the mouth, suspended sediment concentrations (SSC) were above the maximum limit of detection (3 gL^{-1}) but reduced to 0.4 gL^{-1} during the ebb tide. The proportion of mud was greatest on the eastern bank and sand dominated the western bank. Mean mud proportion was 44.65% (Roche, 2022). At 9.8 km upriver from the mouth, the mud proportion was greatest in the mid channel bar and the base of the channel was sand dominated, the mean proportion of mud was 47.87% (Roche, 2022). At 6.4 km upriver from the mouth, SSC was between 14 and 0.5 gL^{-1} reducing at the end of the flood tide. The mud proportion was greatest along channel margins and the western bank, while the channel base was sand dominated. The mean mud proportion was 50.48% (Roche, 2022). At 2.7 km upriver from the mouth, SSC exceeded measurable values (greater than 3 .7 gL^{-1}) and decreased to less than 0.1 gL^{-1} when velocity was zero. The eastern channel margin had the greatest proportion of mud, most of the channel base was sand dominated. The mean proportion of mud was 36.49% (Roche, 2022). At the river mouth, SSC exceeded maximum values (greater than 18.6 gL^{-1}) but was more common to peak around 13 gL^{-1}, SSC decreased to 0.6 gL^{-1} when flow velocity was 0. The mud proportion was greatest along the southwestern channel margin, and most of the channel base was sand dominated. The mean proportion of mud was 34.93% (Roche, 2022).

Roche discussed that very large SSCs were observed up to 18 gL^{-1}, fluid mud was observed during slack tides. Peak mud content was found in the middle of the study area, the main mud type being thick structure less mud, resulting from fluid mud deposition. The distribution of the muds was linked to hydrodynamic processes, with muds being poorly preserved in the deepest parts of the channels. Mixing of water types at the upper estuary controls the flocculation of sediments, and that was the main driver for sediment depositions. In the lower estuary, sediment accumulation is limited by fast current velocities (Roche, 2022).

Chapter 3: Methodology: field measurements and numerical model set up

3.1 Field measurements

Field measurements were taken during five vessel surveys on the Waihou River (Table 3.1, Figure 3.1). Surveys were taken across different tidal stages. Surveys 1 and 4 were taken during the end of the flood tide and start of the ebb tide. For surveys 2 and 3, measurements were taken on the incoming tide, while for survey 5, measurements were taken on the outgoing tide. For the measurements on the incoming tide, a handheld sensor was first used at each position to verify that the progression of the saltwater upstream was captured. The surveys started from the river mouth and a vertical profile was taken at approximately every 500 m, for 10-12 km upstream, to cover the furthest landwards point of the salt intrusion at high tide. Following the change to ebb tide, a few further measurements were taken following the tide back towards the river mouth. For the measurements taken during the out-going tide, a similar process was followed, measurements were taken while travelling upstream every 500 m, starting 6,000m upstream from the mouth of the river, and then once the limit of the salt intrusion was reached, measurements were also taken while travelling back downstream. The vertical profiles were taken with a Seabird SBE 19plus V2 SeaCAT Conductivity-Temperature-Depth (CTD) Profiler, which measured conductivity, temperature, and pressure at 4 Hz sampling rate. A Campbell scientific OBS 3+ (Optical Backscatter Sensor) was attached to the CTD cage to measure turbidity at the same sampling rate. An YSI ExoSonde was also mounted on the same cage as the CTD. The ExoSonde measured conductivity, temperature, dissolved oxygen, pH, chlorophyll-a and turbidity at 4 Hz. The instruments were lowered slowly into the water and held at the surface for a minute to flush the CTD pump. The profilers were then steadily lowered until they reached the riverbed. In-situ water samples were also taken through a tube attached at the same vertical position as the OBS. Locations of the casts were provided by GPS.

The in-situ water samples were used to calibrate the OBS sensor to provide estimates of suspended sediment concentrations. Samples were filtered through pre-rinsed, dried and weighed microfibre glass filters papers at 47 mm diameter. Filters were subsequently dried (overnight at 105°C) and weighed to provide SSC in mg.L^{-1} for comparison with OBS values. Calibration results are shown in the appendix (Figure A.1 and Figure A.2) noting that in all cases the, fits of the calibration curves were excellent (R^2 >0.98).

3.2 Data processing and analysis

A digitised path along the centre of the river was created on Google Earth, and each cast location was mapped to the closest point on this centre path, to provide an along-river position, where 0 corresponded to the river mouth. Negative values for distance indicated locations in the main FOT, while positive values indicated distances upriver.

The profilers were continuously recording measurements while in the water column. Data processing for both CTD and ExoSonde data removed upcasts so only the downcast was retained. Data points near the surface (depths <1 m) were removed (as less than 1 m depth is where the CTD was held for pump flushing). Similarly, data points from cases where the profiler was clearly submerged into the bottom sediments were removed. Variables were then linearly interpolated to a regular grid at 5 cm depth increments. Conductivity was converted to salinity and density was calculated using the TEOS-10 toolbox (McDougall & Barker, 2011).

Figure 3.1 shows the locations and times of all casts for the five surveys (white circles). While multiple casts were occasionally taken at some sites, the sites were approximately 500 m apart. The furthest distance upstream was around 13,000 m from the river mouth in January 2023 (Figure 3.1). The tidal predictions were taken from a location close to Turua.

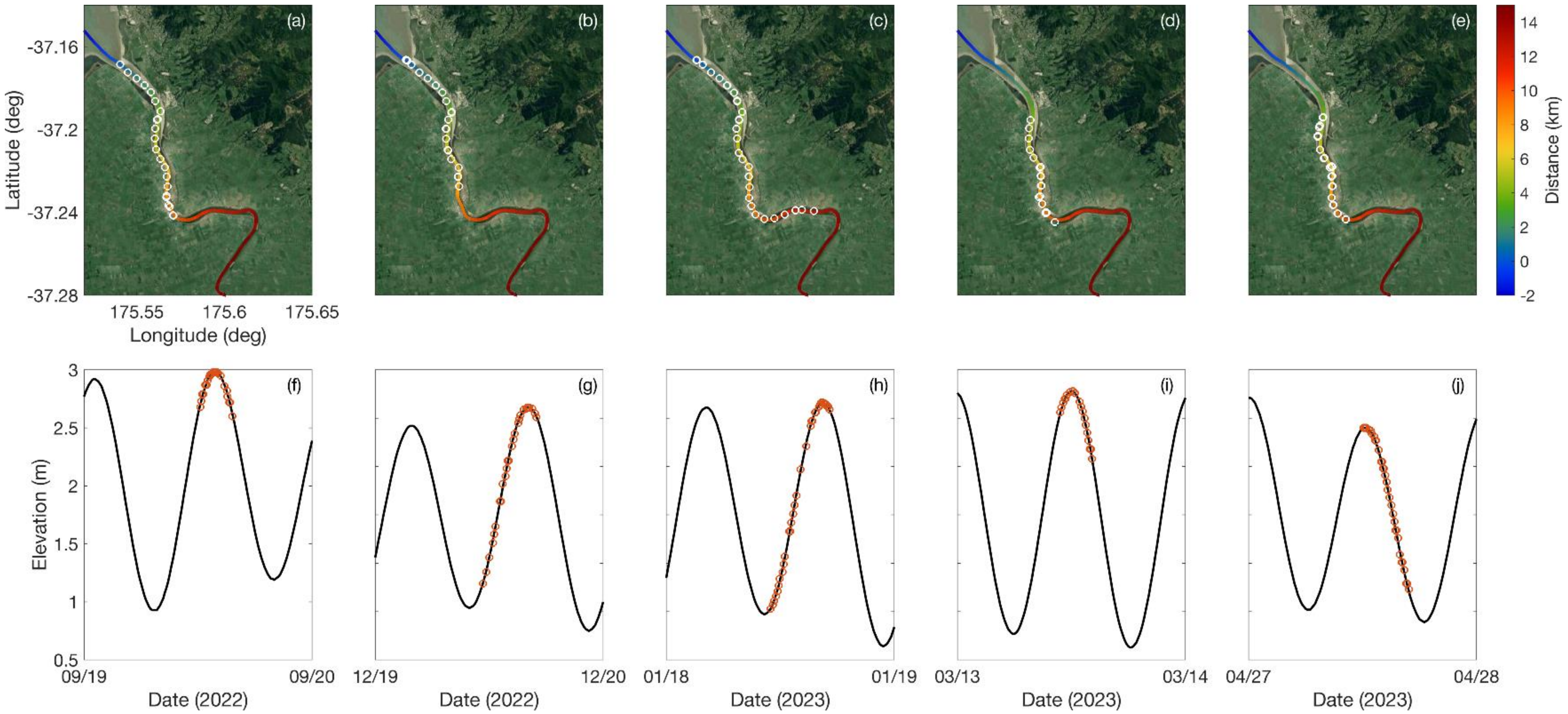

Figure 3.1: Top: Sites of profiles at the Waihou River on each field visit day superimposed on the colour coded distance from the mouth of the river. Bottom: sample times shown relative to the time in the tidal cycle. Tide predictions taken from Latitude -37.216, Longitude 175.565 between Kopu Bridge and Turua by NIWA https://tides.niwa.co.nz/.

Table 3.1: Times and dates for each field visit, including UTC time and tidal stage.

Survey	measurement time (NZ local time)	Tidal stage	Distance covered (m)	Number of casts taken
1	19/09/22 12:10 - 15:40	End of flood to start of ebb	0-10,000	24
2	19/12/22 11:20 – 17:00 (DST)	Incoming flood	0-8,000	27
3	18/01/23 10:55-17:15 (DST)	Incoming flood	0-13,000	33
4	13/03/23 10:50 – 14:10 (DST)	End of flood to start of ebb	4,000-10,000 Upriver 10,000-6,500 Downriver	19
5	27/04/23 12:05 - 16:55	Outgoing ebb	6,000-10,000 Upriver 10,000-4,000 Downriver	32

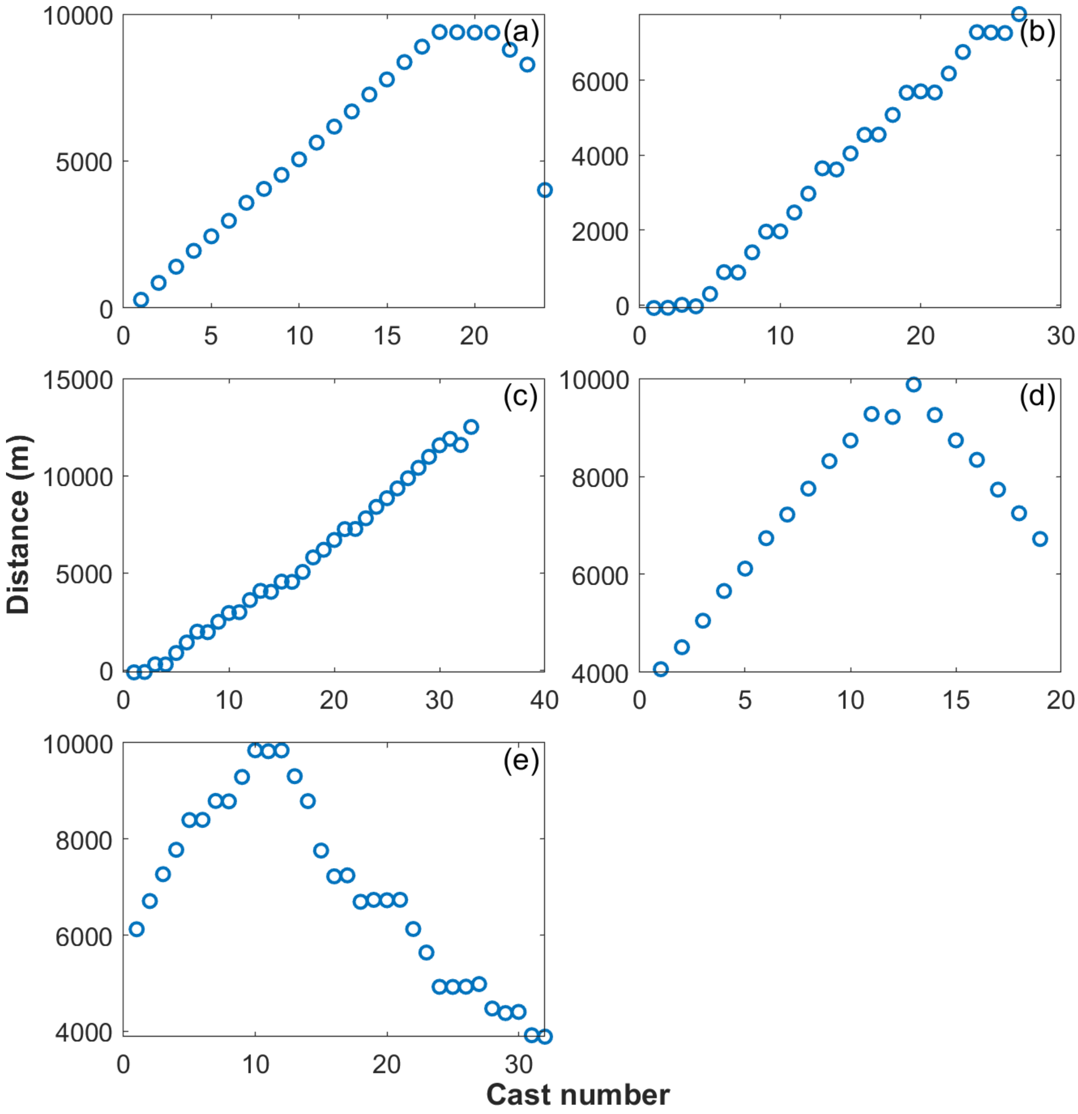

Figure 3.2: Distance along river of each profile, (a) CTD casts taken on 19th September2022, (b) casts taken on 19th December 2022, (c) casts taken on 18th January 2023, (d) casts taken on 13th March, (e) casts taken 27th April.

As shown in Figure 3.2, during the September field trip, casts were taken going upstream following the flood tide, then at about 9,000 m upstream casts were taken at the same place as the tide turned, then a few casts were taken down stream following the ebb tide, with another cast taken near Kopu Bridge at about 4,000m. During the December and January field trips, casts were taken only going upstream with the flooding tide. During the March field trip, measurements were taken going up stream, starting from Kopu Bridge, until reaching almost 10,000 m upstream, before following the ebbing tide back downstream to about 6,700 m from the mouth of the river. During the April field trip, casts were taken going up stream from 6,000 to 10,000 m upstream, before following the ebb tide downstream taken casts from 10,000 m to about 4,000 m upstream of the mouth near Kopu Bridge.

3.3 Numerical modelling introduction

A hydrodynamic model using the Delft 3D FLOW software package was provided by Dr Stephen Hunt from the Waikato Regional Council. The modelling suite is capable of numerically modelling three-dimensional flows in water bodies such as estuaries, coastal areas, rivers and lakes. Additionally, modules can be used to simulate waves, sediment transport, water quality, and ecology. The model of the Waihou uses the FLOW module, which is based on the full Navier-Stokes equations with the shallow water approximation applied (Deltares systems, 2017b).

The model simulates flows and water levels in the Waihou River from Te Aroha into the Firth of Thames and the lower Firth. The model was developed in order to aid with monitoring of the Waihou River. The model was initially calibrated in two-dimensions for predictions of water depths and velocities. One of the aims of the present work was to test how well the model performed when layers in the vertical were introduced.

3.4 Model set up

The grid and depth files were created by Dr Stephen Hunt from the Waikato Regional Council and are shown in Figure 3.3. The model uses a cartesian grid with grid cell sizes ranging from approximately 270 m by 290 m in the Lower Firth of Thames, to 251 m by 118 m near the river mouth, to 10 m by 2 m in the upper river. The model was set to a latitude of -37.3°. There were 1,991 grid cells in the M-direction, and 38 grid cells in the N-direction, and covered a region of around 77 km in the longitude and 23 km in the latitude. The model was changed to contain 10 sigma-layers in the vertical, and the thickness of each layer was 10 % of the total water depth.

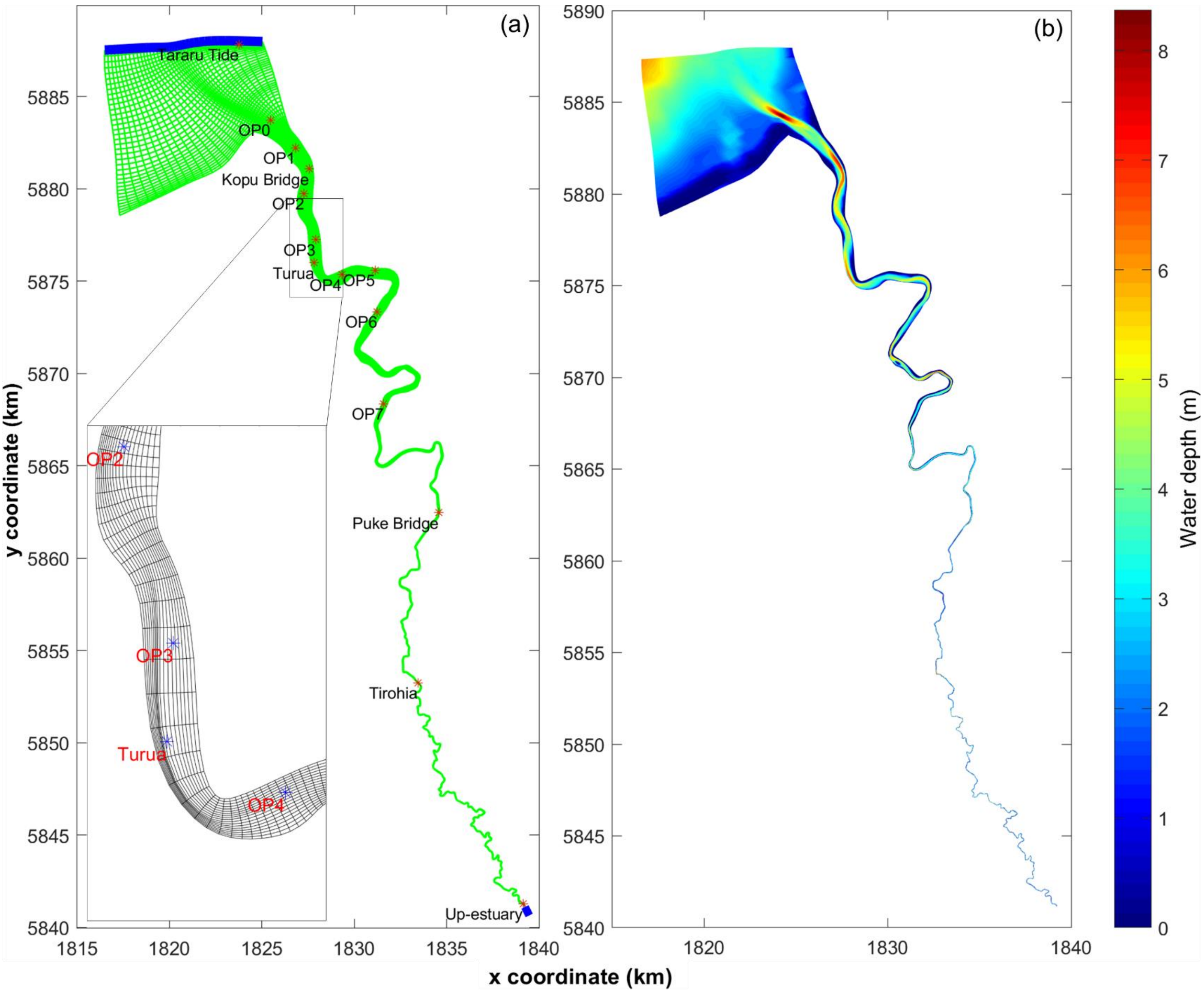

Figure 3.3: Set up of the Delft3D numerical model showing the (a) hydrodynamic grid (green), observation points (red, Table A.1), and open boundaries (blue), and (b) bathymetry (relative to mean tide level). The insert in panel (a) shows a close-up view of the grid near Turua.

Flows were forced at two open boundaries (Figure 3.3): by time series of water levels taken from Waikato Regional Council monitoring stations at Te Aroha and Firth of Thames (Tararu). The tidal boundary salinity was set to 32 PSU, while the river output was set to fresh water (salinity = 0). Temperatures were set throughout the model to a uniform value (in space and time) of 15°C. Models corresponded to each of the field surveys. Forcing was applied for 4 days before the date of measurement to allow a spin up period, to 12 hours after the time of the last measurement in the survey (Table 3.2). The time step for all of the model runs were 0.01 min. The initial conditions were water levels and salinity at 0 m and 0 PSU, respectively for all points in the model and a 60-minute smoothing period was applied. For the spin-up period, model output was stored at 60-minute intervals for the full domain, and at 10-min intervals for defined observation points (shown in Figure 3.3). For 24 hours of simulated time, model output was stored at 5-minute intervals for both the full domain and observation points.

Table 3.2: Model simulations including start and end times. Changed parameters are horizontal eddy viscosity (HEV), and horizontal eddy diffusivity (HED).

Model	**Note**	**NZST Start**	**NZST End**	**HEV ($m^2.s^{-1}$)**	**HED ($m^2.s^{-1}$)**
1	Original 2D	15/04/2015 0:00	29/04/2015 0:00	1	10
2	Original 3D	15/04/2015 0:00	22/04/2015 0:00	1	10
3	Survey 1	16/09/2022 0:00	20/09/2022 4:00	1	10
4	Survey 2	16/12/2022 0:00	20/12/2022 5:00	1	10
5	Survey 3	15/01/2023 0:00	19/01/2023 6:00	1	10
6	Survey 4	10/03/2023 0:00	14/03/2023 3:00	1	10
7	Survey 5	24/04/2023 0:00	28/04/2023 5:00	1	10
8	Survey 1 changed	19/09/2022 0:00	20/09/2022 0:00	0.1	10
9	Survey 1 changed	19/09/2022 0:00	20/09/2022 0:00	1	1
10	Survey 1 changed	19/09/2022 0:00	20/09/2022 0:00	0.1	1
11	Survey 1 changed	19/09/2022 0:00	20/09/2022 0:00	1	0.1
12	Survey 2 changed	19/12/2022 0:00	20/12/2022 0:00	1	0.1
13	Survey 4 changed	13/03/2023 0:00	14/03/2023 0:00	1	1

The model used a Mannin bottom roughness parameterisation with Manning coefficients of 0.03 and 0.02 $m^{-1/3}.s$ in the x and y directions, respectively. A free-slip condition was applied and gravitational acceleration was set to 9.81 $m.s^{-2}$. The background horizontal eddy viscosity was set to a uniform value of 1 $m^2.s^{-1}$, and the background horizontal eddy diffusivity set at 10 m^2s^{-1} for the initial model runs (noting that the horizontal eddy diffusivity was later changed to 0.1 m^2s^{-1}). The background vertical viscosity and diffusivities were set to 0 $m^2.s^{-1}$. A cyclic advection scheme for momentum and transport coupled with a horizontal forester filter were applied (Lesser et al., 2004). A k-ε turbulence closure scheme was applied.

Chapter 4: Results

4.1 Field observations: tidal and flow conditions during surveys

The tidal cycle is a mixed semi-diurnal tide due to the mid-latitude location of the site, with a strong monthly and spring-neap cycle. Figure 4.1 shows when the field surveys were undertaken relative to the tidal cycle. The September field visit (survey 1) was notably taken during a low neap tide, survey 4 (March) was taken during a small spring tide, while the other surveys were taken across the spring-neap cycle. Similarly, Figure 4.2 shows the survey time relation to the flow and level of the Waihou River from two different monitoring stations (locations are shown in Figure 2.1). The Te Aroha station is far from the river mouth and river flows (panel a) and the water level (panel b) at this location are not influenced by the tide. The Puke Bridge station only records the river level, and is influenced by tidal changes as it is further downstream than Te Aroha. Surveys 1, 4 and 5 (September, March, and April) were taken during relatively low flows, while the measurements taken during survey 2 (December) were taken just after a relatively high flow and survey 3 (January) was taken just after a relatively high flow event as the river had settled back to a closer-to-average flow.

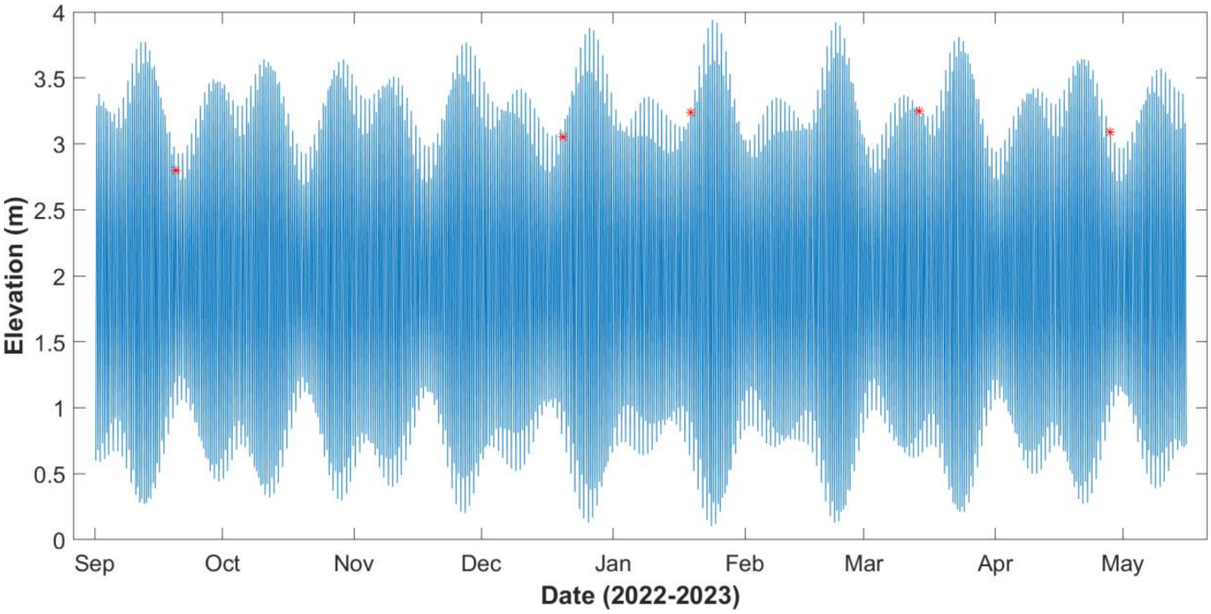

Figure 4.1: Tidal elevation from September 2022 to May 2023. Red markers indicate the days that measurements were taken at Waihou River. Tide predictions taken from Latitude -37.216, Longitude 175.565 between Kopu Bridge and Turua, by NIWA www.tides.niwa.co.nz.

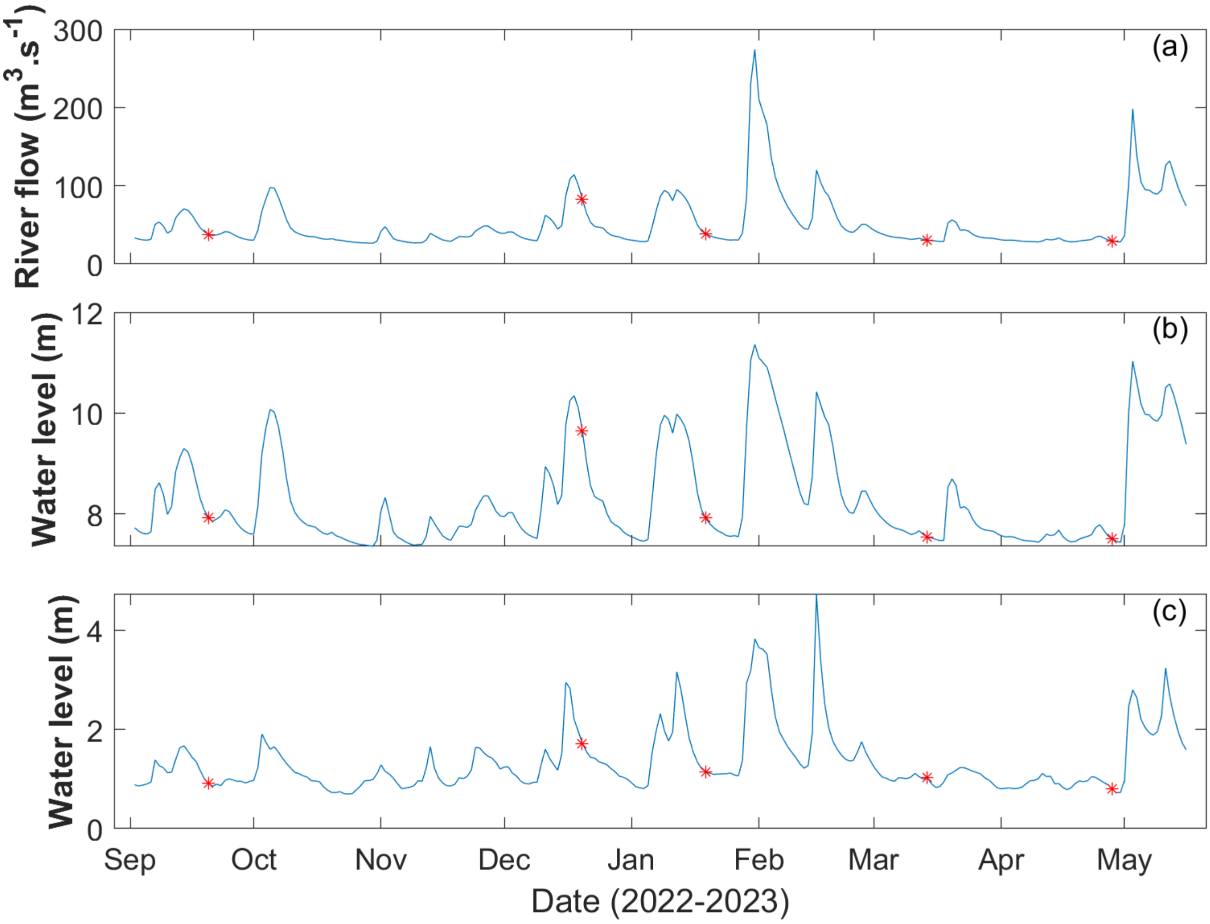

Figure 4.2: River flow and levels for the Waihou River from September 2022 to May 2023 (a, b) Te Aroha station, (c) Puke Bridge station. Red markers indicate days that CTD measurements were taken in the field. Flow and level measurements from the Waikato Regional Council www.waikatoregion.govt.nz.

Shorter-term flow conditions for the different surveys are shown in Figures 4.3 to 4.7. For survey 1 the river flow recorded in Te Aroha during the time of measurements was between 37.9 m^3.s^{-1} and 37.5 m^3.s^{-1} (Figure 4.3). The average flow for the day was 38.4 m^3.s^{-1}. The water level recorded at Te Aroha was between 7.92 m and 7.90 m and at Puke bridge the river level was between 0.48 m and 1.58 m for the duration of the survey. Survey 2 (Figure 4.4) was taken during stronger flows (between 83.5 m^3.s^{-1} and 79.4 m^3.s^{-1} recorded in Te Aroha with a mean flow of 83.8 m^3.s^{-1}) and higher water levels (between 9.70 m and 9.57 m and from 1.5 m and 1.9 m, for Te Aroha and Puke bridge, respectively). Conditions during survey 3 (Figure 4.5) were similar to those during the first survey: the river flows recorded in Te Aroha were between 38.8 m^3.s^{-1} and 38.1 m^3.s^{-1} (mean flow of 41.2 m^3.s^{-1}). The water levels were between 7.93 m and 7.89 m and between 0.63 m and 1.69 m for Te Aroha and

Puke Bridge, respectively, for the duration of the survey. For surveys 4 and 5 (Figures 4.6 and 4.7) mean flows at Te Aroha were 33.2 m^3.s^{-1} and 32.3 m^3.s^{-1}, respectively, with peak water levels around 7.55 m at Te Aroha and 1.94 m (survey 4) and 1.48 m (survey 5) at Puke Bridge.

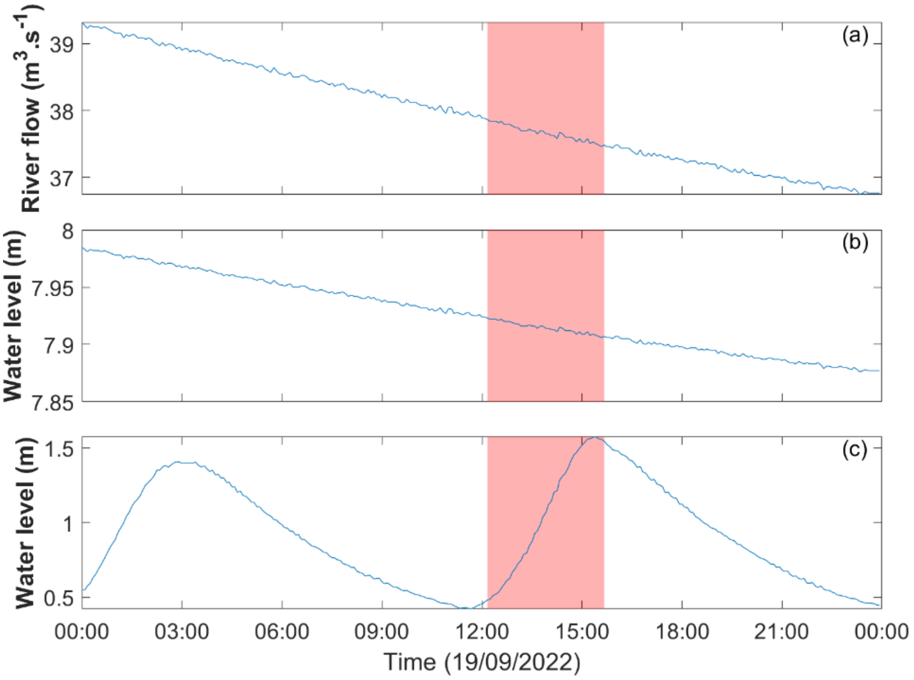

Figure 4.3 River flow and levels for the Waihou River for the day of the 19th of September 2022, (a, b) Te Aroha Station, (c) Puke Bridge Station. Red boxes indicate the time that CTD measurements were taken in the field. Flow and level measurements from the Waikato Regional Council www.waikatoregion.govt.nz.

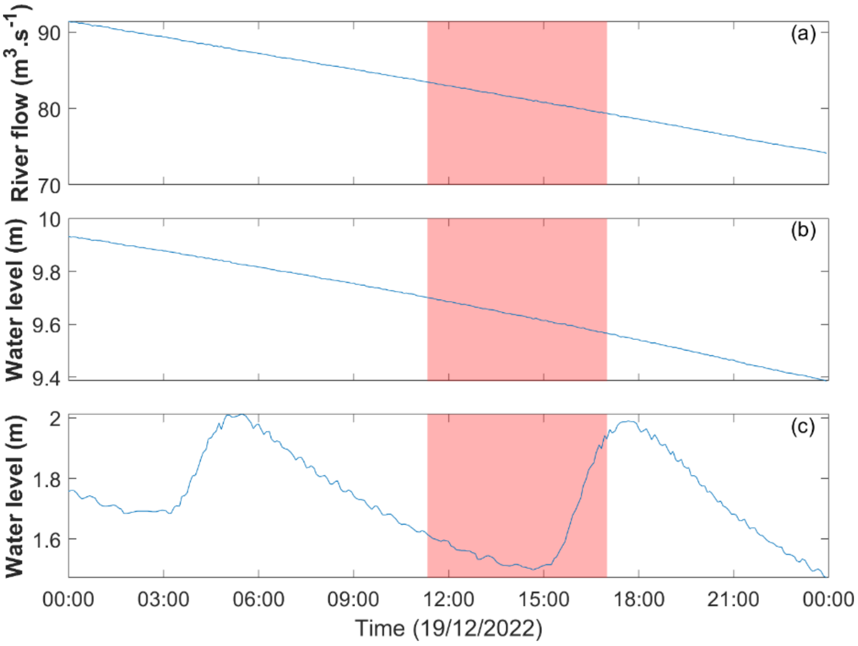

Figure 4.4: River flow and levels for the Waihou River for the day of the 19th of December 2022, (a, b) Te Aroha Station, (c) Puke Bridge Station. Red boxes indicate the time that CTD measurements were taken in the field. Flow and level measurements from the Waikato Regional Council www.waikatoregion.govt.nz.

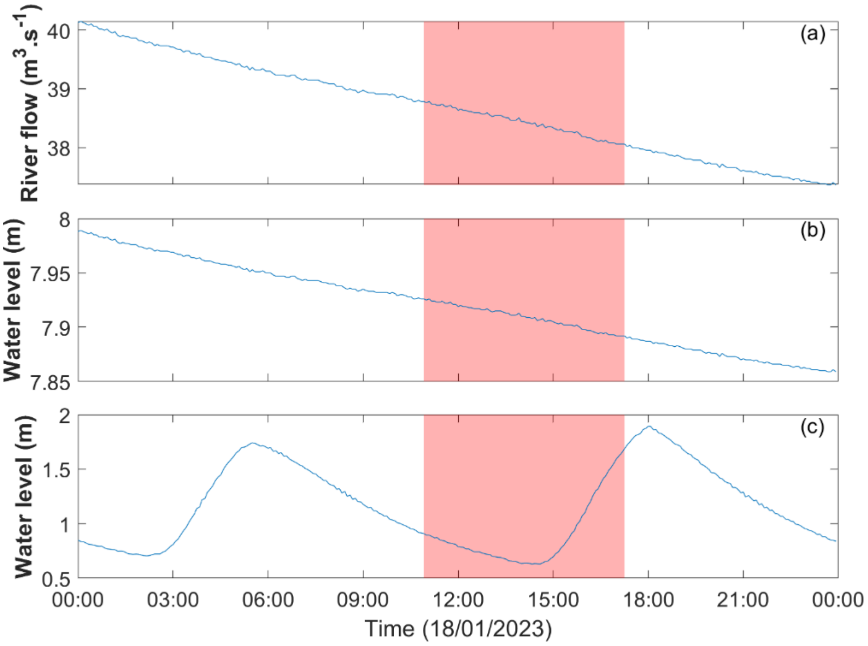

Figure 4.5: River flow and levels for the Waihou River for the day of the 18th of January 2023, (a, b) Te Aroha Station, (c) Puke Bridge Station. Red boxes indicate the time that CTD measurements were taken in the field. Flow and level measurements from the Waikato Regional Council www.waikatoregion.govt.nz.

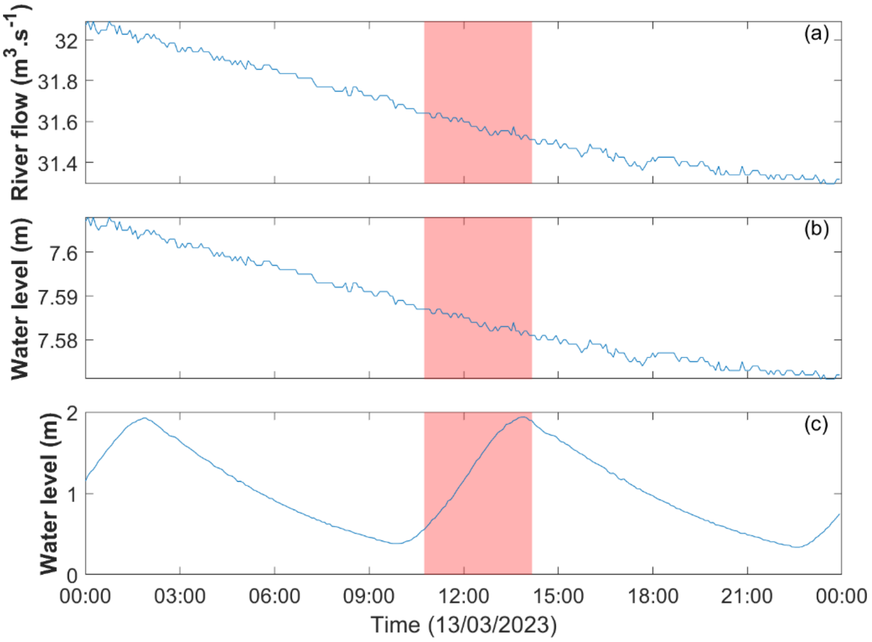

Figure 4.6: River flow and levels for the Waihou River for the day of the 13th of March 2023, (a, b) Te Aroha Station, (c) Puke Bridge Station. Red boxes indicate the time that CTD measurements were taken in the field. Flow and level measurements from the Waikato Regional Council www.waikatoregion.govt.nz.

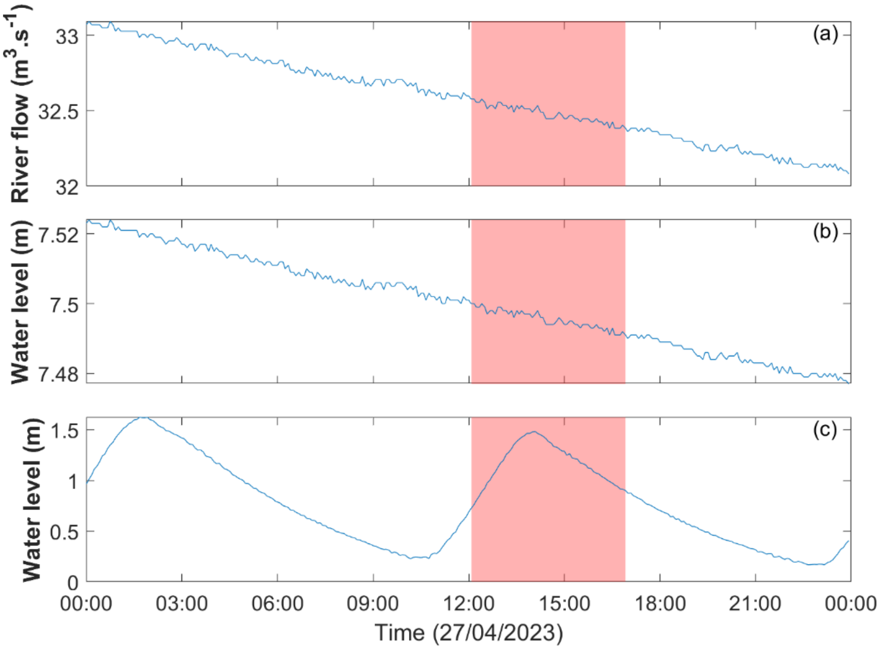

Figure 4.7: River flow and levels for the Waihou River for the day of the 27th of April 2023, (a, b) Te Aroha Station, (c) Puke Bridge Station. Red boxes indicate the time that CTD measurements were taken in the field. Flow and level measurements from the Waikato Regional Council www.waikatoregion.govt.nz.

4.2 Field observations: density structure and salt-intrusion

In this section, we report the key results from each survey, with particular emphasis on identifying maximum extent of the salt intrusion and if a salt wedge is present.

4.2.1 Survey 1 (September 2022)

As the flood tide propagated upstream, the water column was stably stratified and predominantly well-mixed (Figure 4.8), with maximum salinity, temperature and density differences between surface and near-bed of 3.32 PSU, 0.5°C, and 2.6 kg.m^{-3}, respectively. The maximum salinity observed from each cast is shown in Figure 4.9. From this figure we can estimate the approximate distances upstream reached by varying salinity levels: 20 PSU reached 4.76 km upstream from the river mouth. 10 PSU of salinity reached 7.45 km upstream, 5 PSU reached 8.51. The furthest measurement upstream was taken at 9.34 km upstream, and showed a salinity value of 3.2 PSU close to the bed.

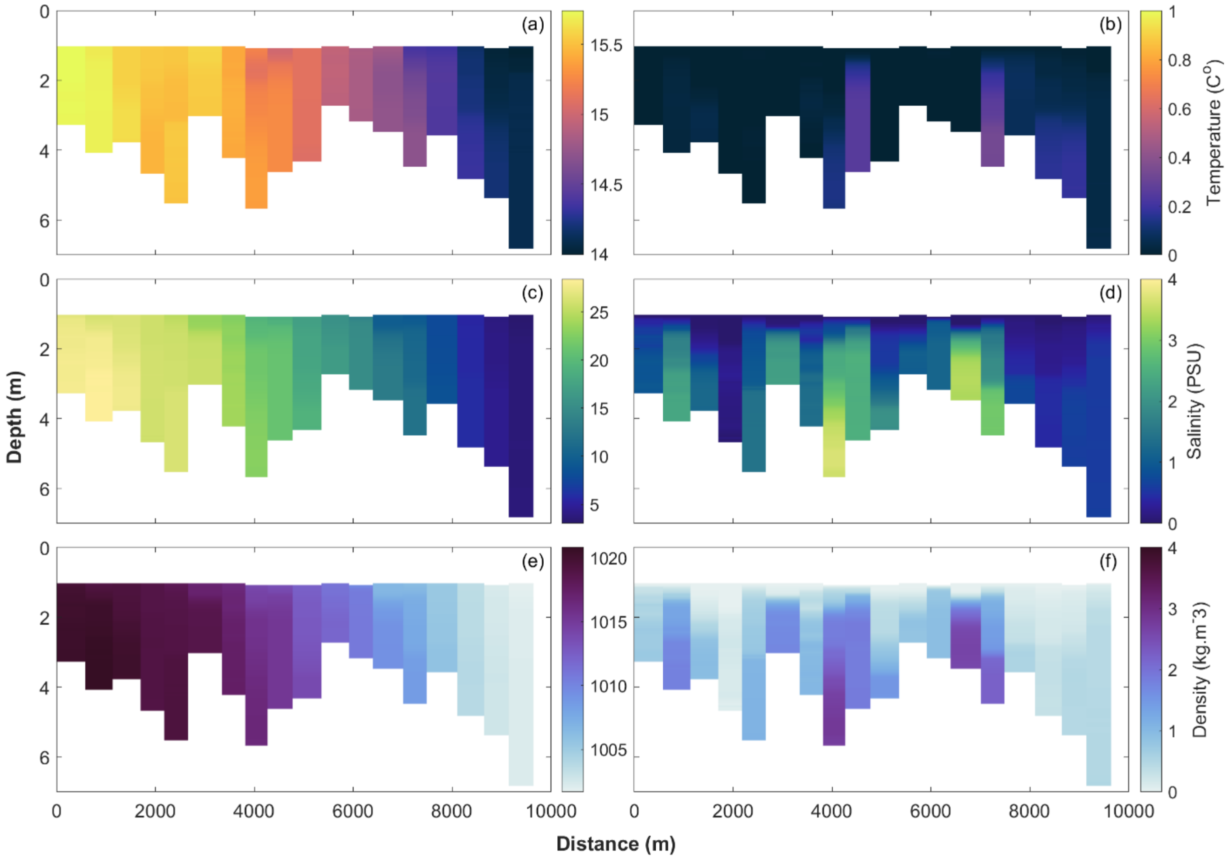

Figure 4.8: Left-hand column: Profiles of (a) temperature, (c) salinity, (e) density, as a function of distance along the river from survey 1 (September 2022). Right-hand column: Differences from the near-surface value (taken from the highest measurement in water column) of (b) temperature, (d) salinity, and (f) density.

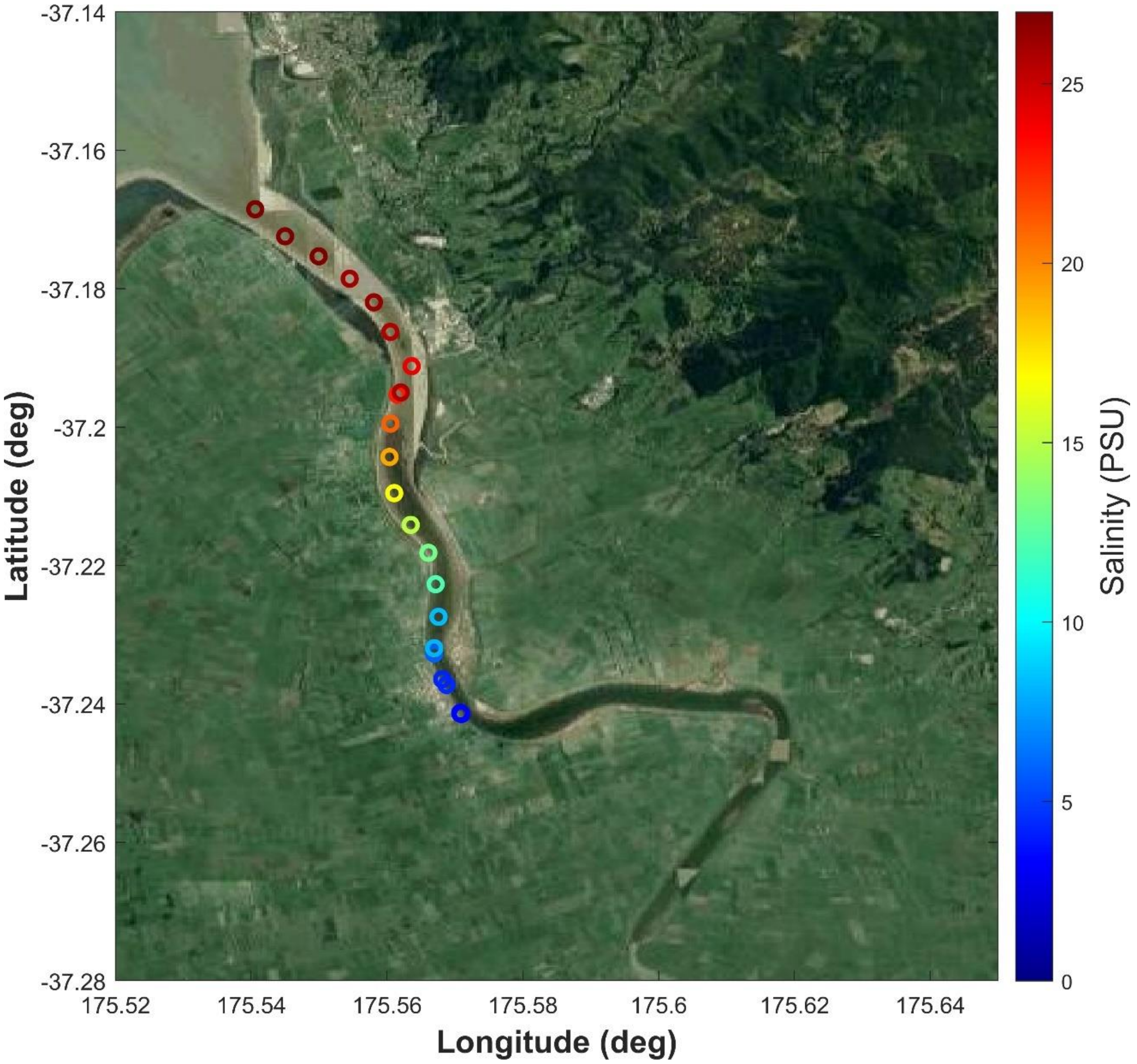

Figure 4.9: Observed salinity maximum (psu) measured at each CTD cast location for Survey 1 (September 2022). The background image is a Google Earth satellite image.

Observed salinities were at least 25 PSU close to the river mouth (distances of 0 to 3,500 m), density was at least 1,020 kg.m^{-3}, and temperature at 15.5°C, and around 10 to 25 PSU, 1,002-1,005 kg.m^{-3}, 14.8-15.5°C around 3,500 m to 7,500m upriver from the mouth. For distances beyond 7,500 m, all observed salinity values were less than 10 PSU, density values were less than 1,002 kg.m^{-3} and temperature values less than 14.5°C. The patterns in density closely reflect those observed in the salinity profiles, thus indicating that (as expected) the salinity was the primary control on the density structure, with temperature playing a much smaller dynamical role.

At the maximum distance upstream close to high tide, four casts were taken in the same location over a period of time of an hour, as the tide was turning and showed a gradual decrease in salinity (Figure 4.10a). The profiles change slowly over time as the direction of the tide reverses. As time progresses, there is a thinning and freshening of the salt intrusion at the bottom of the water column. depicting the tide moving back down the river.

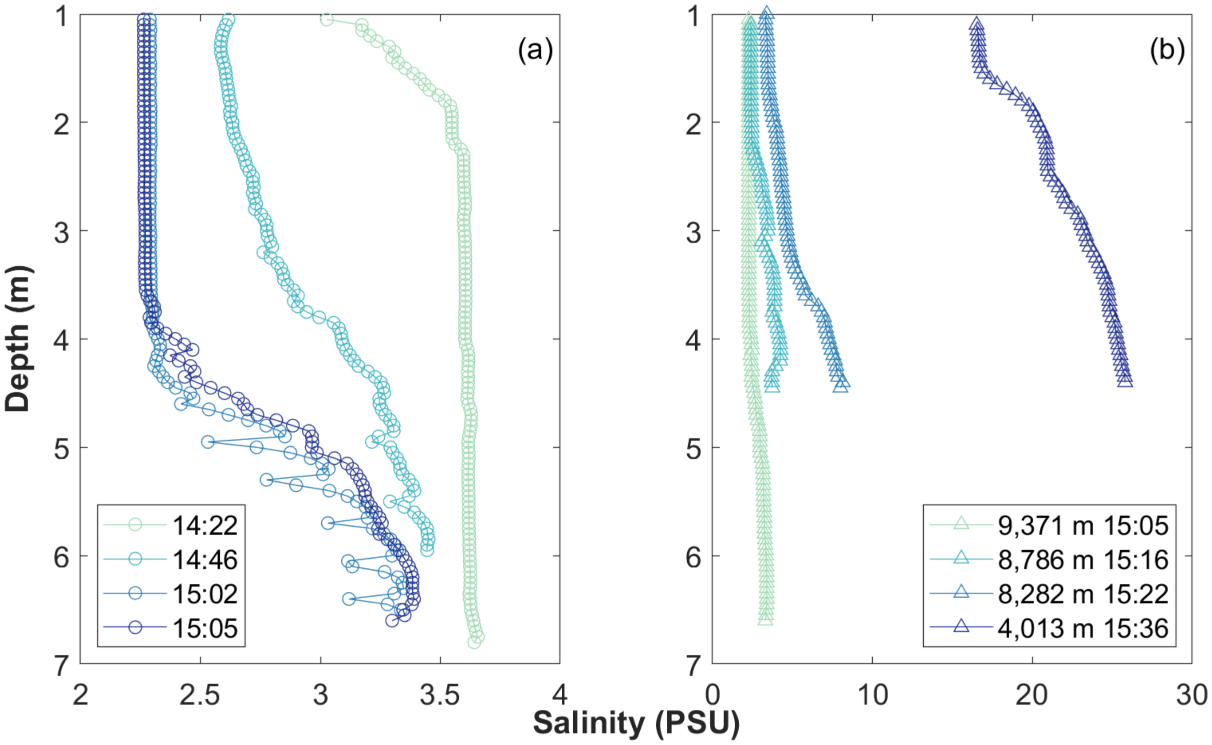

Figure 4.10: Salinity profiles for casts taken in the same location ~9,380m upstream from the river mouth (a) and casts taken while travelling downstream (b), measurements taken on September 19th 2022.

The plot shown in Figure 4.10b shows casts taken while travelling downstream during the start of the ebb tide, starting from 9,371 m upstream down to 4,013 m upstream from the river mouth. The cast at 9,371 m shows a slight halocline as the difference in salinity is small, the cast at 8,282 m shows a slightly more exaggerated halocline relative to the cast at 4,013 m, and the cast at 4,013 m shows an even more exaggerated halocline, although, overall salinities are larger (~20 PSU near the surface). The density profiles follow a very similar pattern to that of the salinity profiles, with observed densities ranging from 1,001 to 1,002 kg.m^{-3} at the furthest point upstream, and 1,000-1,020 kg.m^{-3} for casts taken while travelling downstream.

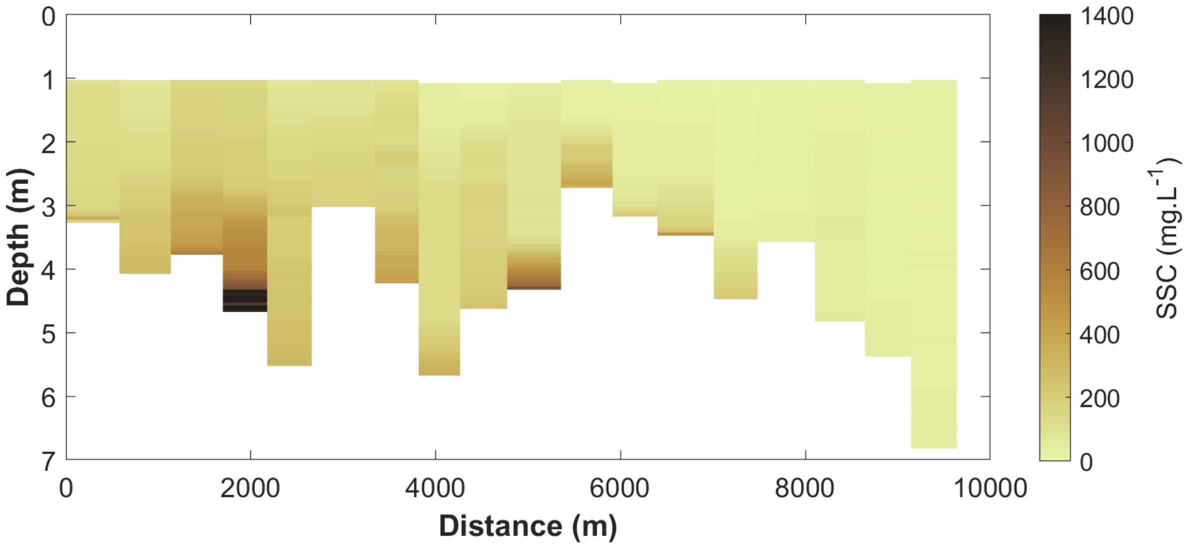

Figure 4.11: Suspended sediment concentration profiles of casts taken on September 19th, 2022.

In general, suspended sediment concentrations throughout the water column were around 200-400 mg.L^{-1}, and decreased with distance upriver (and time/tidal stage). Most profiles exhibited some depth variability with greater sediment concentrations near the seafloor. Maximum observed concentrations over the survey were around 1,400 mg.L^{-1}, which were near-bed values closer to the river mouth.

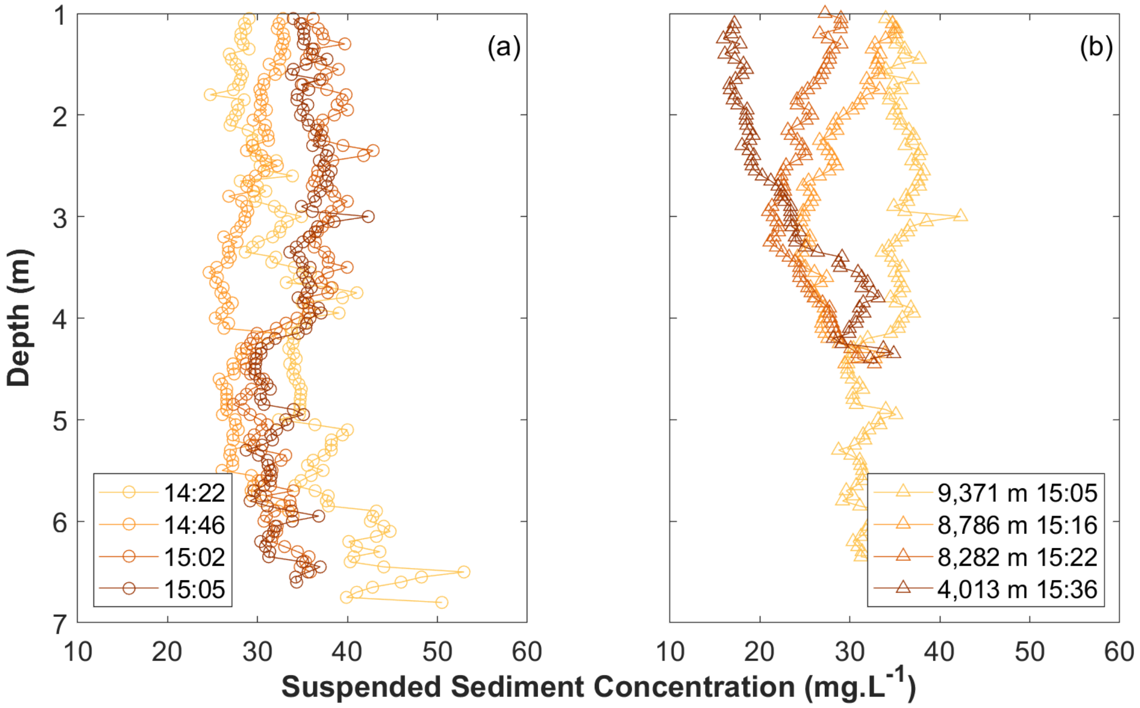

Figure 4.12: Suspended sediment concentration calculated from voltage 1 for casts taken in the same location ~9,380 m upstream from the river mouth (a), and casts taken while travelling downstream (b).

The profiles shown in for Figure 4.12a show casts taken in the same location at the furthest point upstream as the tide was turning from flood to ebb tide. There is very little difference between the profiles, with concentrations in the majority of the water column of around 30-40 mg L^{-1}. The plot in Figure 4.12b shows profiles that were taken while travelling downstream, as the tide was flowing back out of the estuary. While overall sediment concentrations are relatively small, there is an observable decrease in concentrations with distance downstream (noting that observations also change in time).

The ExoSonde measurements taken during survey 1 are shown in Figure 4.13, which includes measurements of pH, chlorophyll, fluorescent dissolved organic matter (fDOM), and dissolved oxygen (DO). Observed pH and chlorophyll was greater within the salinity intrusion, than in fresh water. Conversely, fDOM was smaller within the salinity intrusion than the fresh water. Observed DO was very high during the survey. Differences between the surface and near bed were approximately 0.2, 15 µg.L^{-1}, 0.5 RFU, and 3 % for pH, chlorophyll, fDOM, and DO respectively (Figure 4.13).

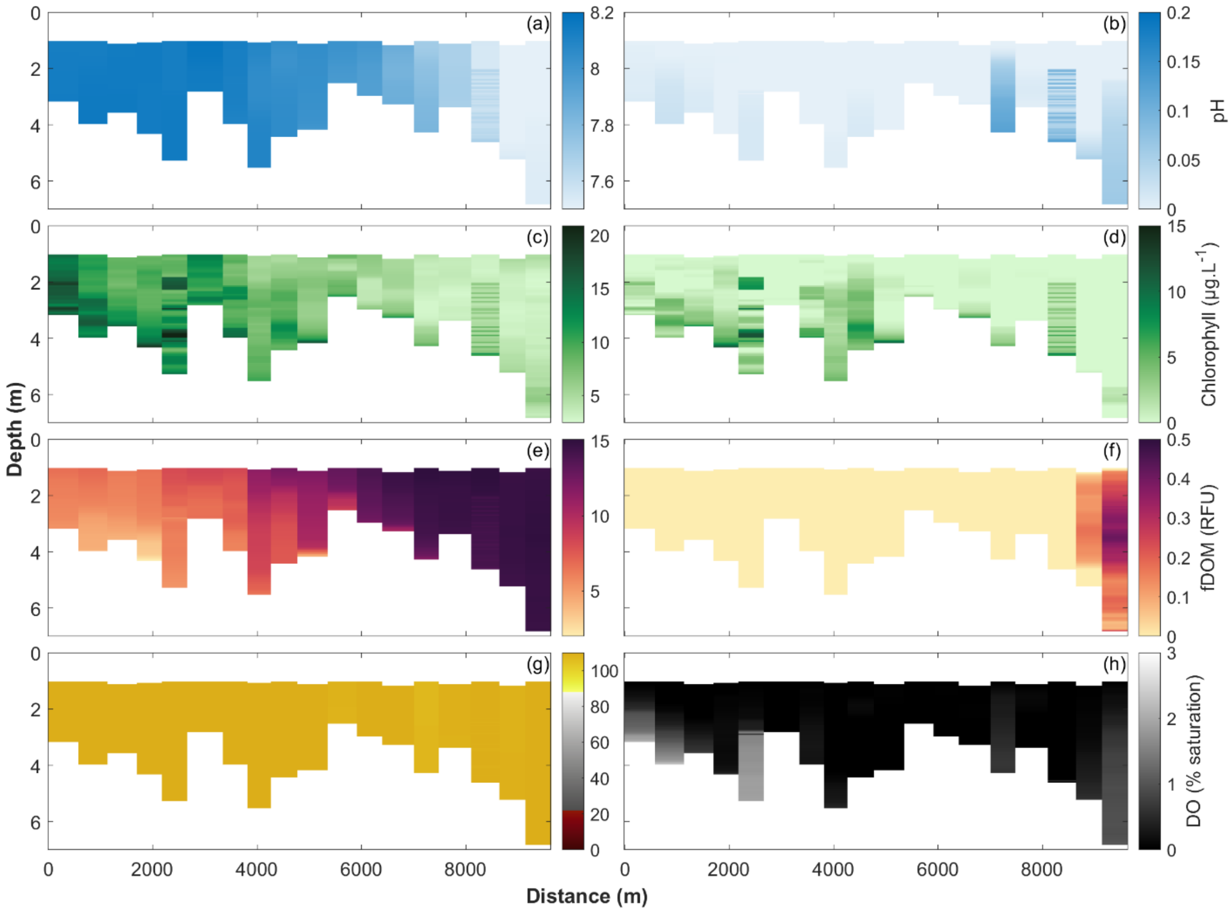

Figure 4.13: Left-hand column: Profiles of (a) pH, (c) chlorophyll, (e) fluorescent dissolved organic matter (fDOM) (g) dissolved oxygen, as a function of distance along the river from survey 1 (September 2022). Right-hand column: Differences from the near-surface value (taken from the highest measurement in water column) of (b) pH, (d) chlorophyll, (f) fDOM, and (h) dissolved oxygen.

4.2.2 Survey 2 (December 2022)

In December, the survey followed the salt intrusion moving upstream on the incoming tide. On this occasion, in the majority of locations, several (two to four) casts were taken at the same point. Profiles of temperature, salinity and density are shown in Figure 4.14, with maximum differences between surface and the near-bed of 13.7 PSU, 1.6 °C, and 10.6 kg.m^{-3} respectively. In this case, a much stronger halocline was present with almost freshwater at the surface of the water column to salt water at the bottom, thus implying a more clearly defined salt wedge. Repeat casts from the same location are shown in Figure 4.16. The Salinity intrusion can be seen in the profiles in each plot. The first couple of casts have relatively low levels of salinity, while the last cast shows greater salinities (an increase of 8 PSU over 20 minutes and more exaggerated haloclines.

However, the intrusion did not reach as far upstream as in the first survey. Figure 4.15 shows maximum salinity for each cast measured during the December field visit and shows how far the salinity travelled into the estuary during high tide. 10 PSU reached 4.53 km upstream from the mouth of the river. 5 PSU reached 6.19 km upstream, 1 PSU reached 7.25 km and 0.1 PSU reached 7.76 km upstream, which is the furthest measurement upstream (Figure 4.15).

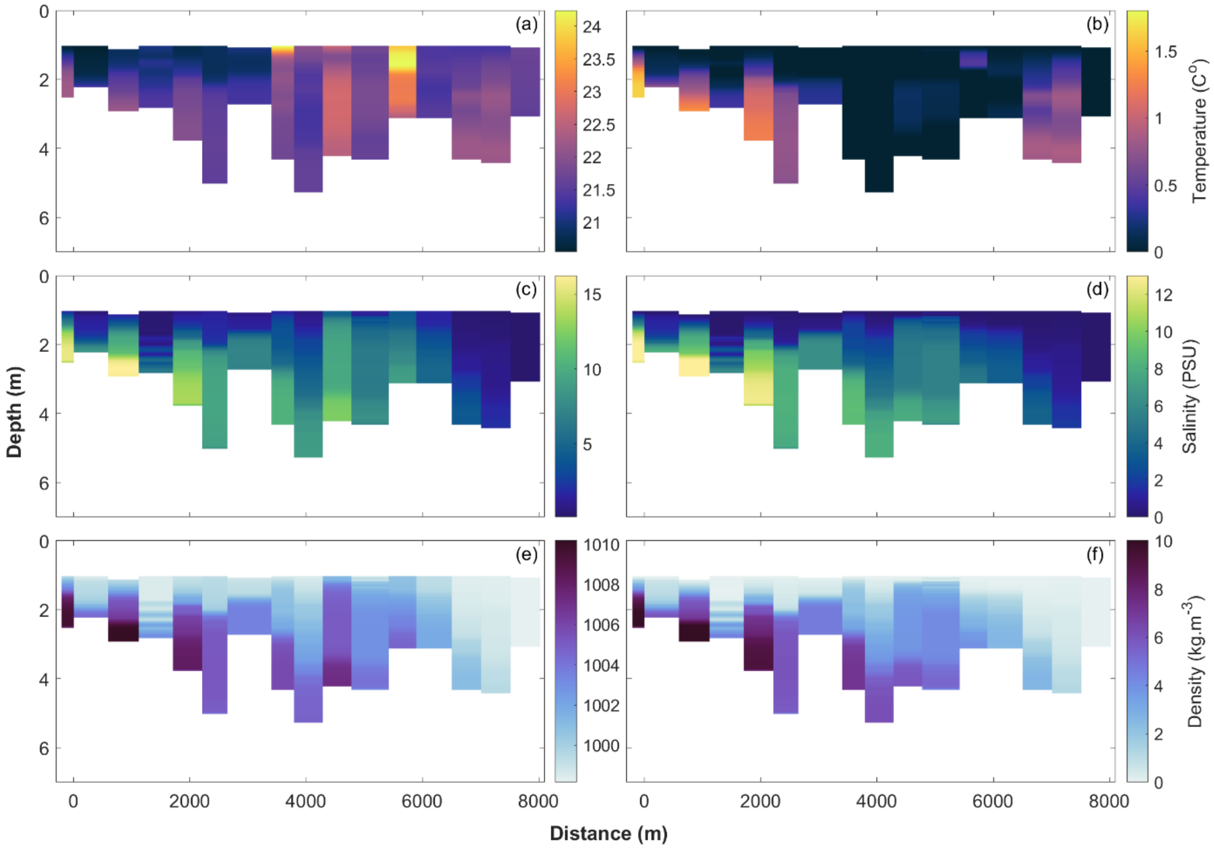

Figure 4.14: Left-hand column: Profiles of (a) temperature, (c) salinity, (e) density, as a function of distance along the river from survey 2 (December 2022). Right-hand column: Differences from the near-surface value (taken from the highest measurement in water column) of (b) temperature, (d) salinity, and (f) density.

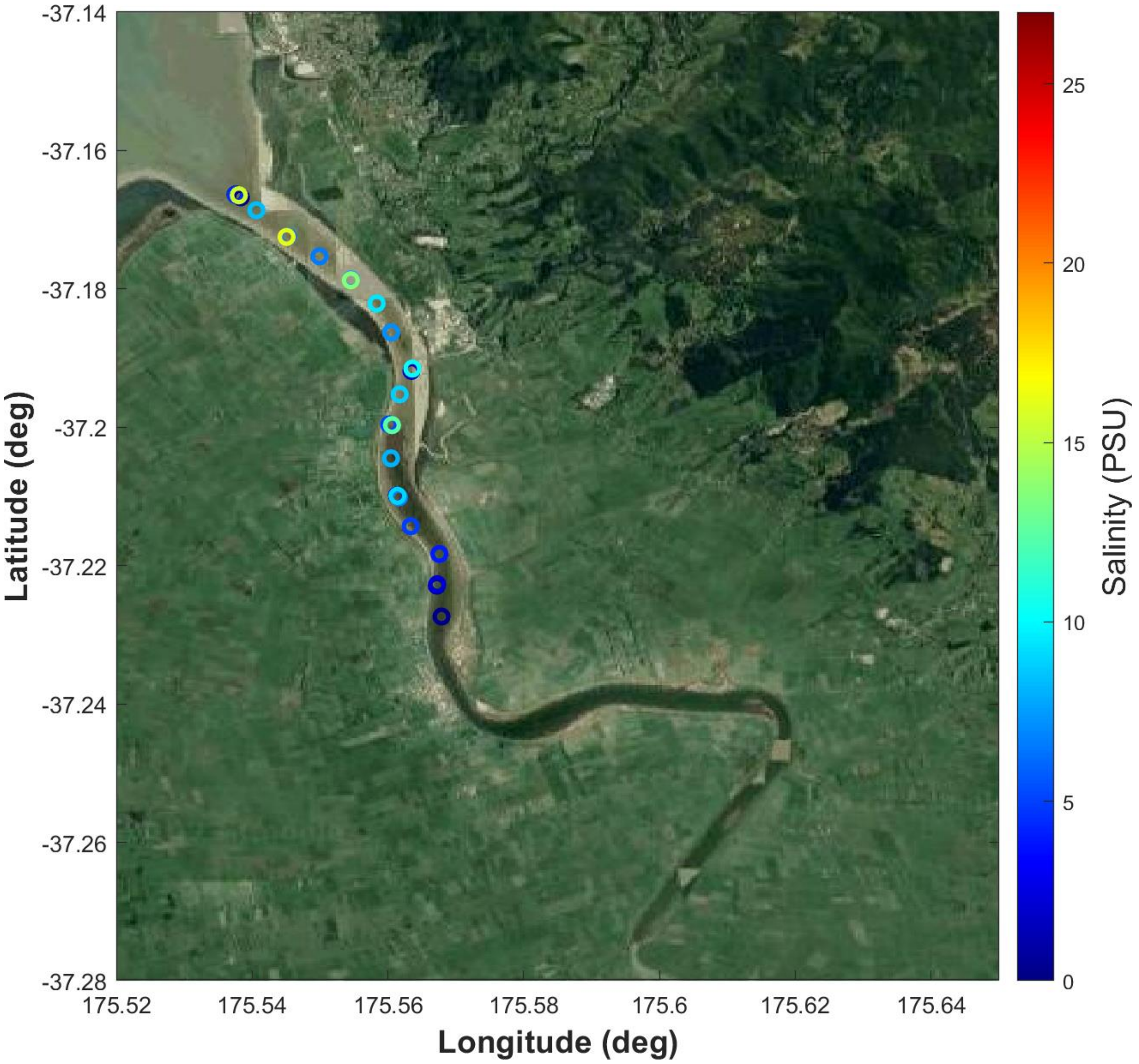

Figure 4.15: Points of maximum salinity measured at each site at the Waihou River, on a satellite image from Google Earth, for the December run.

Close to the river mouth (distances of 0 to 1,000 m) observed salinities were at least 15 PSU, and observed densities were 1,010 kg.m^{-3}, while for distances of 1,000 to 6,500 m upriver from the mouth, salinities and densities covered ranges of 5-15 PSU and 1,000-1,010 kg.m^{-3}, respectively. For distances beyond 7,000 m, salinity values were below 5 PSU and density values were below 1,000 kg.m^{-3}. The first 8 casts show significant stratification (0 to 4,000 m), from 4,500 m to 6,000m, the profiles are presented as mixed, both salinity and density values present this. The observed temperature values vary, from distances of 0 to 4,000 m upriver from the mouth, temperature varies from 21-22^{o}C with lower temperature at the surface, from 4,000 to 6,000 m, temperature varies from 22-24^{o}C with higher temperatures at the surface, beyond 6,000 m temperature varies from 21.5-22.5^{o}C, there is no clear pattern regarding temperature.

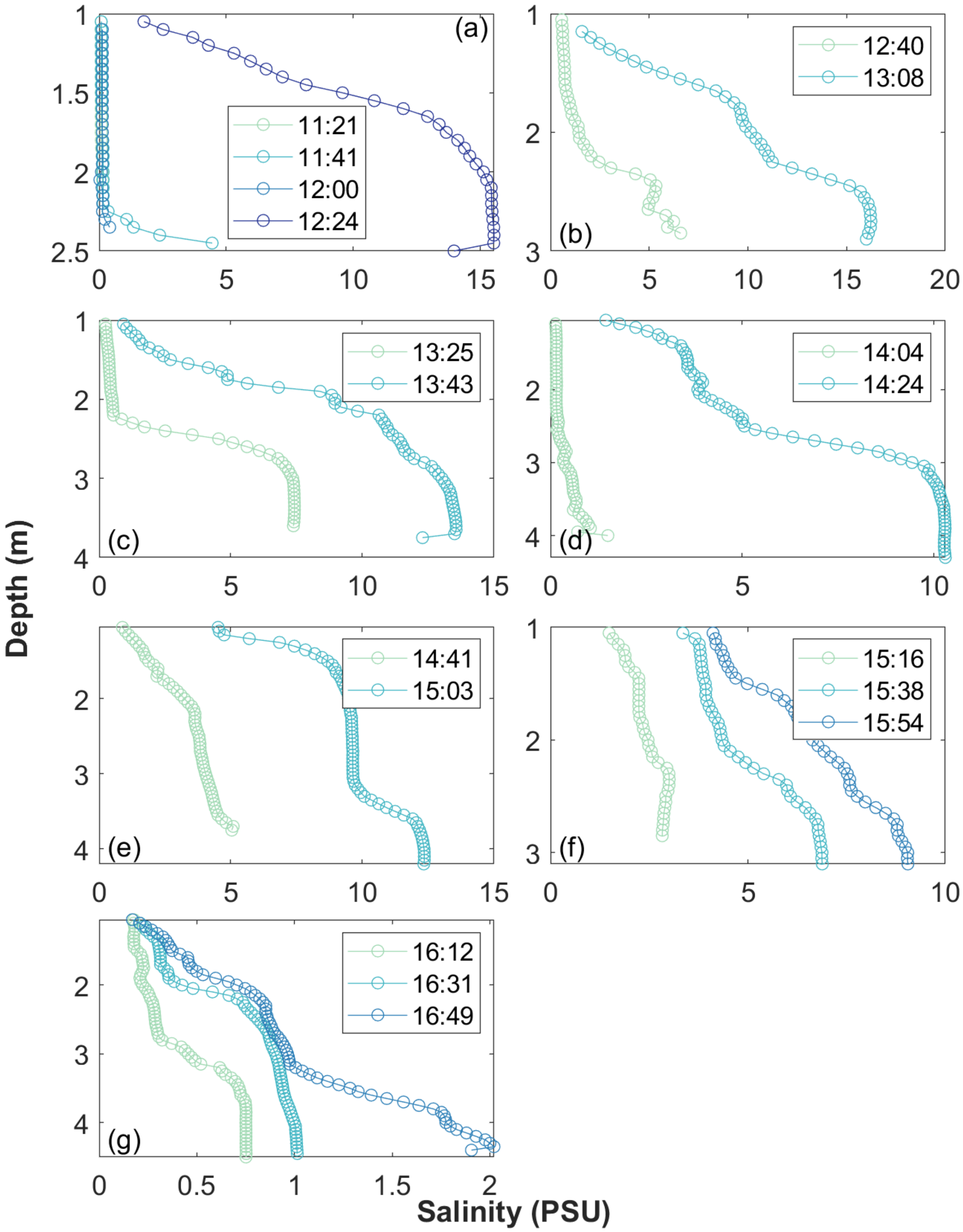

Figure 4.16: Salinity profiles for casts taken in the same location (a) ~-50 m, (b) 870 m, (c) 1,960 m, (d) 3,630 m, (e) 4,545 m, (f) 5,680 m, (g) 7,270 m.

The plots in Figure 4.16 depict profiles of casts that were taken in the same location as the tide was coming into the river. In majority of the locations, the first couple of casts have low levels of salinity, while the last cast has increased levels of salinity relative to the first couple of casts. The profiles show the salinity gradually increasing at each site, and the profiles gradually present more exaggerated haloclines. The density profiles for the same casts as those shown in Figure 4.16 follow the same patterns as the salinity profiles. Observed densities for plots a, b, and c range from 1,000-1,010 kg.m^{-3}, 999-1,005 kg.m^{-3} for plots d and f, 1,000-1,007 kg.m^{-3} for plot e and 998-999.5 kg.m^{-3} for plot g.

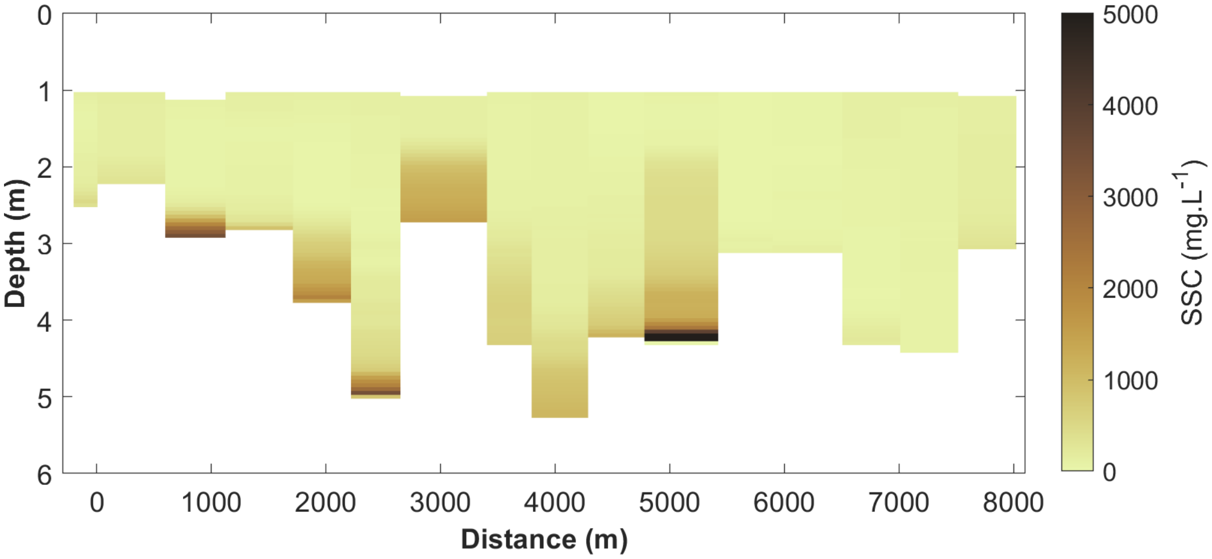

Figure 4.17: Suspended sediment concentration for casts taken on December 19th 2022.

Figure 4.17 shows the suspended sediment concentrations observed in the profiles of the casts. In general, suspended sediment concentrations throughout the water column were around 0-1,000 mg.L^{-1}, and decreased with distance up river. Most profiles exhibited depth-variability, with greater sediment concentrations near the bed. Notably, maximum observed concentrations observed were around 9,000 mg L^{-1} in the near-bed values, which is close to the nominal value for the presence of fluid mud.

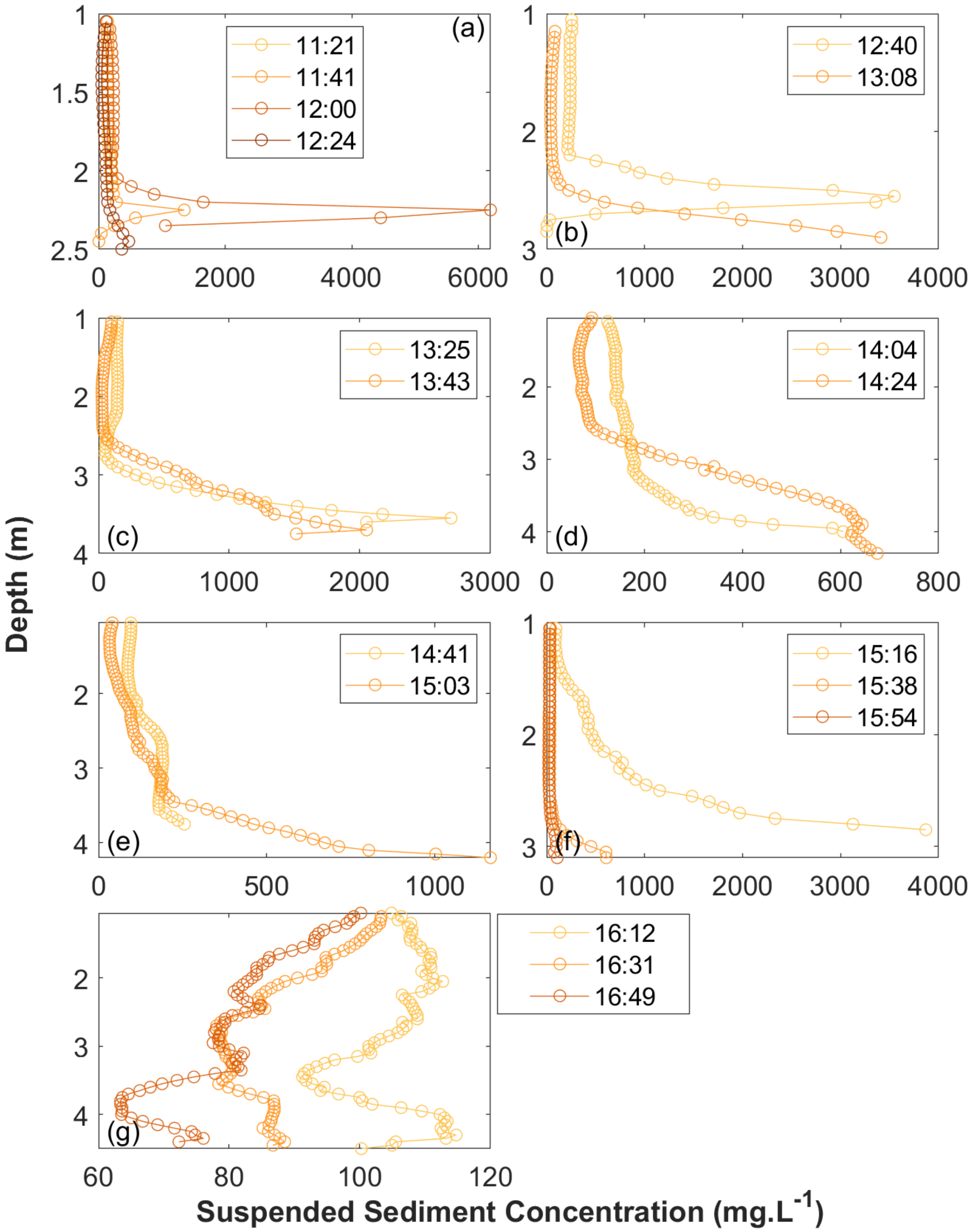

Figure 4.18: Suspended sediment concentration for casts taken in the same location (a) ~-50 m, (b) 870 m, (c) 1,960 m, (d) 3,630 m, (e) 4,545 m, (f) 5,680 m, (g) 7,270 m.

The plots in Figure 4.18 depict cast profiles that were taken in the same location as the tide was coming into the river. As the coastal water intruded further upstream, suspended sediment concentrations also increased. It can be seen in majority of the plots in Figure 4.18, that the bottom of the water column had greater SSC than the rest of the water column.

The ExoSonde measurements taken during survey 2 are shown in Figure 4.19, which includes measurements of pH, chlorophyll, fluorescent dissolved organic matter (fDOM), and dissolved oxygen (DO). Observed pH ranged from 6 to 7. Observed chlorophyll was greater within the salt wedge near the bed, than in fresh water. Conversely, fDOM was smaller within the salt wedge near the bed than the fresh water. Observed DO ranged from approximately 50-80%. Differences between the surface and near bed were approximately 1.2, 10 μg.L^{-1}, 3 RFU, and 5 % for pH, chlorophyll, fDOM, and DO respectively (Figure 4.19).

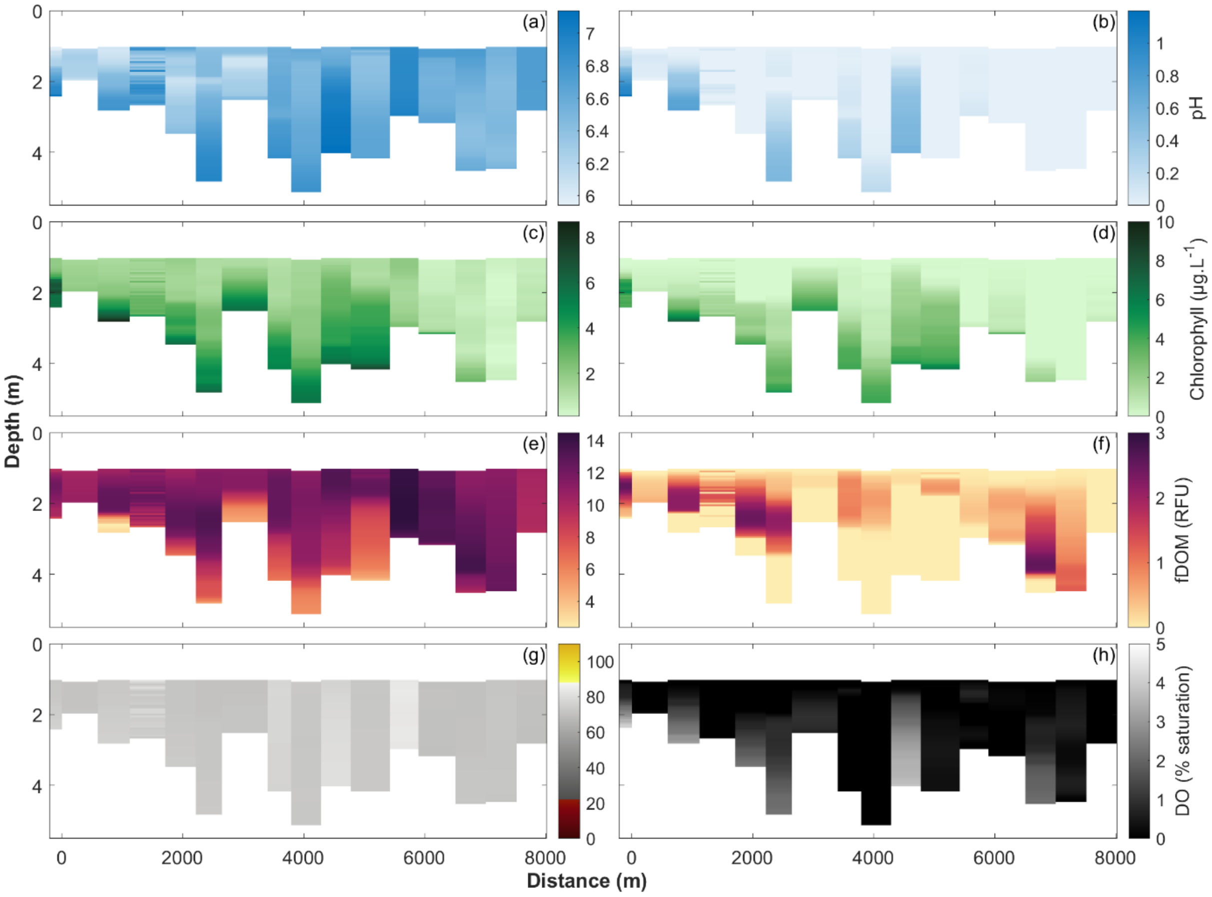

Figure 4.19: Left-hand column: Profiles of (a) pH, (c) chlorophyll, (e) fluorescent dissolved organic matter (fDOM) (g) dissolved oxygen, as a function of distance along the river from survey 2 (December 2022). Right-hand column: Differences from the near-surface value (taken from the highest measurement in water column) of (b) pH, (d) chlorophyll, (f) fDOM, and (h) dissolved oxygen.

4.2.3 Survey 3 (January 2023)

In January, the survey again followed the salt intrusion moving upstream on the incoming tide. Several casts were taken at the same point in a number of locations. Profiles of temperature, salinity and density are shown in Figure 4.20, with maximum differences between surface and the near-bed of 18.15 PSU, 0.23°C, and 13.52 kg.m^{-3} respectively. In this case, a strong halocline was present in the lower estuary, while the middle to upper estuary had less defined stratification. Repeat casts are shown in Figure 4.22. The salinity intrusions can be seen in the profiles in each plot, as the later casts have higher levels of salinity than the earlier casts. These field results showed the salinity intrusion penetrating further than the rest of the field results. Figure 4.21 shows maximum salinity for each cast measured during the January field visit and shows how far the salinity travelled into the estuary during high tide. 10 PSU reaches 7.38 km upstream from the mouth of the river, 5 PSU reaches 8.88 km upstream, 1 PSU reaches 11.87 km upstream, and 0.1 PSU reaches 12.53 km upstream with that being the furthest measurement upstream.

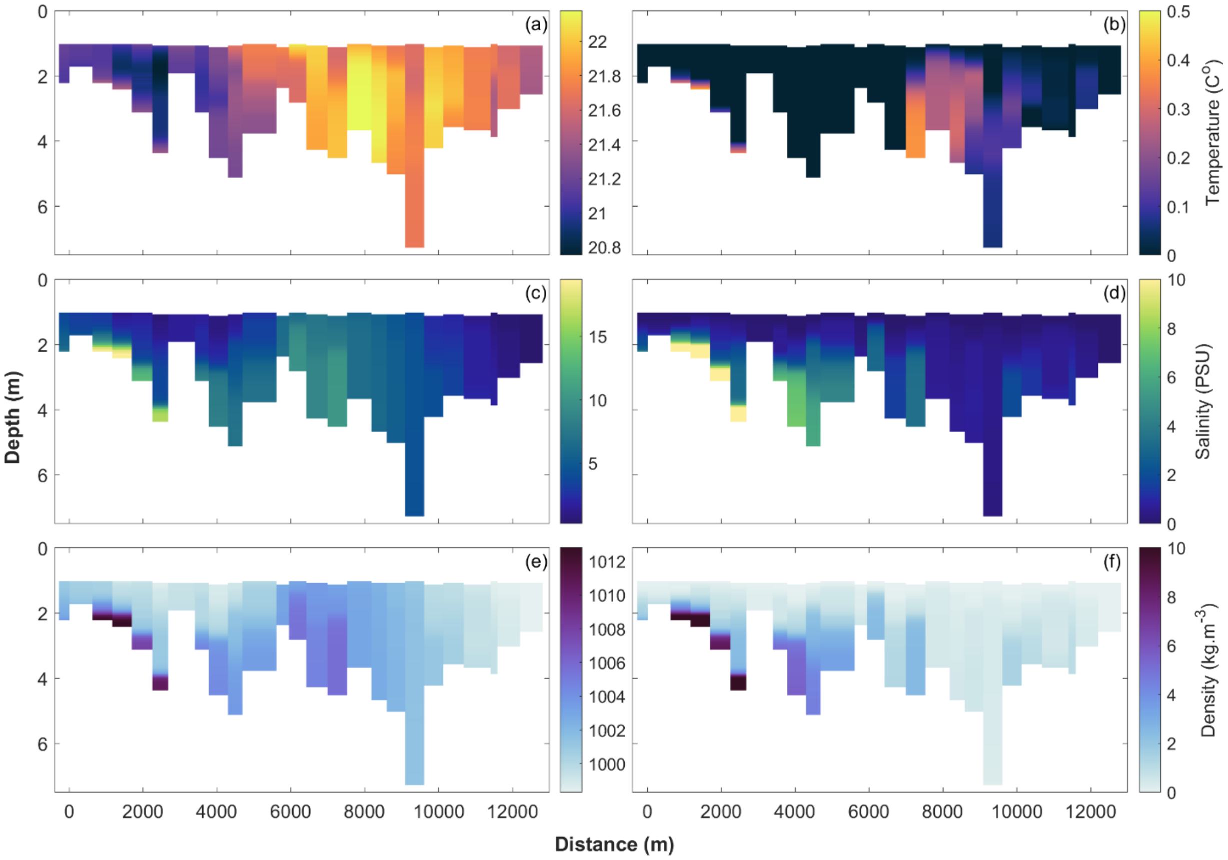

Figure 4.20: Left-hand column: Profiles of (a) temperature, (c) salinity, (e) density, as a function of distance along the river from survey 3 (January 2023). Right-hand column: Differences from the near-surface value (taken from the highest measurement in water column) of (b) temperature, (d) salinity, and (f) density.

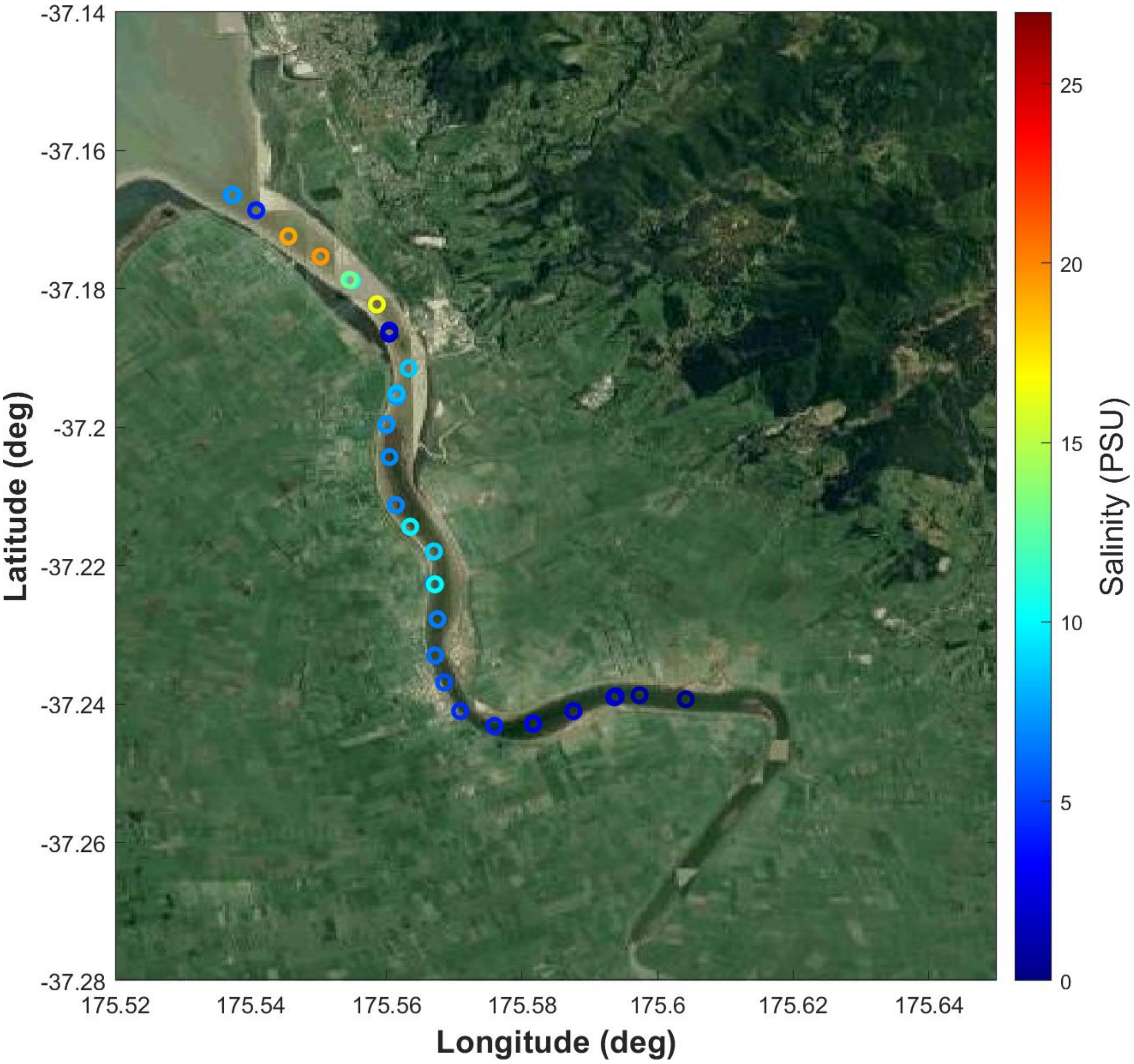

Figure 4.21: Points of maximum salinity measured at each site at the Waihou River, on a satellite image from Google Earth, for the January run.

Observed salinities were lower during the January visit compared to other field visits. Near the river mouth to distances up to 2,000 m upriver from the mouth, salinities of at least 15 PSU and densities of at least 1,012 kg.m^{-3} were observed, 5-10 PSU and 1,004 kg.m^{-3} from 2,000 to 10,000 m upriver from the mouth, for distances beyond 11,000 m salinities were below 5 PSU and observed density was lower than 1,000 kg.m^{-3}. Observed temperatures from 0 to 4,000 m from the river mouth are around 20.8-21.4°C, from 4,000 m onwards, temperature is around 21.4-22.2°C.

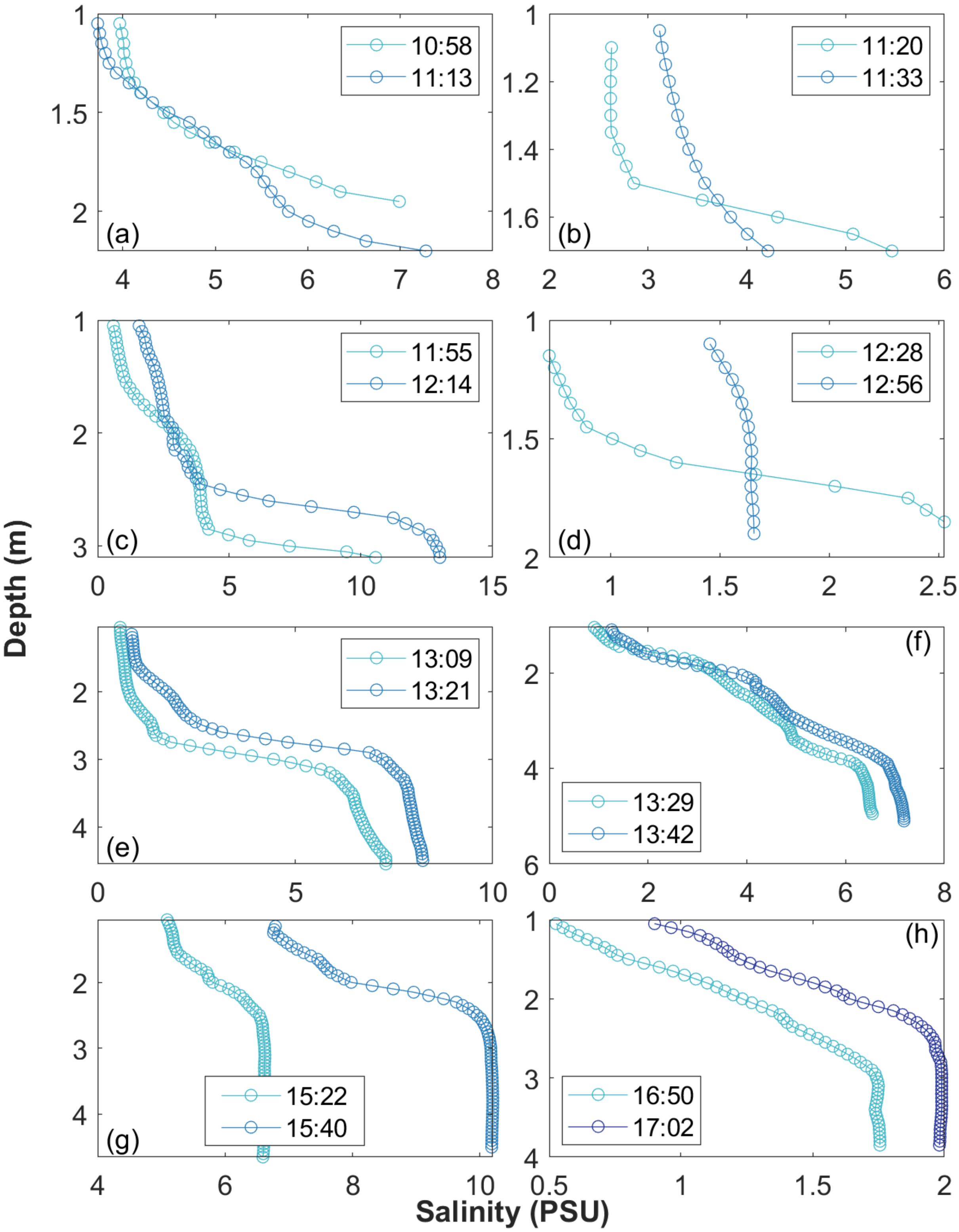

Figure 4.22: Salinity profiles for casts taken in the same location (a) 100 m, (b) 300 m, (c) 1,970 m, (d) 2,965m, (e) 4,058 m, (f) 4,550 m, (g) 7,260 m, (h) 11,570 m.

The plots in Figure 4.22 depict casts that were taken in the same location as the tide was coming into the river. The profiles show the salinity gradually increasing at the site, and the profiles gradually present more exaggerated haloclines. The profiles in Figure 4.22a show similar salinity, and in Figure 4.22d the profile at 12:56 shows less of a salt wedge and more of a mixed water column compared to the profile at 12:28 which shows a significant halocline, although at low salinity. These patterns are again reflected in the density profiles.

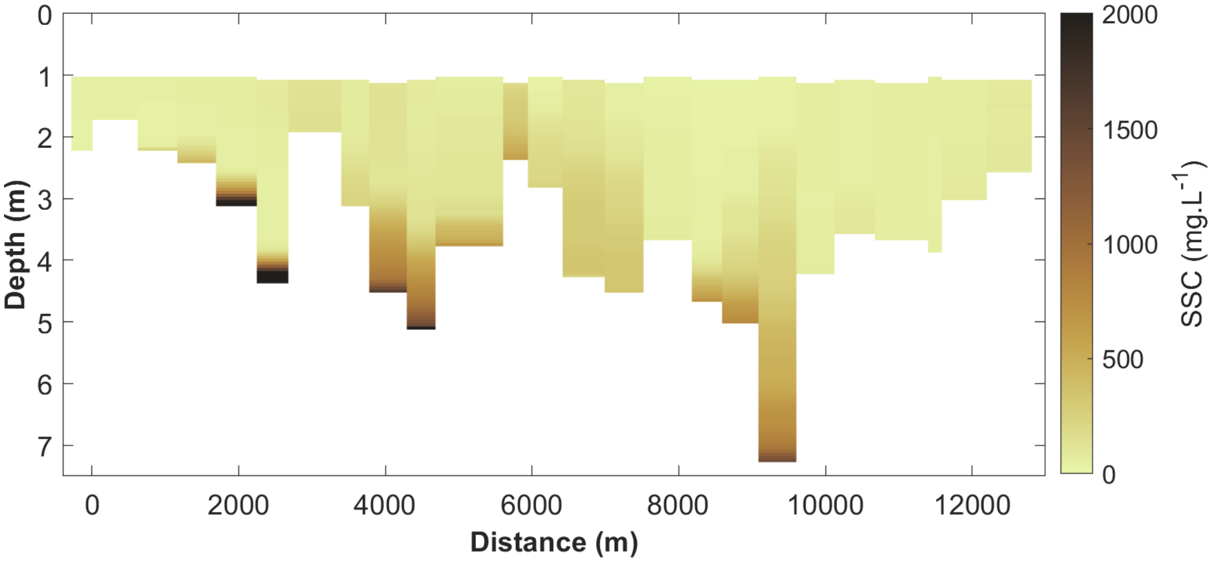

Figure 4.23: Suspended sediment concentration for casts taken on January 18th 2023.

Figure 4.23 shows the suspended sediment concentrations. In general, suspended sediment concentrations throughout the water column were around 0-500 mg L^{-1}, and decreased with distance upriver. Majority of the profiles showed depth-variability with greater sediment concentrations near the bed, up to maximum observed values of 3,500 mg L^{-1}.

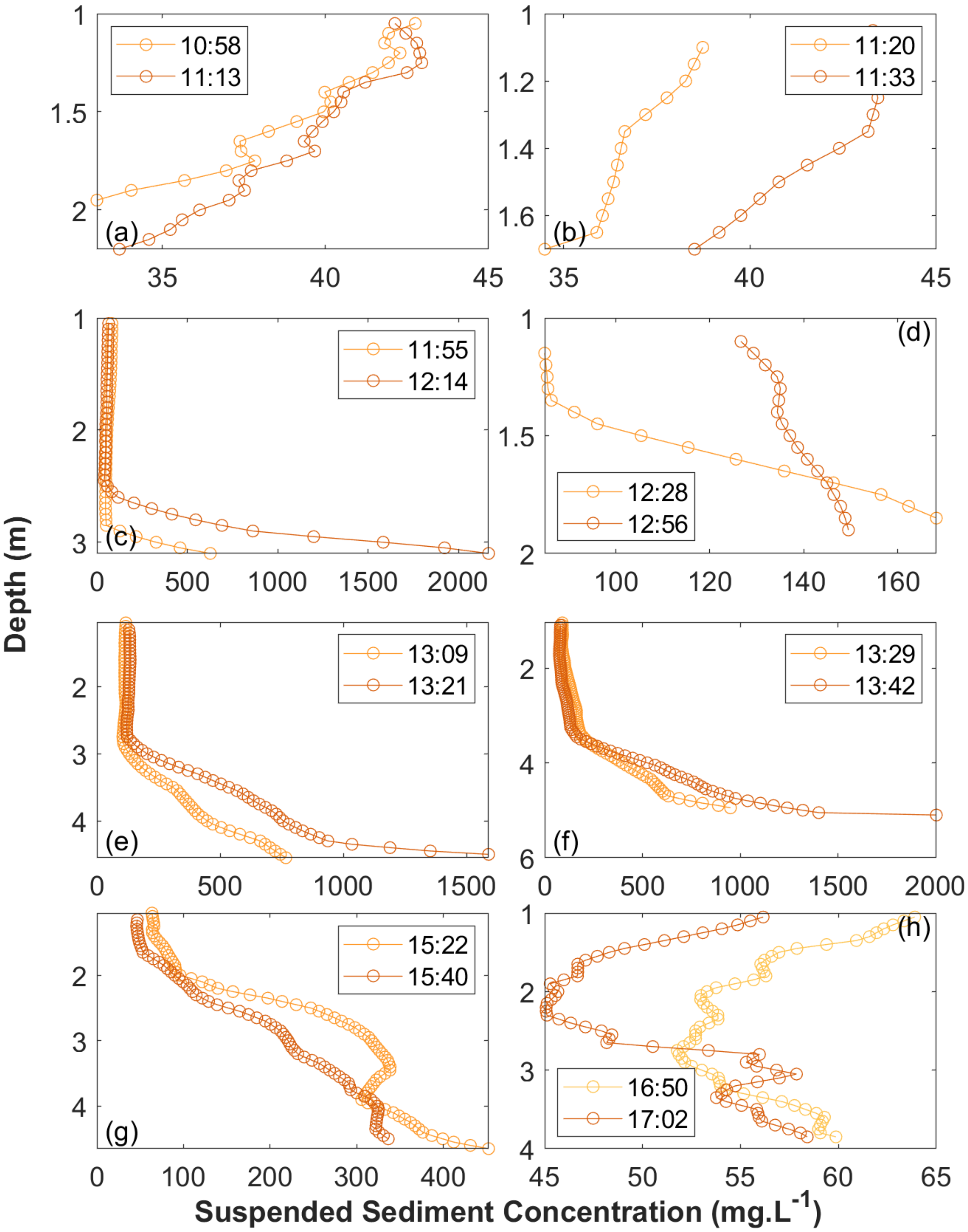

Figure 4.24: Suspended sediment concentrations for casts taken in the same location (a) 100 m, (b) 300 m, (c) 1,970 m, (d) 2,965 m, (e) 4,058 m, (f) 4,550 m, (g) 7,260 m, (h) 11,570 m.

The plots in Figure 4.24 depict casts that were taken in the same location as the tide was coming into the river. Most of the plots show the SSC increasing, as the tide was coming in. The plots also show that SSC tends to be of higher concentration at the bottom of the water column than the surface, which is true for all profiles besides those shown in Figure 4.24a and Figure 4.24b, which have a lower SSC at the bottom of the profile than the surface. The difference however is very small and therefore likely insignificant.

The ExoSonde measurements taken during survey 3 are shown in Figure 4.25, which includes measurements of pH, chlorophyll, fluorescent dissolved organic matter (fDOM), and dissolved oxygen (DO). Observed pH was decreased near the river (0-4,000 m) mouth compared to further upstream (4,000-12,000 m). Chlorophyll was greater within the salinity intrusion particularly near the bed, than in fresh water. Conversely, fDOM was smaller within the salinity intrusion near the bed, than in the fresh water. Observed DO ranged from 60-80% for majority of the estuary, at 6,000 m from the river mouth DO was >80% near the surface. Differences between the surface and near bed were approximately 0.2, 5 $\mu g.L^{-1}$, 1.5 RFU, and 2.5 % for pH, chlorophyll, fDOM, and DO respectively (Figure 4.13).

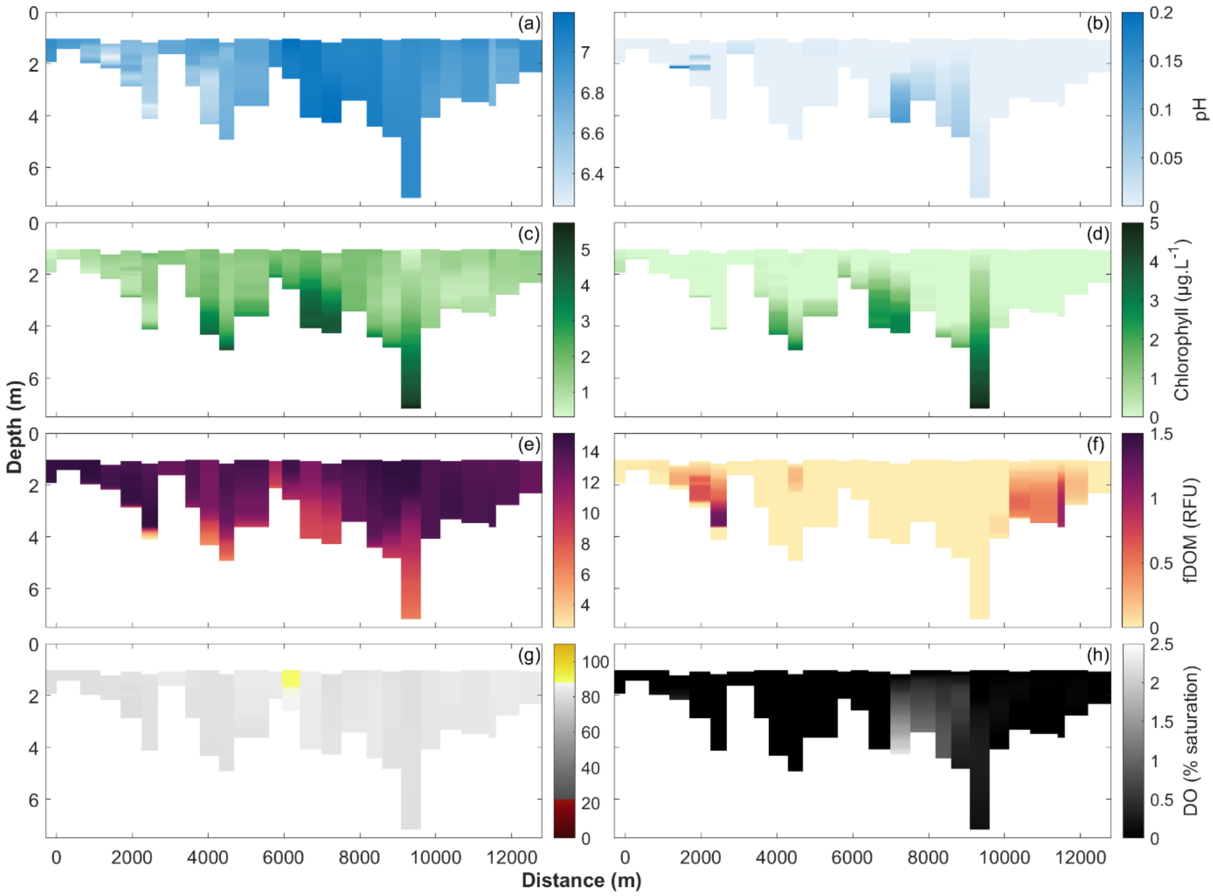

Figure 4.25: Left-hand column: Profiles of (a) pH, (c) chlorophyll, (e) fluorescent dissolved organic matter (fDOM) (g) dissolved oxygen, as a function of distance along the river from survey 3 (January 2023). Right-hand column: Differences from the near-surface value (taken from the highest measurement in water column) of (b) pH, (d) chlorophyll, (f) fDOM, and (h) dissolved oxygen.

4.2.4 Survey 4 (March 2023)

The March survey was focussed on measurements around high tide, with 12 casts taken on the incoming tide, and seven casts subsequently taken on the ebb tide. Two casts were taken at the maximum distance travelled upstream during the March survey, as the flood tide transitioned into an ebbing tide.

Profiles of temperature, salinity and density are shown in Figures 4.26 and 4.27, with maximum differences during the upstream measurements between surface and near-bed of 1.36 PSU, 0.1°C, and 1 kg.m^{-3} respectively, and during the downstream measurements, the differences were 2.58 PSU, 0.02°C, and 2 kg.m^{-3}. In this case, the majority of the profiles of the water column during the march measurements show the estuary as mixed with small differences between the near-bottom and near-surface salinities as previously mentioned.

Figure 4.28 shows maximum salinity for each cast measured during the March survey and shows how far the salinity travelled into the estuary during high tide. 10 PSU reached 5.35 km upstream from the river mouth, 5 PSU reached 8.74 km upstream, and 1 PSU reached 9.85 km upstream with that being the furthest measurement upstream.

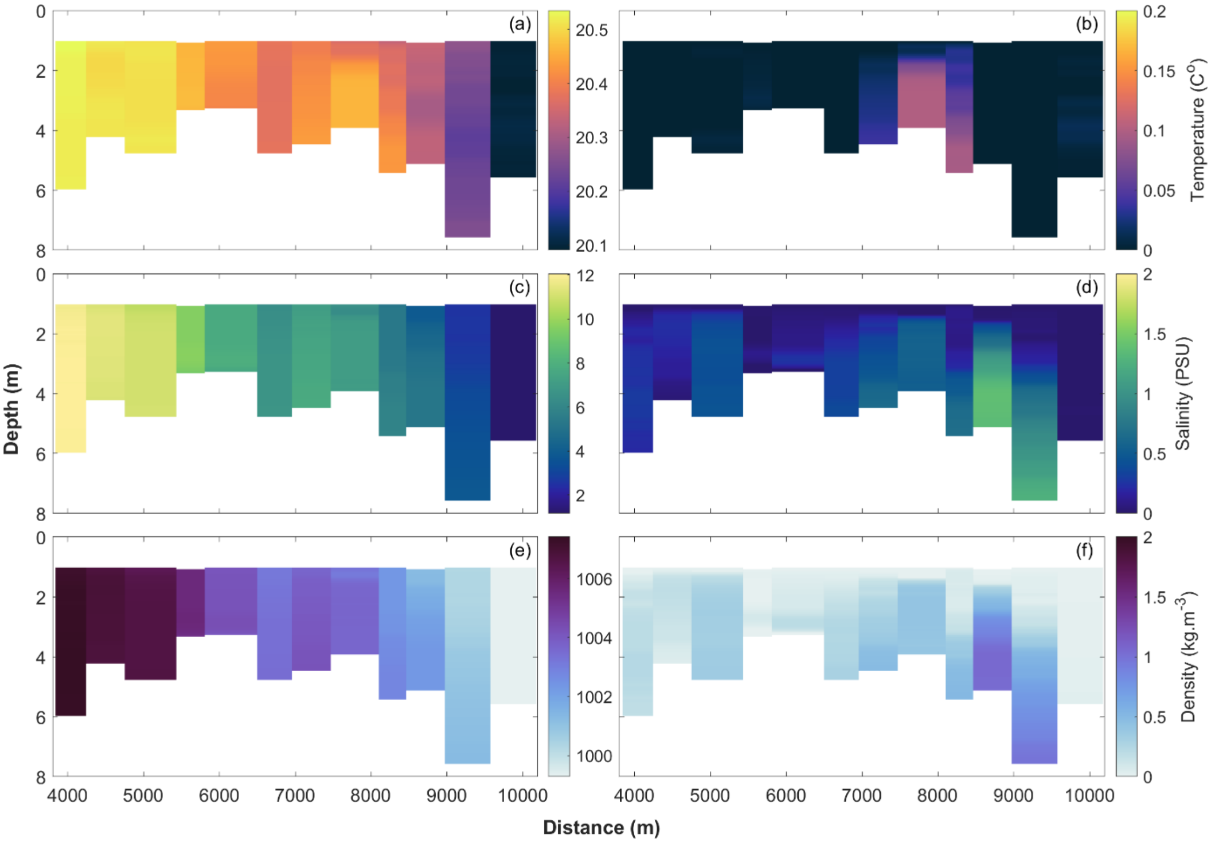

Figure 4.26: Left-hand column: Profiles of (a) temperature, (c) salinity, (e) density, as a function of distance along the river from survey 4 (March 2023) upriver measurements. Right-hand column: Differences from the near-surface value (taken from the highest measurement in water column) of (b) temperature, (d) salinity, and (f) density.

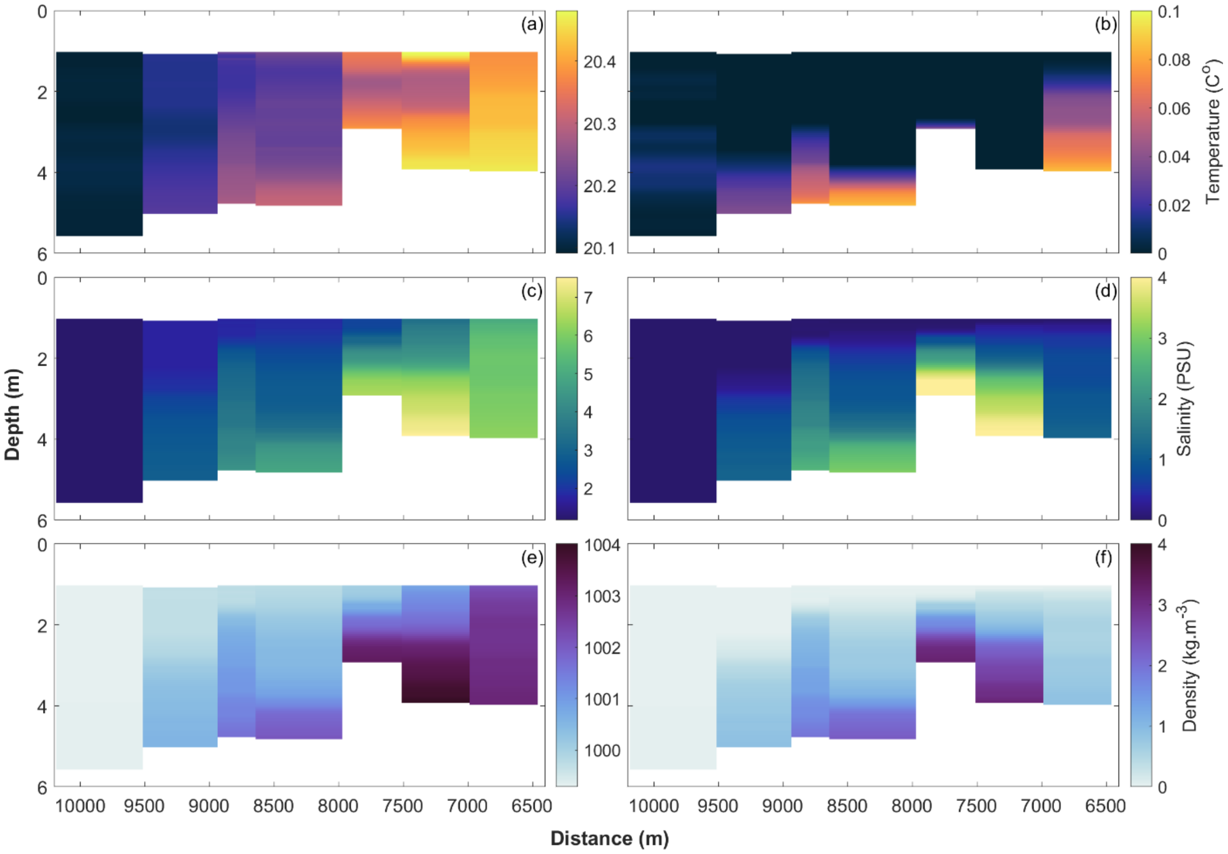

Figure 4.27: Left-hand column: Profiles of (a) temperature, (c) salinity, (e) density, as a function of distance along the river from survey 4 (March 2023) downriver measurements. Right-hand column: Differences from the near-surface value (taken from the highest measurement in water column) of (b) temperature, (d) salinity, and (f) density.

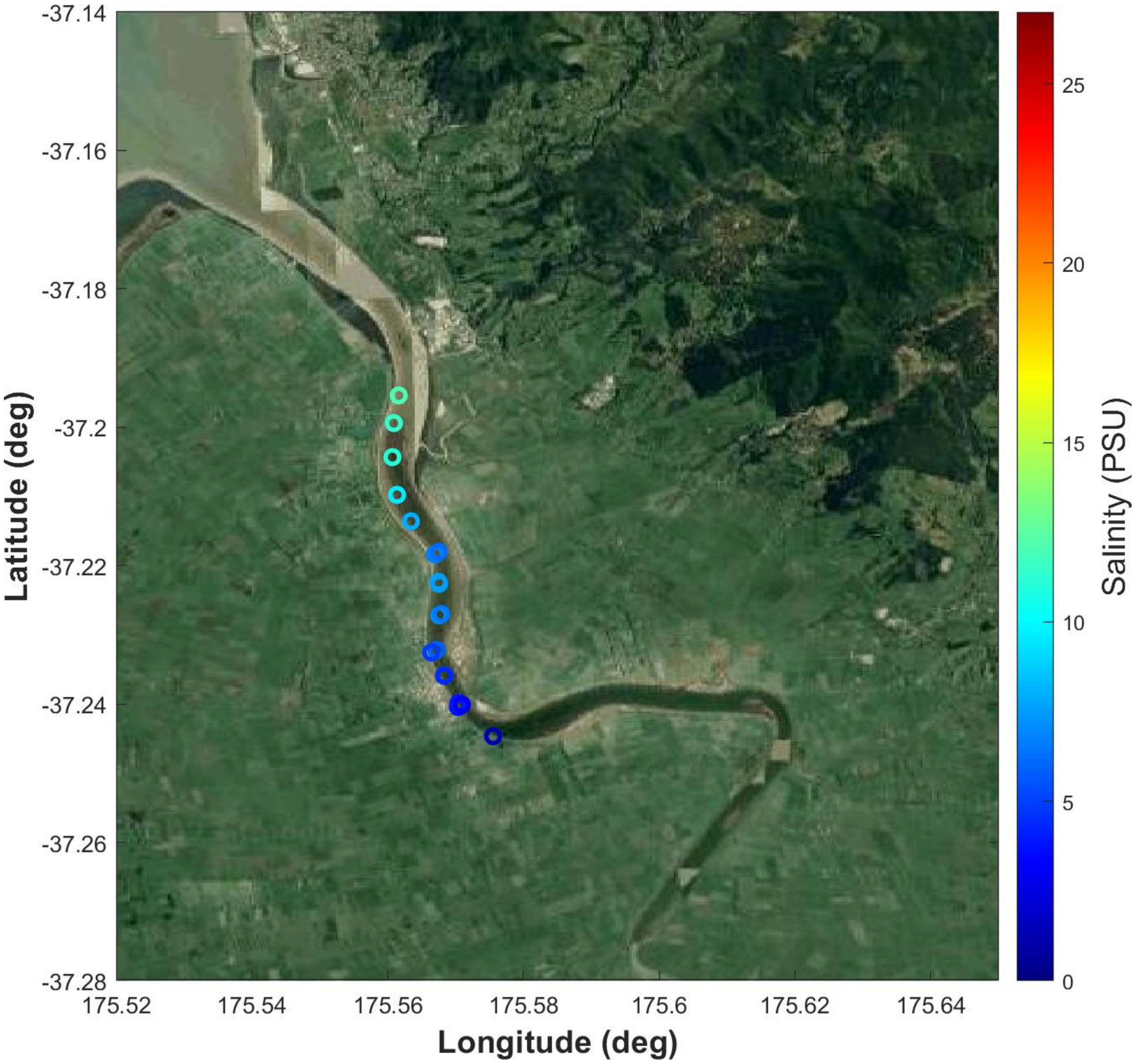

Figure 4.28: Points of maximum salinity measured at each site at the Waihou River, on a satellite image from Google Earth, for the March run.

For measurements taken during the upstream section of the survey, observed salinities from distances of 4,000 to 5,500 m from the river mouth are around 10-12 PSU, observed densities were ~1,007 kg.m^{-3} and observed temperatures were 20.5°C, around 5-10 PSU, 1,004-1,006 kg.m^{-3} and 20.2-20.5°C at 5,500 to 9,000 m upstream from the river mouth. Beyond 9,000 m, observed salinities are less than 4 PSU, observed densities gradually decrease from 1,004 kg.m^{-3} and observed temperatures were less than 20.2°C. For measurements taken during the downstream section of the survey, observed salinities from 6,500 to 8,000 m upriver from the mouth is up to 7 PSU, observed densities are up to 1,004 kg.m^{-3} and observed temperatures were 20.3-20.4°C, 4-7 PSU, 1,001-1,004 kg.m^{-3} and 20.2-

20.3°C around 8,000 to 9,500 m, beyond 9,500 m observed salinity is less than 3 PSU, observed density is less than 1,001 kg.m^{-3} and observed temperature is less than 20.2°C.

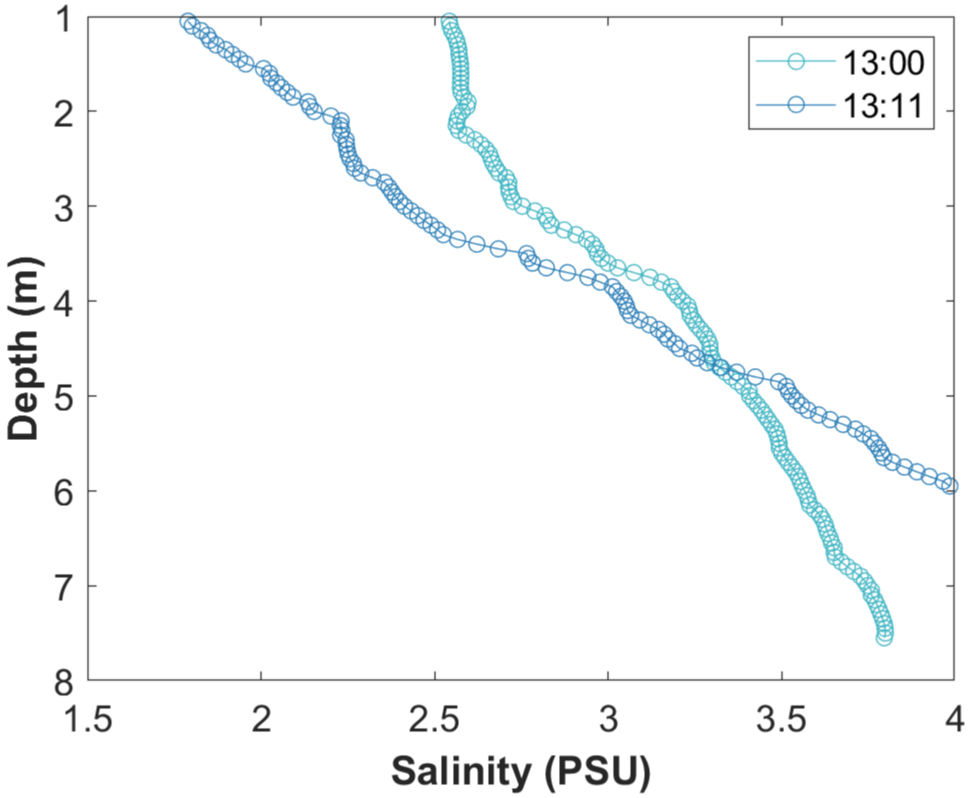

Figure 4.29: Salinity profiles for casts taken in the same position ~9,240 m, at the furthest point upstream, for March 13th 2023.

The profiles in Figure 4.29 are taken in the same location at the farthest position upstream during the March survey. The casts were taken as the tide was turning from flood to ebb. The cast taken at 13:11 has a more exaggerated halocline, with a difference of 2.5 PSU from the surface to near-bed, compared to the cast taken at 13:00 which has a difference of 1 PSU from surface to near bed. The density profiles for the same casts shown in Figure 4.29 follow the same pattern as the salinity profiles. Density ranges from 999.5-1,001.5 kg.m^{-3}.

As shown in Figure 4.30, it is observed that the water column becomes more stratified, and salinity decreases during ebb tide compared to flood tide.

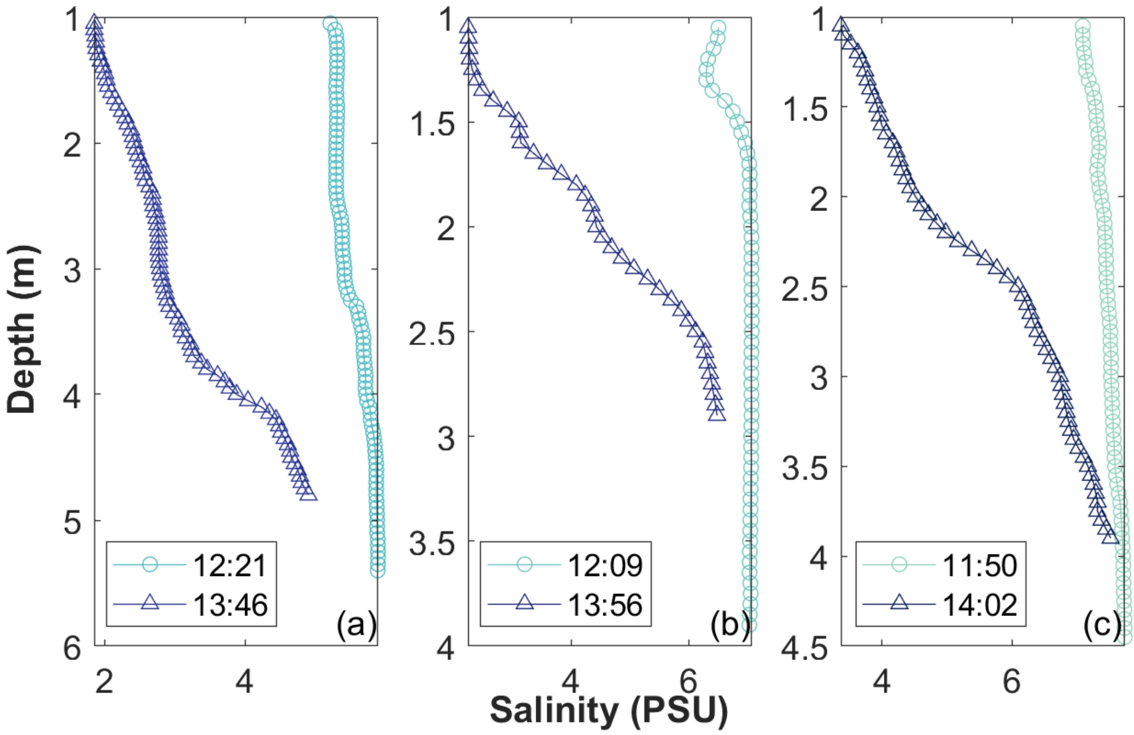

Figure 4.30: Salinity profiles taken in the same location (a)~8,320 m, (b)~7,740 m, (c) 7,230 m, showing a profiles taken during flood tide (circles) and ebb tide (triangles).

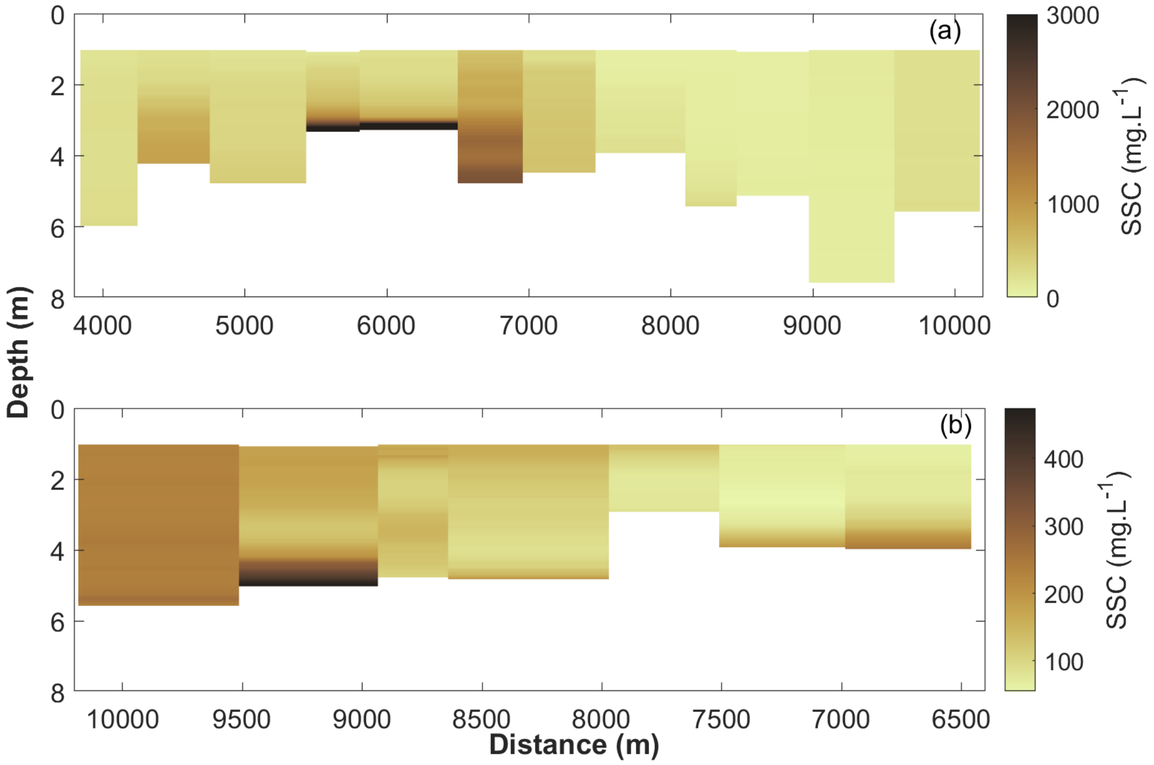

Figure 4.31: Suspended sediment concentration for casts taken while travelling upstream (a), and from casts taken while travelling downstream (b). Measurements taken on March 13th 2023.

Figure 4.31 shows the suspended sediment concentrations observed in the profiles of the casts. In Figure 4.31a, suspended sediment concentrations throughout the water column are generally 0 to 1,000 mg L^{-1}, decreasing with distance upstream. Half of the profiles show depth-variability with increased sediment concentrations near the bed. The maximum observed concentration is around 5,500 mg L^{-1}. In Figure 4.31b, suspended sediment concentrations throughout the water column are generally 100-300 mg L^{-1} decreasing concentrations downstream. Concentrations within the water column are variable. The maximum observed concentration is around 450 mg L^{-1}.

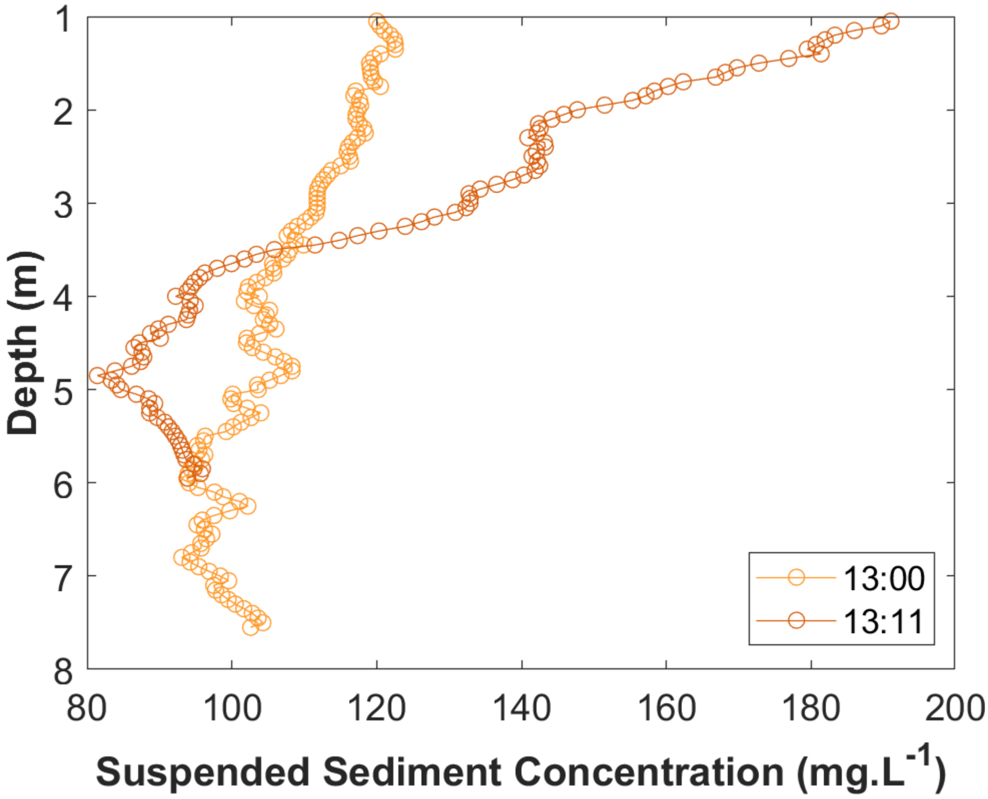

Figure 4.32: Suspended sediment concentration calculated from voltage 1 taken at the same location ~9,240 m at the furthest point upstream, for March 13th 2023.

The profiles in Figure 4.32 show casts taken in the same location at the furthest point upstream as the tide was turning from flood to ebb tide. Concentrations for the majority of the water column is between 80-180 mg L^{-1} with the cast taken at 13:11 showing a larger difference between surface and near bottom SSC compared to the cast taken at 13:00.

The ExoSonde upriver measurements taken during survey 4 are shown in Figure 4.33, which includes measurements of pH, chlorophyll, fluorescent dissolved organic matter (fDOM), and dissolved oxygen

(DO). Observed pH and chlorophyll was greater within the salinity intrusion, than in fresh water. Conversely, fDOM was smaller within the salinity intrusion than the fresh water. Observed DO ranged from 60-80%. Differences between the surface and near bed were approximately 0.1, 3 µg.L^{-1}, 4 RFU, and 2 % for pH, chlorophyll, fDOM, and DO respectively (Figure 4.33).

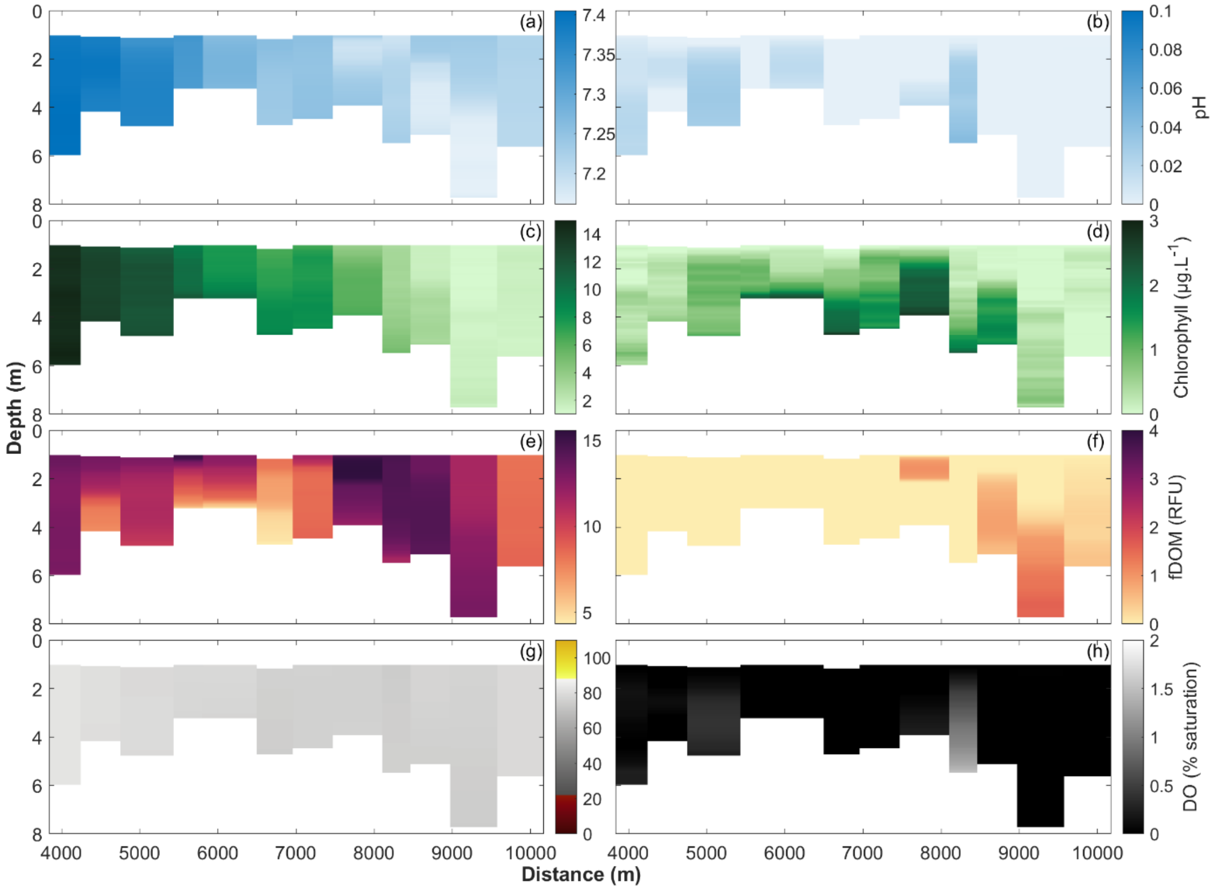

Figure 4.33: Left-hand column: Profiles of (a) pH, (c) chlorophyll, (e) fluorescent dissolved organic matter (fDOM) (g) dissolved oxygen, as a function of distance along the river from survey 4 (March 2023) upriver measurements. Right-hand column: Differences from the near-surface value (taken from the highest measurement in water column) of (b) pH, (d) chlorophyll, (f) fDOM, and (h) dissolved oxygen.

The ExoSonde measurements which were taken when travelling downriver during survey 4 are shown in Figure 4.34, which includes measurements of pH, chlorophyll, fluorescent dissolved organic matter (fDOM), and dissolved oxygen (DO). Observed pH decreased with distance downstream, conversely, chlorophyll and fDOM increased with distance downstream. Observed DO ranged from 60-80%.

Differences between the surface and near bed were approximately 0.1, 5 µg.L^{-1}, 4 RFU, and 0 % for pH, chlorophyll, fDOM, and DO respectively (Figure 4.34).

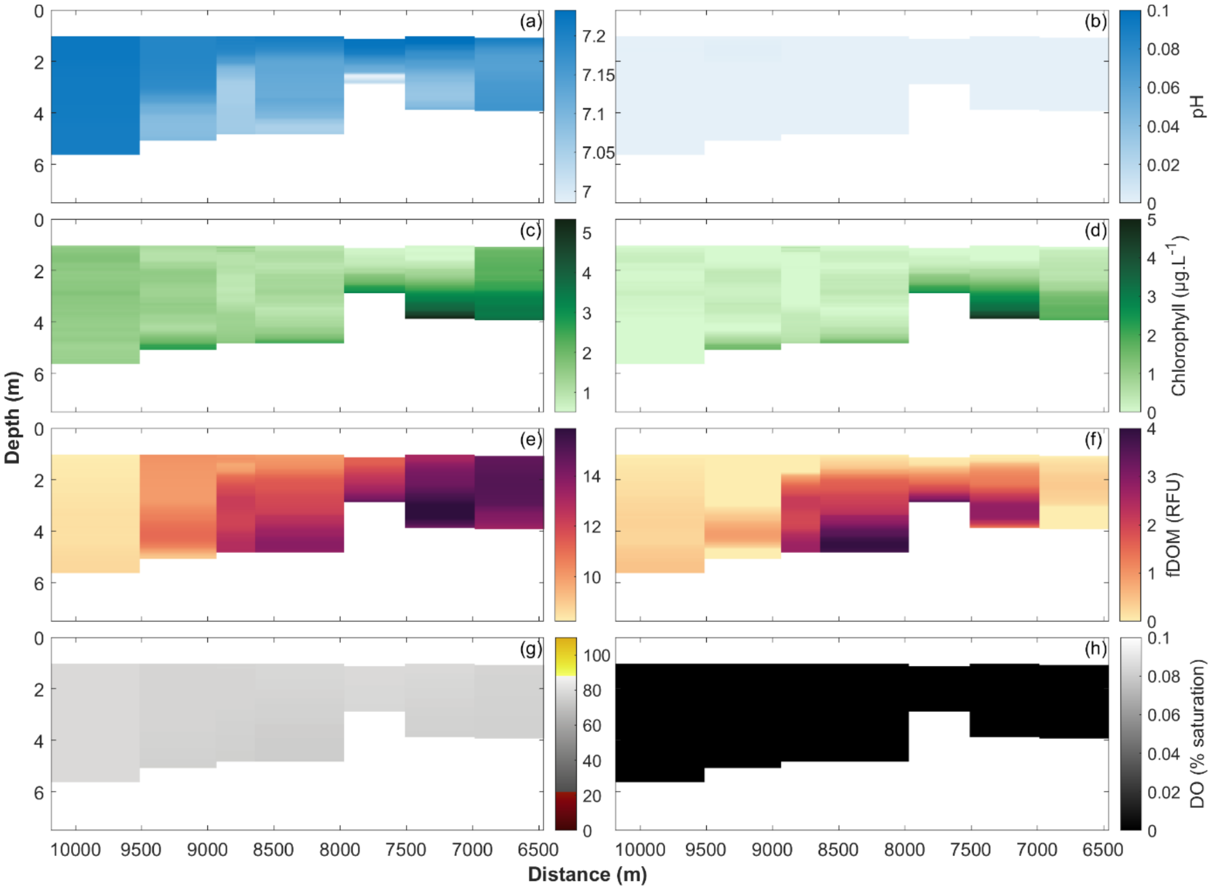

Figure 4.34: Left-hand column: Profiles of (a) pH, (c) chlorophyll, (e) fluorescent dissolved organic matter (fDOM) (g) dissolved oxygen, as a function of distance along the river from survey 4 (March 2023) downriver measurements. Right-hand column: Differences from the near-surface value (taken from the highest measurement in water column) of (b) pH, (d) chlorophyll, (f) fDOM, and (h) dissolved oxygen.

4.2.5 Survey 5 (April 2023)

The April survey was taken during the ebb phase of the tidal cycle. A few initial CTD casts were taken heading upriver as the tide receded in the opposite direction. These casts allowed for the maximum extent of the salt intrusion to be identified, with the cast at 10,000 m revealing the entire water column was fresh water (Figure 4.35). Casts were subsequently taken whilst heading downriver and show the freshening of the water column with both time and distance (thus the salt intrusion receded at a faster velocity than the boat speed).

Profiles of temperature, salinity and density are shown in Figures 4.35 and 4.36, with maximum differences between surface and near-bed, for the upstream measurements, of 3.6 PSU, 0.07°C, and 2.8 kg.m^{-3} respectively, and differences of 8 PSU, 0.05°C, and 8 kg.m^{-3} for the downstream measurements. Several casts were taken in the same location, these profiles can be seen in Figure 4.38. In this case, a weak stratification is present during the start of the ebbing tide, while there is stronger stratification as the tide is strongly receding. Figure 4.37 shows maximum salinity for each cast measured during the April field visit and shows how far the salinity travelled into the estuary at the peak of high tide. 10 PSU reached 7.56 km upstream from the mouth of the river, 5 PSU reached 8.98 km upstream, and 1 PSU reached about 9.75-10 km upstream from the mouth of the river. The furthest measurement up stream was at 9.75 km with 1.3-2.5 PSU.

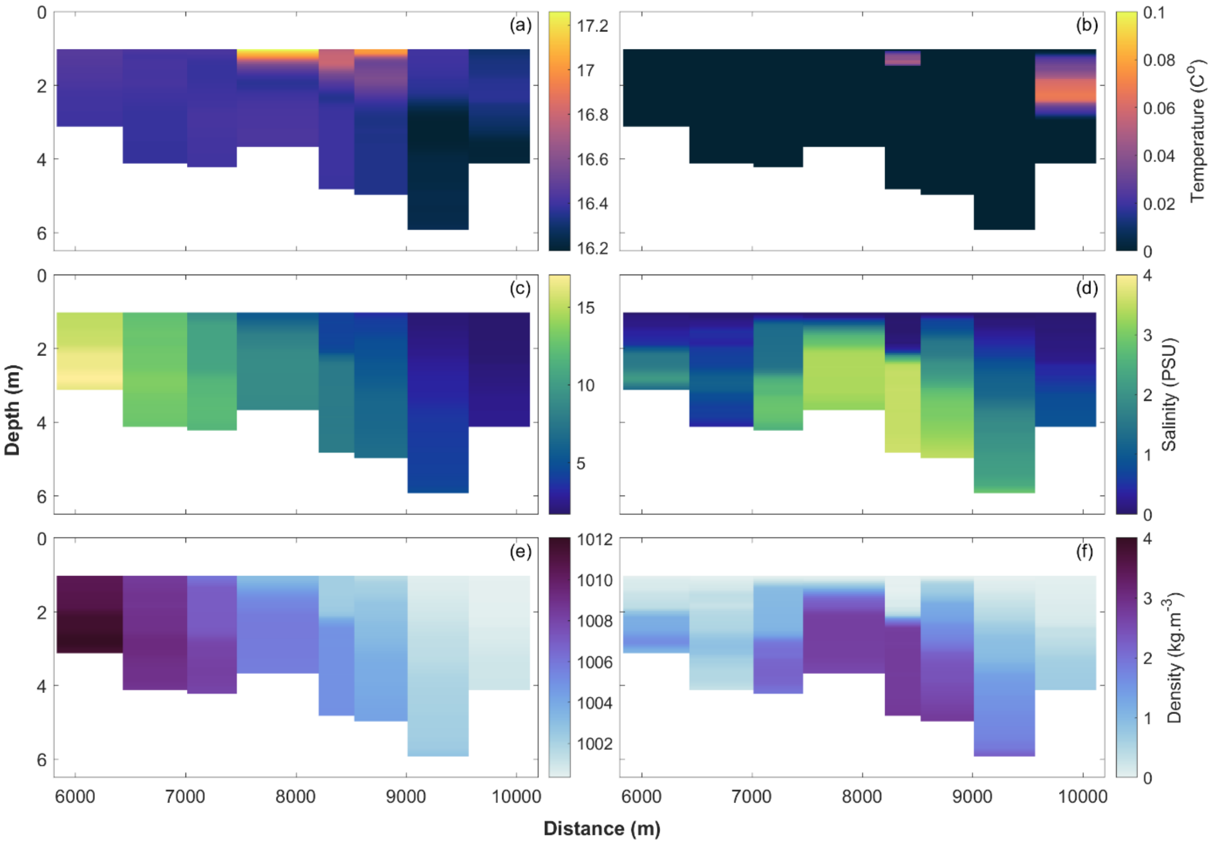

Figure 4.35: Left-hand column: Profiles of (a) temperature, (c) salinity, (e) density, as a function of distance along the river from survey 5 (April 2023) upriver measurements. Right-hand column: Differences from the near-surface value (taken from the highest measurement in water column) of (b) temperature, (d) salinity, and (f) density.

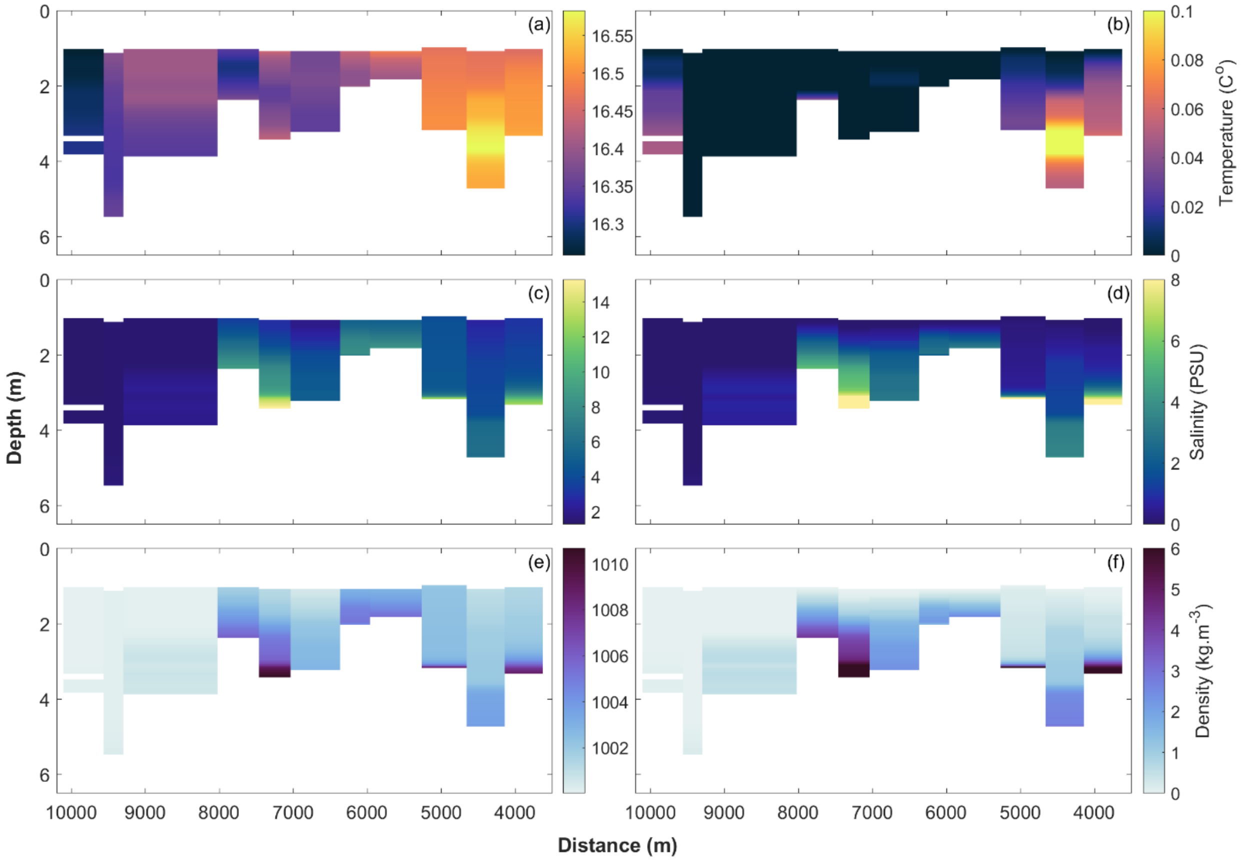

Figure 4.36: Left-hand column: Profiles of (a) temperature, (c) salinity, (e) density, as a function of distance along the river from survey 5 (April 2023) downriver measurements. Right-hand column: Differences from the near-surface value (taken from the highest measurement in water column) of (b) temperature, (d) salinity, and (f) density.

For measurements taken during the upstream section of the survey, observed salinities from 6,000 to 7,000 m upriver from the mouth were around 10-15 PSU, observed densities were 1,008 to 1,012 kg.m^{-3} and observed temperatures were 16.4°C, from 7,000 to 9,000 m around 5-10 PSU, density gradually decreases from 1,008 to 1,002 kg.m^{-3} and temperature was 16.4-17.2°C with larger temperatures at the surface of the water. Beyond 9,000 m, observed salinity is below 5 PSU, observed density is below 1,002 kg.m^{-3} and observed temperatures are 16.2-16.4 with higher temperatures observed near the surface.

For measurements taken during the downstream section of the survey, observed salinities beyond 8,000 m are below 5 PSU and observed densities are below 1,000 kg.m^{-3}, from distances of 4,000 to 8,000 m salinity is 5-15, with higher salinity observed near the bed and lower salinity observed near the surface, and density varies from 1,002 to 1,010 kg.m^{-3} with heaviest densities located at the bottom of the water profiles. Observed temperatures beyond 9,500 m are below 16.35°C, from distances 5,000 to 9,500 m from the river mouth around 16.35-16.45°C, and from 4,000 to 5,000 m observed temperature is around 16.45-16.55°C.

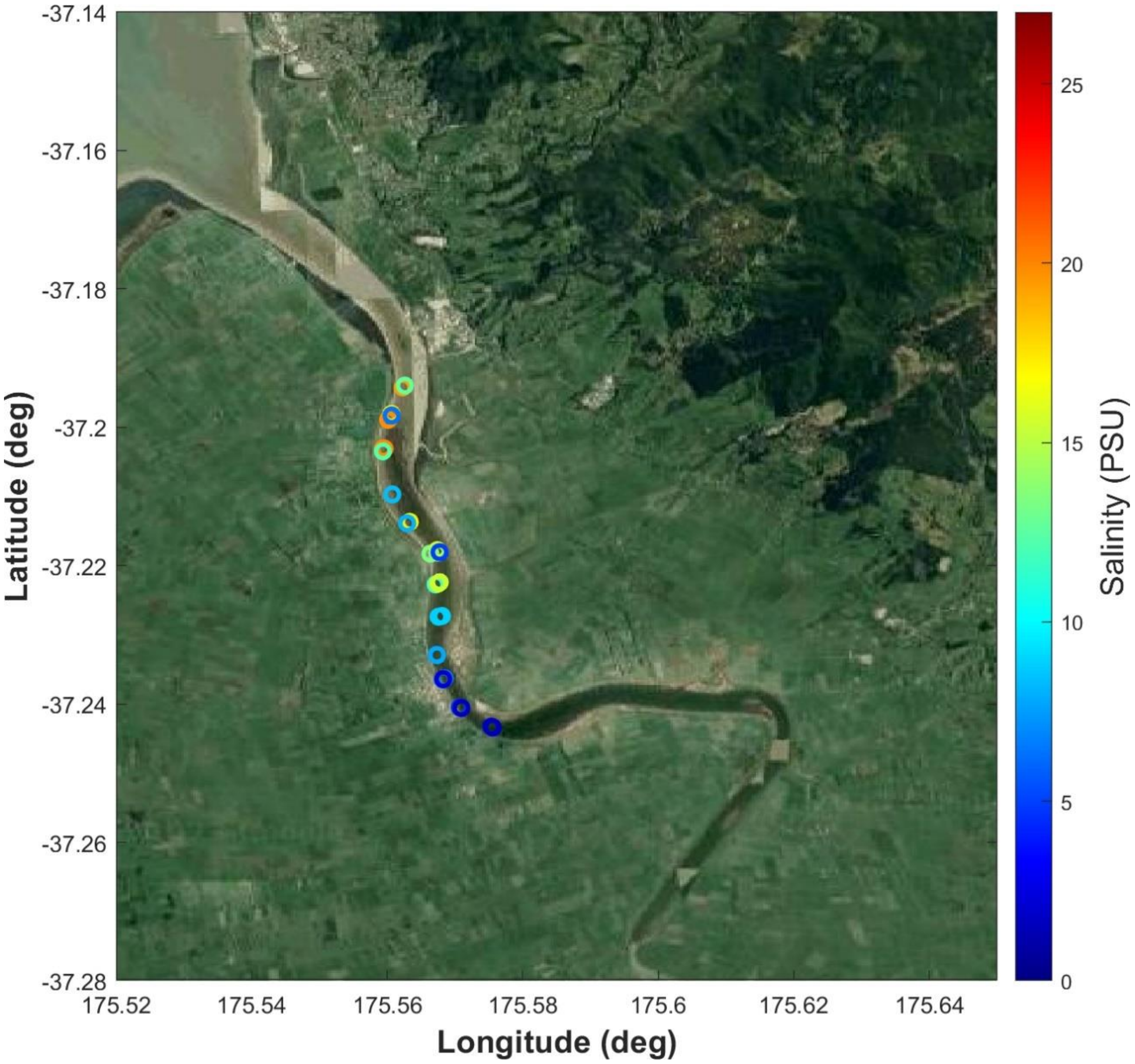

Figure 4.37: Points of maximum salinity measured at each site at the Waihou River, on a satellite image from Google Earth, for the April run.

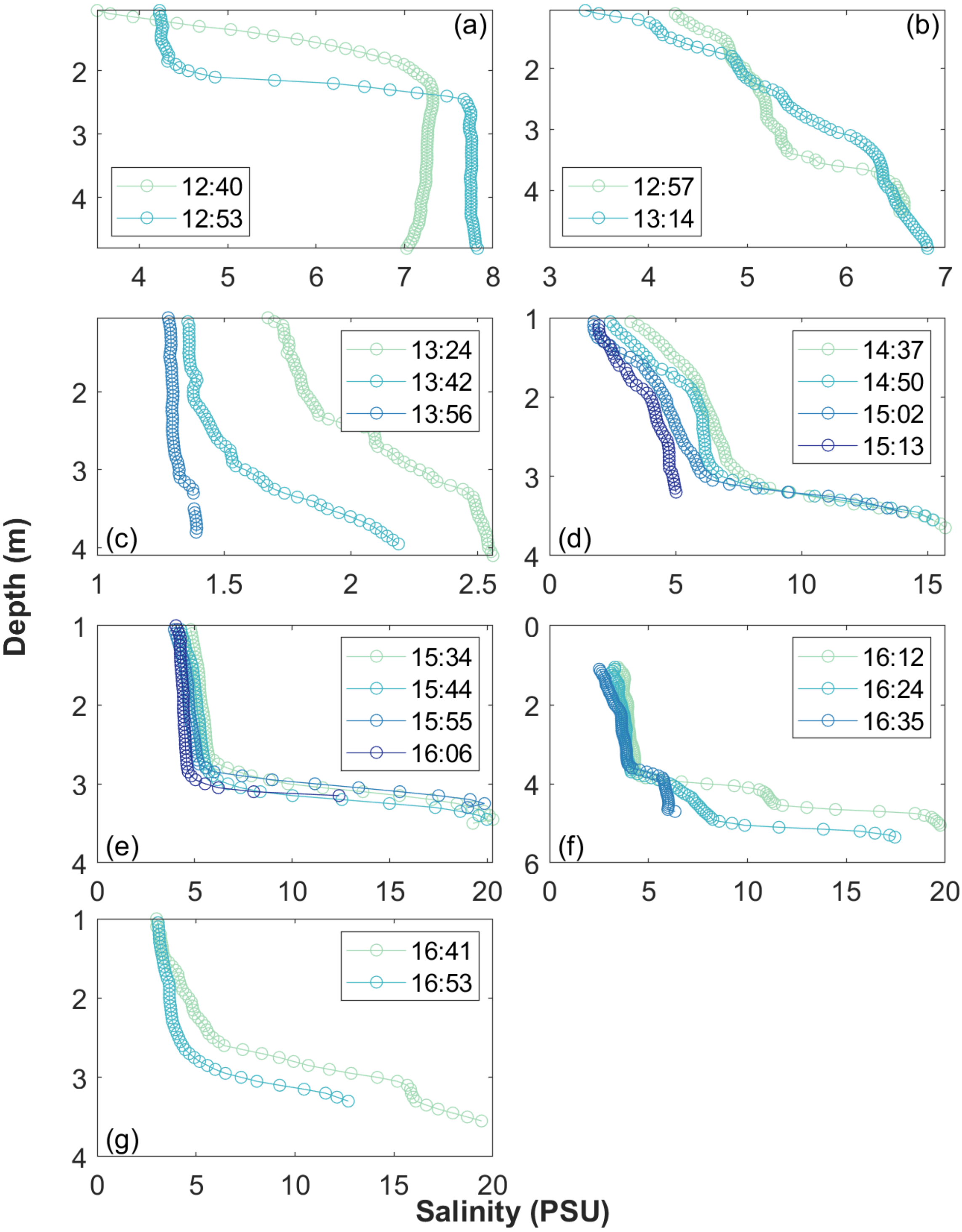

Figure 4.38: Salinity profiles for casts taken in the same location (a) 8,395 m, (b) 8,790 m, (c) 9,835 m, (d) 6,725 m, (e) 4,930 m, (f) 4,420 m, (g) 3,900 m.

The plots in 43 depict profiles of casts that were taken in the same location. The casts in Figure 4.38a and b were taken while travelling upstream, the casts in Figure 4.38c were taken at the maximum distance travelled, and when the salinity intrusion started to retreat, and the casts in Figure 4.38d, e, f, and g were taken while travelling downstream, following the retreat of the salinity intrusion.

As shown in Figure 4.38a and b, the haloclines become more exaggerated with time. The halocline in the cast taken at 13:14 has moved up in the water column, compared to the cast taken at 12:57, meaning the thickness of the salt wedge has increased, as the salt intrusion is moving into the estuary. As shown in Figure 4.38c the salinity is reducing over time as the salt intrusion is retreating. The last 4 plots contain casts that were taken while travelling downstream. For plots d, e, f, and g, the profiles depict the salinity reducing over time as the salinity intrusion retreats from the estuary.

The density profiles for the same casts shown in Figure 4.38 follow the same patterns as the salinity profiles. Density ranges from 1,002-1,005 kg.m^{-3} for plot a, 1,002-1,004 kg.m^{-3} for plot b, 1,000-1,001 kg.m^{-3} for plot c, 1,000-1,010 kg.m^{-3} for plot d, and 1,000-1,015 kg.m^{-3} for plots e, f, and g. As shown in Figure 4.39, it is observed that the salinity decreases during ebb tide compared to flood tide.

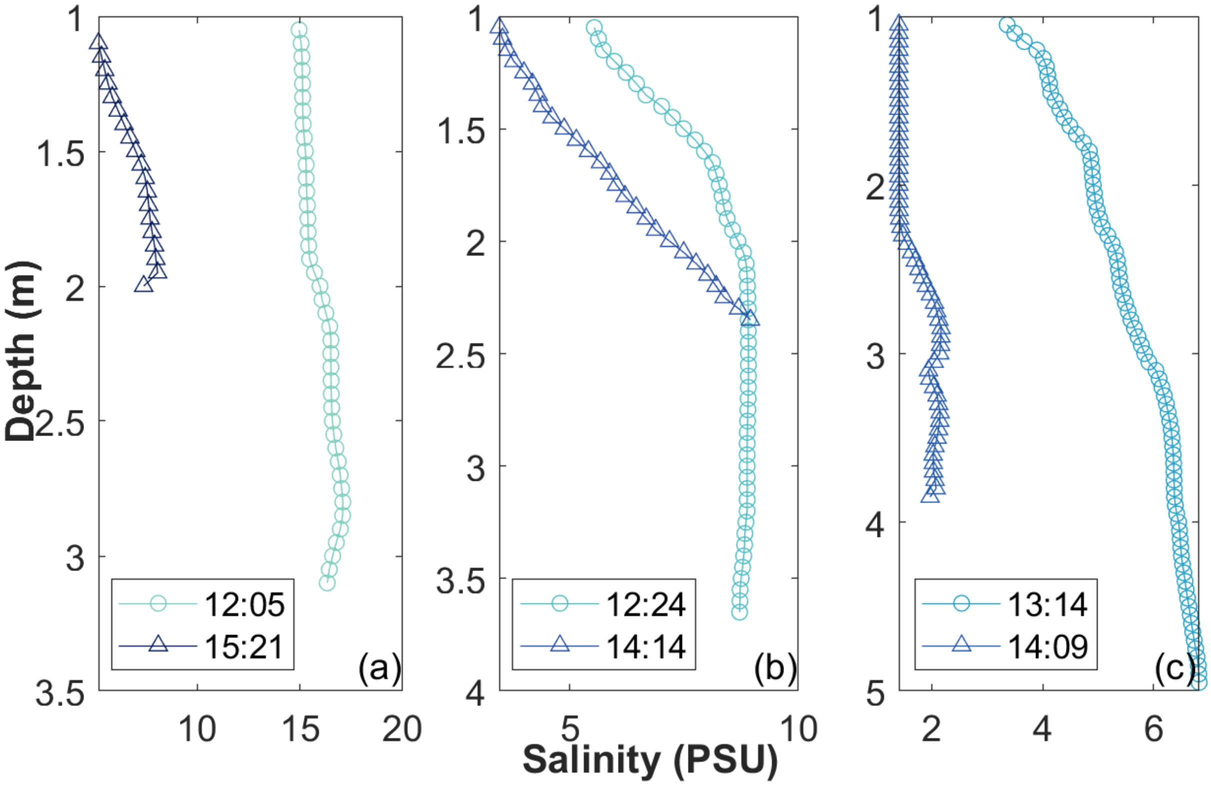

Figure 4.39: Salinity profiles for casts taken at the same location (a)~6,125 m, (b)~7,765 m, (c)~8,785, showing a profiles taken at flood tide (circles),and ebb tide (triangles).

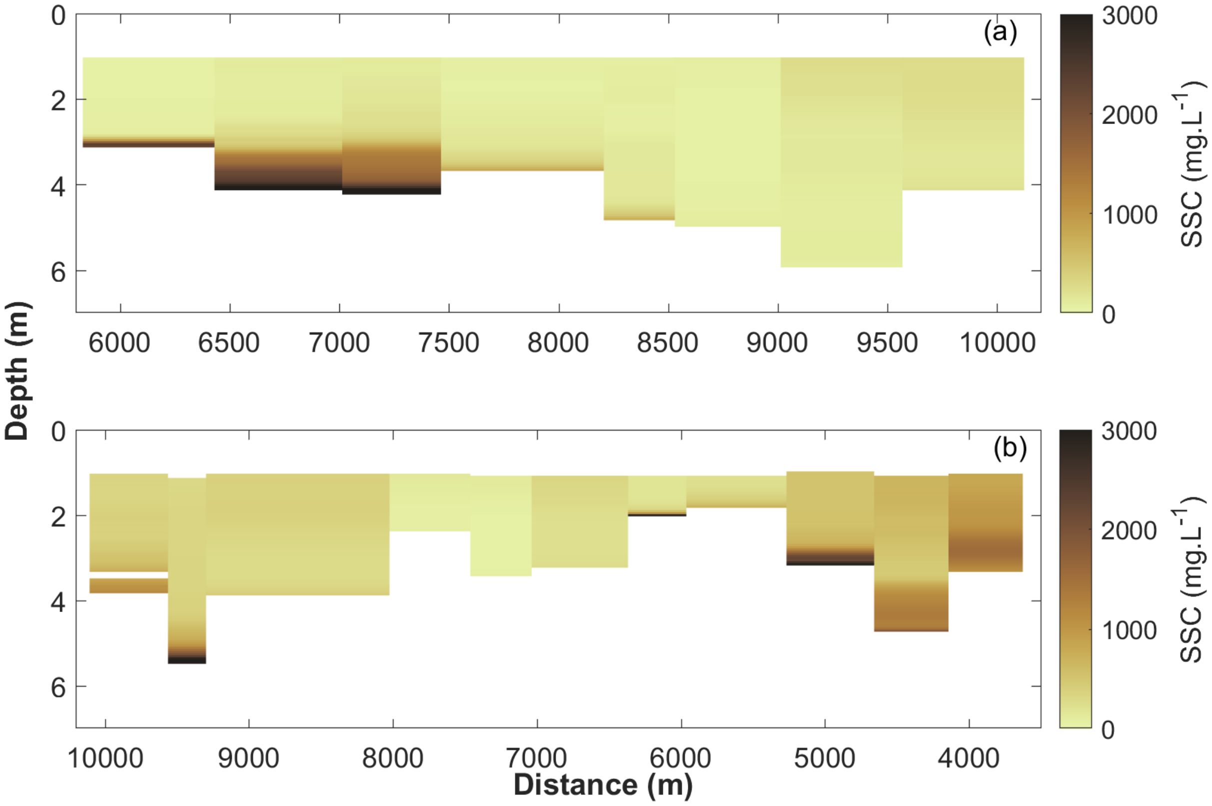

Figure 4.40: Suspended sediment concentration for casts taken while travelling upstream (a) and casts taken while travelling downstream (b). Measurements taken on April 27th 2023.

Figure 4.40 shows the suspended sediment concentrations observed in the profiles of the casts. In Figure 4.40a, suspended sediment concentrations throughout the water column are generally around 0-500 mg L^{-1}, decreasing with distance upstream. Half of the profiles show depth-variability with greater sediment concentrations near the bed. Maximum observed values were around 5,500 mg L^{-1}. In Figure 4.40b, suspended sediment concentrations throughout the water column were around 0-1,500 mg L^{-1}. There is an increase in concentrations downstream. Again, there is depth-variability exhibited, with greater concentrations near the bed. Maximum observed concentrations were around 7,000 mg L^{-1} from near-bed values.

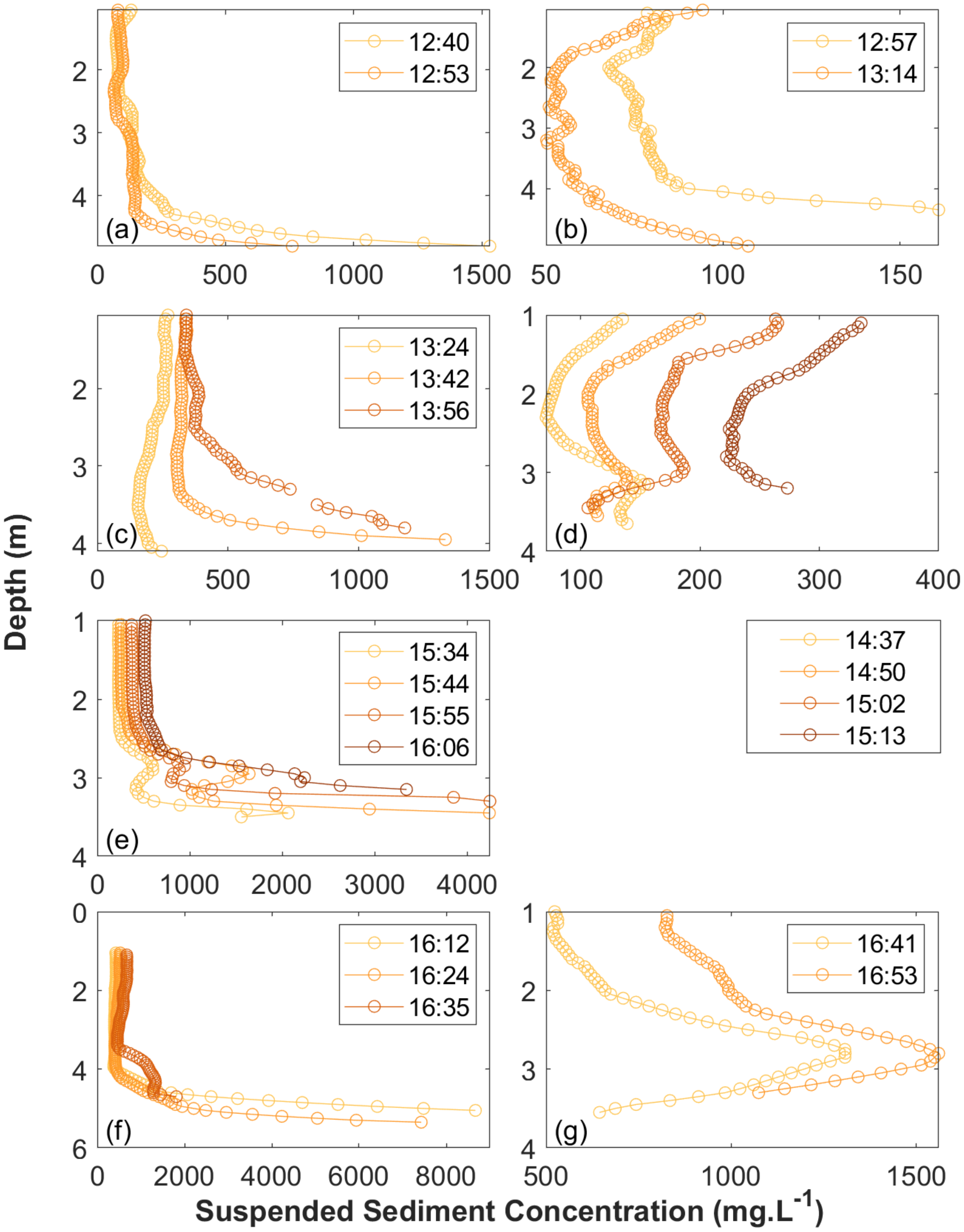

Figure 4.41: Suspended sediment concentration calculated from voltage 1 for casts taken in the same location (a) 8,395 m, (b) 8,790 m, (c) 9,835 m, (d) 6,725 m, (e) 4,930 m, (f) 4,420 m, (g) 3,900 m.

The plots in Figure 4.41 depict cast profiles that were taken in the same location. The casts in Figure 4.41a and b were taken while travelling upstream, the casts in Figure 4.41c were taken at the maximum distance travelled, and when the salinity intrusion started to retreat, and the casts in Figure 4.41d, e, f, and g were taken while travelling downstream, following the retreat of the salinity intrusion. The majority of the profiles show that the bottom of the water column has higher SSC than the surface. In Figure 4.41c, d, e, f, and g, SSC is increasing with time.

The ExoSonde upriver measurements taken during survey 5 are shown in Figure 4.42, which includes measurements of pH, chlorophyll, fluorescent dissolved organic matter (fDOM), and dissolved oxygen (DO). Observed pH and chlorophyll was greater within the salinity intrusion, than in fresh water. Conversely, fDOM was smaller within the salinity intrusion than the fresh water. Observed DO saturations ranged from 60-80%. Differences between the surface and near bed were approximately 0.2, 10 µg.L^{-1}, 4 RFU, and 0.6 % for pH, chlorophyll, fDOM, and DO respectively (Figure 4.42).

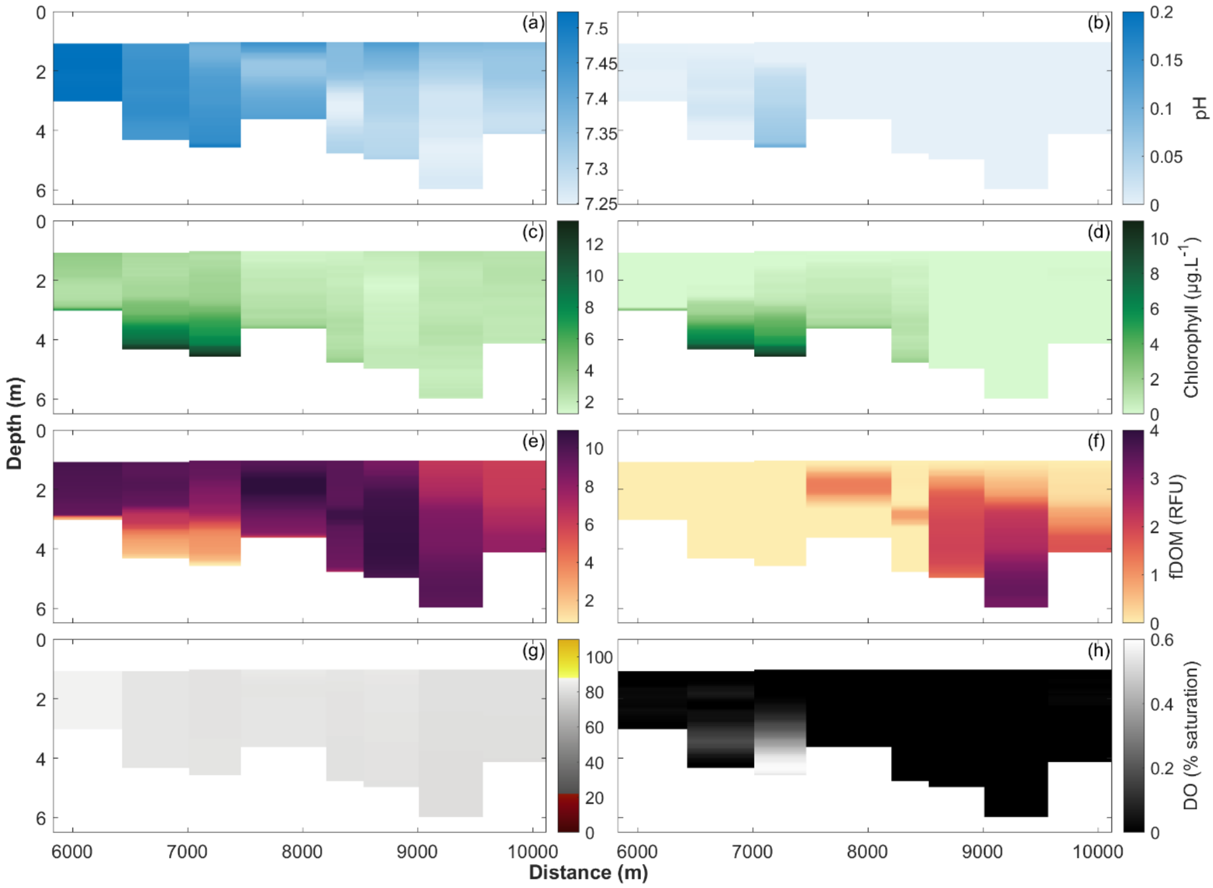

Figure 4.42: Left-hand column: Profiles of (a) pH, (c) chlorophyll, (e) fluorescent dissolved organic matter (fDOM) (g) dissolved oxygen, as a function of distance along the river from survey 5 (April 2023) upriver measurements. Right-hand column: Differences from the near-surface value (taken from the highest measurement in water column) of (b) pH, (d) chlorophyll, (f) fDOM, and (h) dissolved oxygen.

The ExoSonde measurements taken while travelling downriver during survey 5 are shown in Figure 4.43, which includes measurements of pH, chlorophyll, fluorescent dissolved organic matter (fDOM), and dissolved oxygen (DO). Observed pH was smaller within the salinity intrusion near the bed compared to freshwater, conversely, chlorophyll and fDOM was greater within the salinity intrusion, than in fresh water. Observed DO ranged from 60-80%. Differences between the surface and near bed were approximately 0.3, 8 μg.L^{-1}, 3 RFU, and 0.01 % for pH, chlorophyll, fDOM, and DO respectively (Figure 4.43).

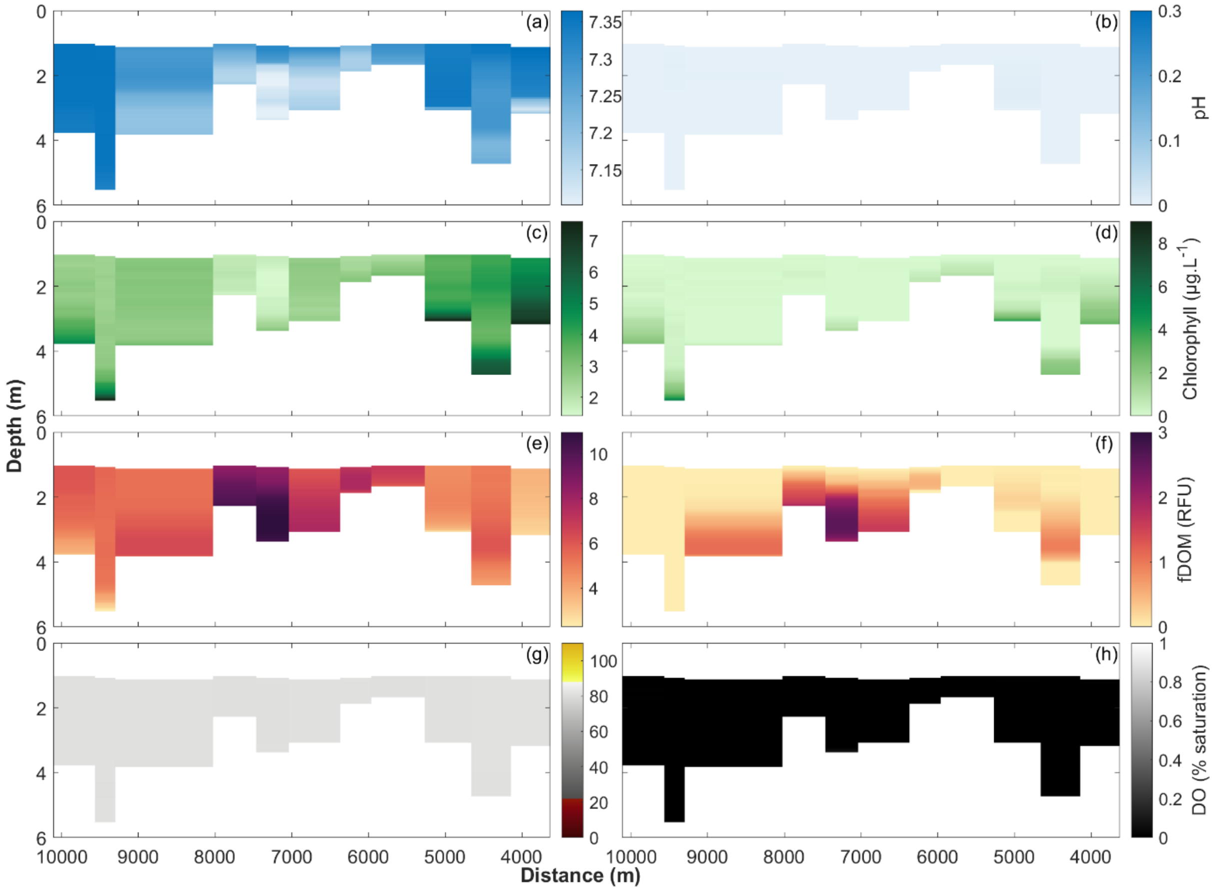

Figure 4.43: Left-hand column: Profiles of (a) pH, (c) chlorophyll, (e) fluorescent dissolved organic matter (fDOM) (g) dissolved oxygen, as a function of distance along the river from survey 5 (April 2023) downriver measurements. Right-hand column: Differences from the near-surface value (taken from the highest measurement in water column) of (b) pH, (d) chlorophyll, (f) fDOM, and (h) dissolved oxygen.

4.2.6 *Summary of field measurements*

Summaries of the salinity measurements are shown in Figure 4.44 (selected salinity profiles from points along the Waihou river) and Table 4.1 (salinity intrusion length for each survey).

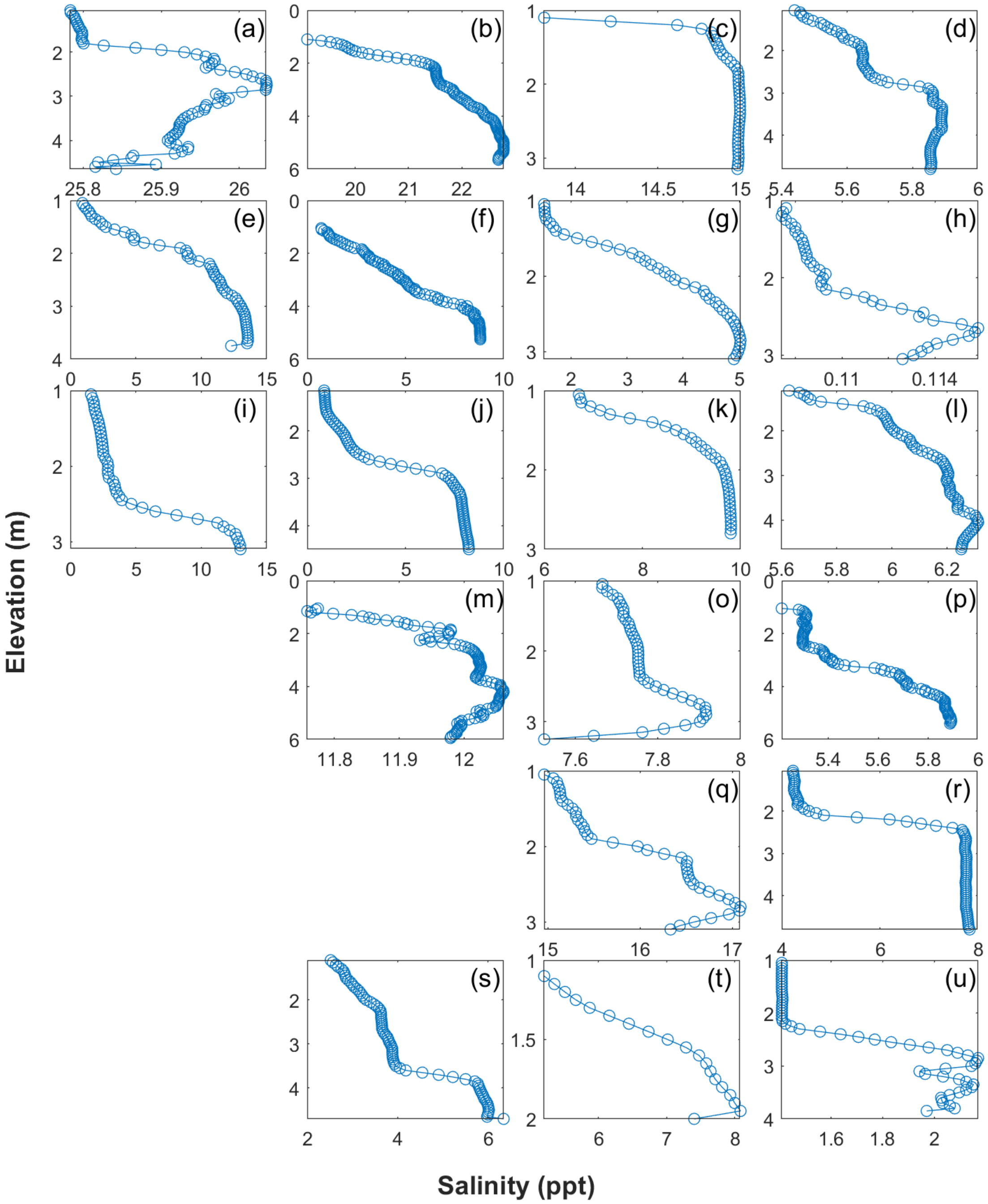

Figure 4.44: Summary figure of salinity profiles from the field surveys. Columns left to right show profiles taken corresponding to distances of 2,000 m (a, e, i), 4,000 m, 6,000 m, 8,000 m. Rows correspond to surveys 1 to 5 (top to bottom: September, December, January, March, April upstream, April downstream), with survey being split into upriver and downriver sections (rows 5 and 6).

Table 4.1 Summary table of salinity results from the field data, including approximate values of how far the salinity intruded upriver, river flow at time of surveys and high tide times (NZ local time) and value.

		How far salinity reached upriver from the mouth (km)						High tide	
Survey	**Day**	**20 PSU**	**10 PSU**	**5 PSU**	**1 PSU**	**0.1 PSU**	**River flow ($m^3.s^{-1}$)**	**Time**	**Value**
1	September (2022)	4.7	7.4	8.5			40	13:47	2.95m
2	December (2022)		4.5	6.1	7.2	7.7	80-85	16:07	3.08m
3	January (2023)		7.3	8.8	11.8	12.5	40-41	16:28	3.12m
4	March (2023)		5.3	8.7	9.8		34	12:00	3.24m
5	April (2023)		7.5	8.9	9.75-10		32-33	12:17	2.86m

4.3 Numerical modelling results

In this section, we present results of the numerical modelling. Initially, we report differences between results obtained with the two- and three-dimensional model simulations. These initial tests were undertaken with the model predictions from the period the model was originally calibrated for (April 2015). Then an example of model results is presented from the simulations corresponding to one of the field surveys. These are followed by a summary section which compares results for the 5 surveys and the field data. Lastly, we present a short sensitivity analysis examining how results change with the use of different model parameters.

4.3.1 2D vs 3D Modelling

Time series of model spin-up are shown in Figure 4.45 for both 2D and 3D model simulations (simulations 1 and 2, Table 3.2). There is no difference in salinity between the two models for the Tararu tide observation point (close to the river mouth) for both the surface (layer 1) and bottom layers (layer 10). However, the difference between model salinities increases with distances upriver: small differences (less than 0.5 PSU) are predicted at the Kopu Bridge observation point, and differences of approximately 2 PSU are seen the Turua observation point (~8.7 km upstream of the river mouth). In each case, the 3D model predicts higher salinities than the 2D model, with a slight stable stratification (~0.03 PSU difference between surface and bottom layers).

Figure 4.46 is a snapshot showing the maximum extent of the salt intrusion for one incoming flood tide. In this case, the extent of the salt intrusion was smaller in the 2D model than in the 3D model (likely owing to enhanced mixing in the vertical in the 2D model). The difference in salinity extent was 0.8 km.

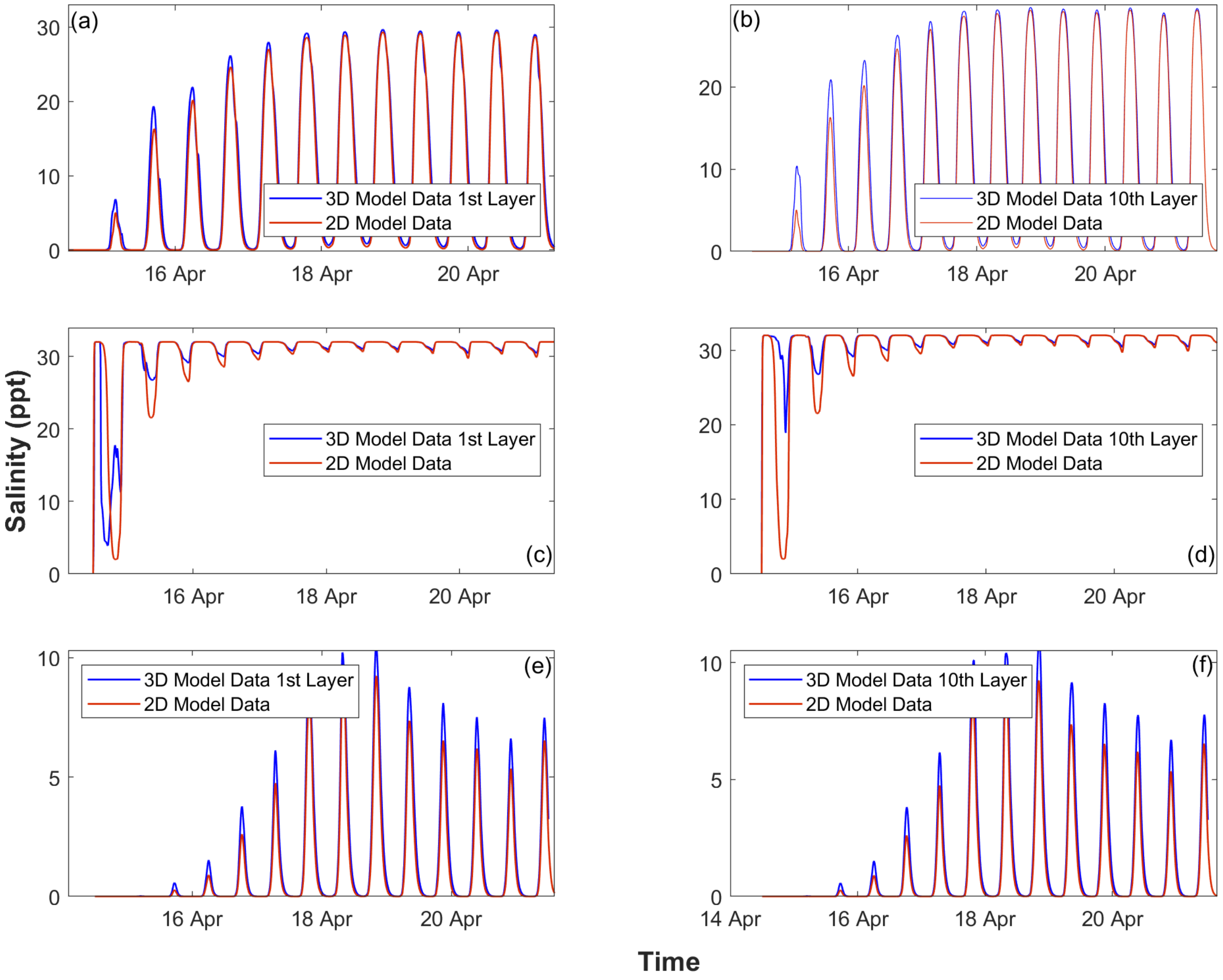

Figure 4.45: Salinity against time differences between 2D modelling and 3D modelling for three observation stations Kopu Bridge (a, b), Tararu Tide (c, d), and Turua (e, f).

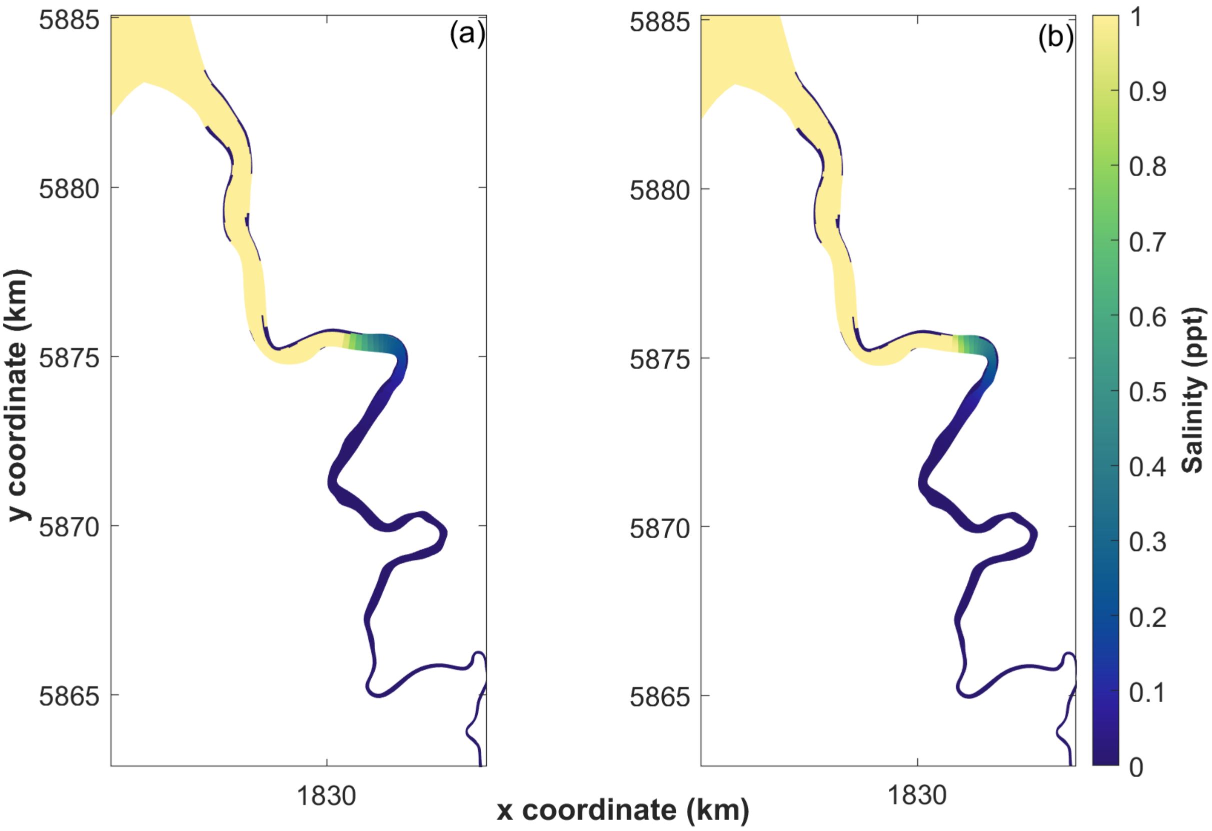

Figure 4.46: Difference of salinity intrusion between 2D modelling (a) and 3D modelling bottom layer (b). For the same time at 19th of April 2015

4.3.2 *Model predictions – for survey 1*

In this section, we present a few figures to show the general circulation patterns from the model run 3 (Table 3.2), the 3D simulation corresponding to the same time period as field survey 1 (with results from after the initial model spin-up period).

Figure 4.47 shows the predicted water depths at different observation points, plotted against time. Tidal heights at the river mouth (OP0) are approximately 2 m. As expected, tidal influence decreases with distance upriver: for example, Puke Bridge shows tidal height differences of about 1 m, while at the Up-estuary observation point (near Te Aroha), there is no tidal influence. The tide at Kopu and Turua is flood-dominant, while the other locations exhibit more symmetric tides.

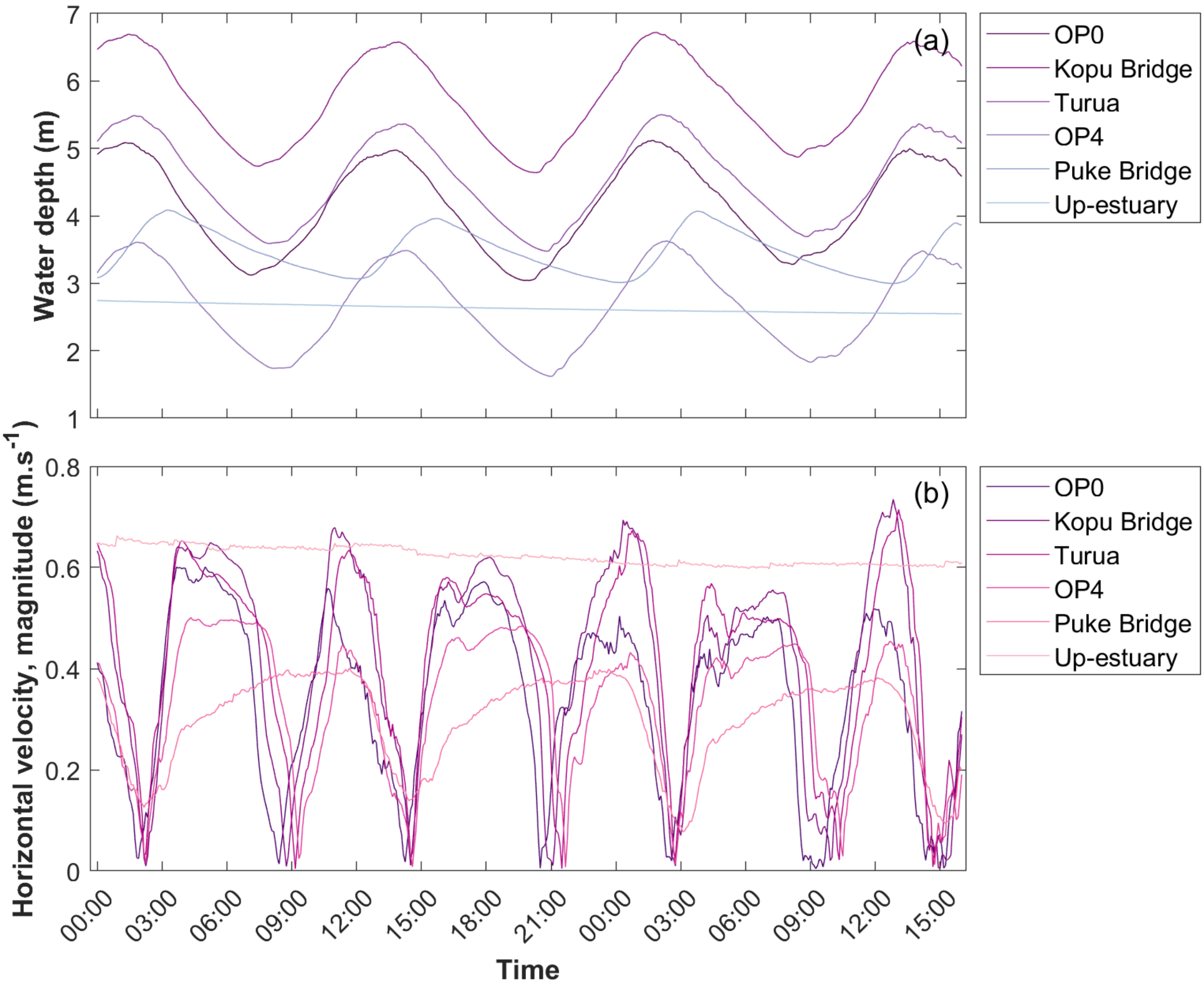

Figure 4.47: Time series of water depths (a), and depth averaged velocity (b) at different observation points from model simulation 3 of the time period of survey 1. Coloured lines depict different locations (Figure 3.3) with lighter lines corresponding to locations which are further upriver (times in UTC).

Figure 4.48 and Figure 4.49 show snapshots of horizontal flow speeds and salinities, respectively, for both surface and bottom layers, at the times of salinity maximum extent, and peak ebb and flood tides (i.e. maximum horizontal velocity during flood and ebb tide). The time of minimum horizontal velocity aligned with the time of salinity maximum extent, around 02:54 UTC (26 hours after model start, Figure 4.47), and velocities within the river were around 0.1-0.5 m.s^{-1}. Maximum horizontal flow speeds of 1 and 0.83 m.s^{-1} during flood and ebb tides occurred approximately 2 hours before and after the time of maximum salinity extent. As anticipated, faster slow speeds occurred at the surface, and flows were flood dominant throughout the domain. For the times shown in the figure the salinity intrusion extended further upriver in the bottom layer than the surface layer (Figure 4.49).

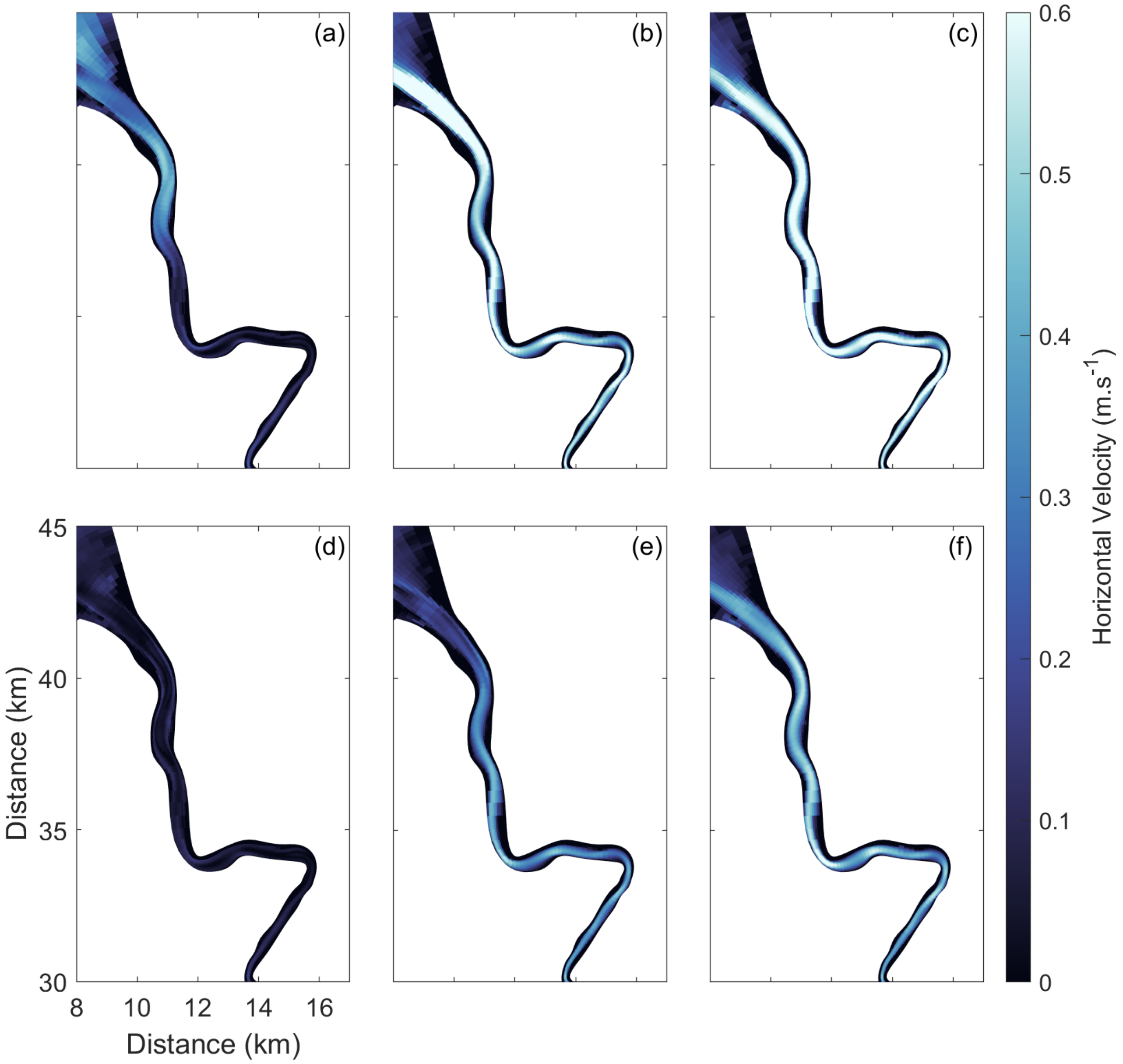

Figure 4.48: Model predictions of horizontal flow speeds at the surface (a, b, c) and bottom (d, e, f) for model run 3 (corresponding to field survey 1). Columns correspond to (a, d) the time of horizontal velocity maximum salinity extent (14:54), (b, e) peak ebb tide (16:54), and (c, f) peak flood tide (12:54) (times are NZ local time).

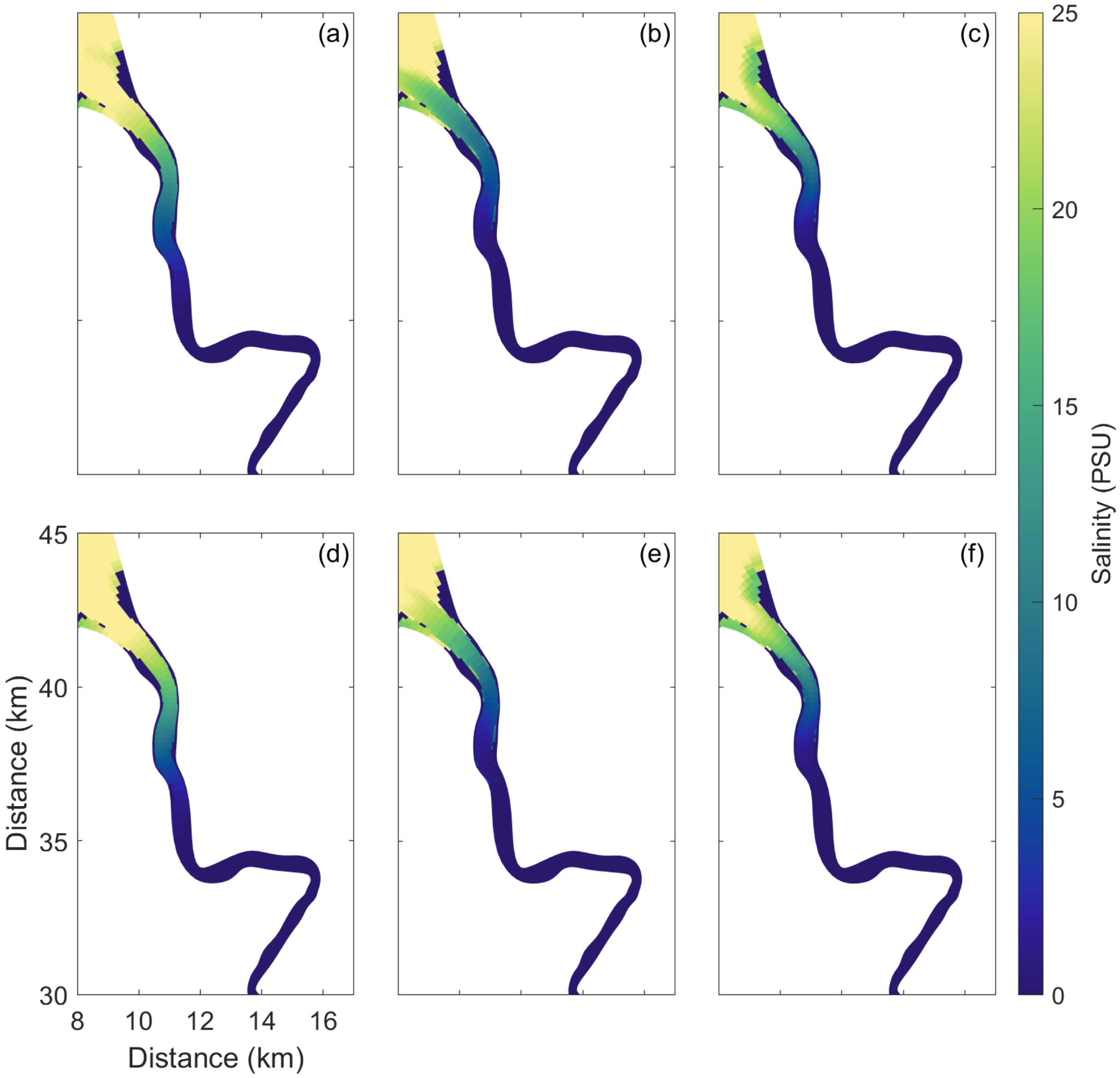

Figure 4.49: Model predictions or salinity intrusion at the surface (a, b, c) and bottom (d, e, f) for model run 3 (corresponding to field survey 1). Columns correspond 10 (a, d) the time of maximum salinity extent (14:54), (b, e) peak ebb tide (16:54), and (c, f) peak flood tide (12:54) (times are NZ local time).

4.3.3 Comparison with field data

We compare profiles of model salinities predicted by the model with the field data (Figure 4.44). Figure 4.50 shows model salinity profiles from the same location and time as profiles from casts taken in the field surveys, and Figure 4.51 shows model salinity profiles from the time of model maximum salinity extent, these profiles do not match with the field time and location. Model predictions show that the water column was typically well-mixed (Figures 4.50, and 4.51); haloclines shown in profiles were very slight, with a difference of around 2 PSU salinity from the surface to the bed, portraying a well-mixed water column. The salinity difference between surface and near bed is 0.01-0.1, with higher salinity near the surface than the bed for all plots in Figure 4.50 except plots s, t, and u which show profiles taken on the ebb tide. The field data has a difference of surface to near-bed of 0.2-15, with an average of 4 PSU difference. Compared to the field data profiles (Figure 4.44), the difference in salinity values between the model and the field varies from 1 to 15 PSU, with an average of around 7 PSU.

In Figure 4.51 (time of maximum salinity extent), salinity difference between surface and near bed is 0.001-2, with higher salinity near the bed than the surface The profiles in Figure 4.51 are closer to the field data than Figure 4.50 (profiles from same time as the surveys), which shows that the horizontal velocity of the salinity intrusion into the estuary is slower in the model than in the field.

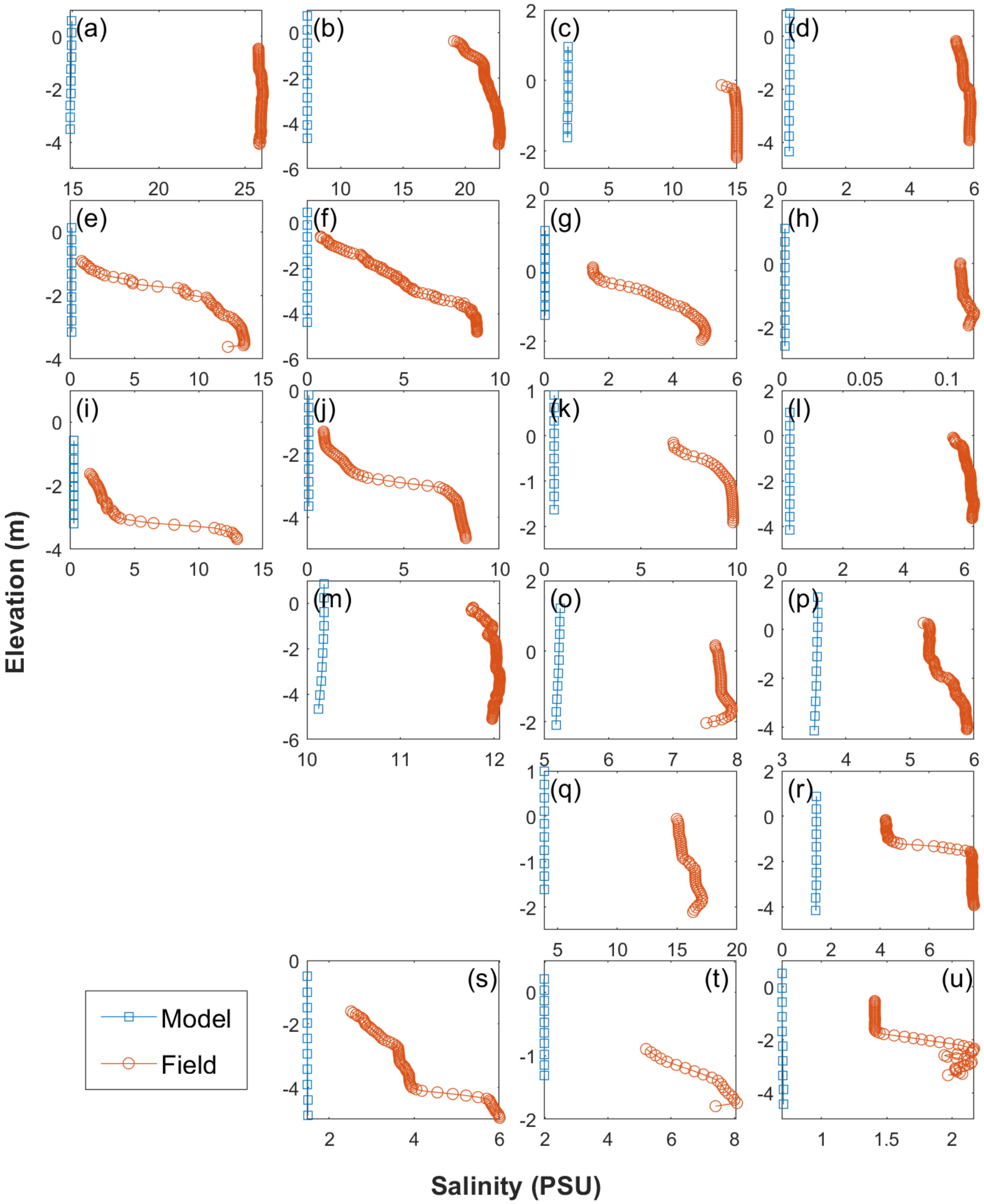

Figure 4.50: Salinity profiles for the original September model run (model 3) and survey 1, taken from the corresponding field data location and time. Columns left to right show profiles corresponding to distances of 2,000 m (a, e, i), 4,000 m (b, f, j, m, s), 6,000 m (c, g, k, o, q, t), 8,000 m (d, h, l, p, r, u). Rows correspond to surveys 1 to 5 (top to bottom: September, December, January, March, April upstream, April downstream) with survey 5 being split into upriver and downriver sections (rows 5 and 6).

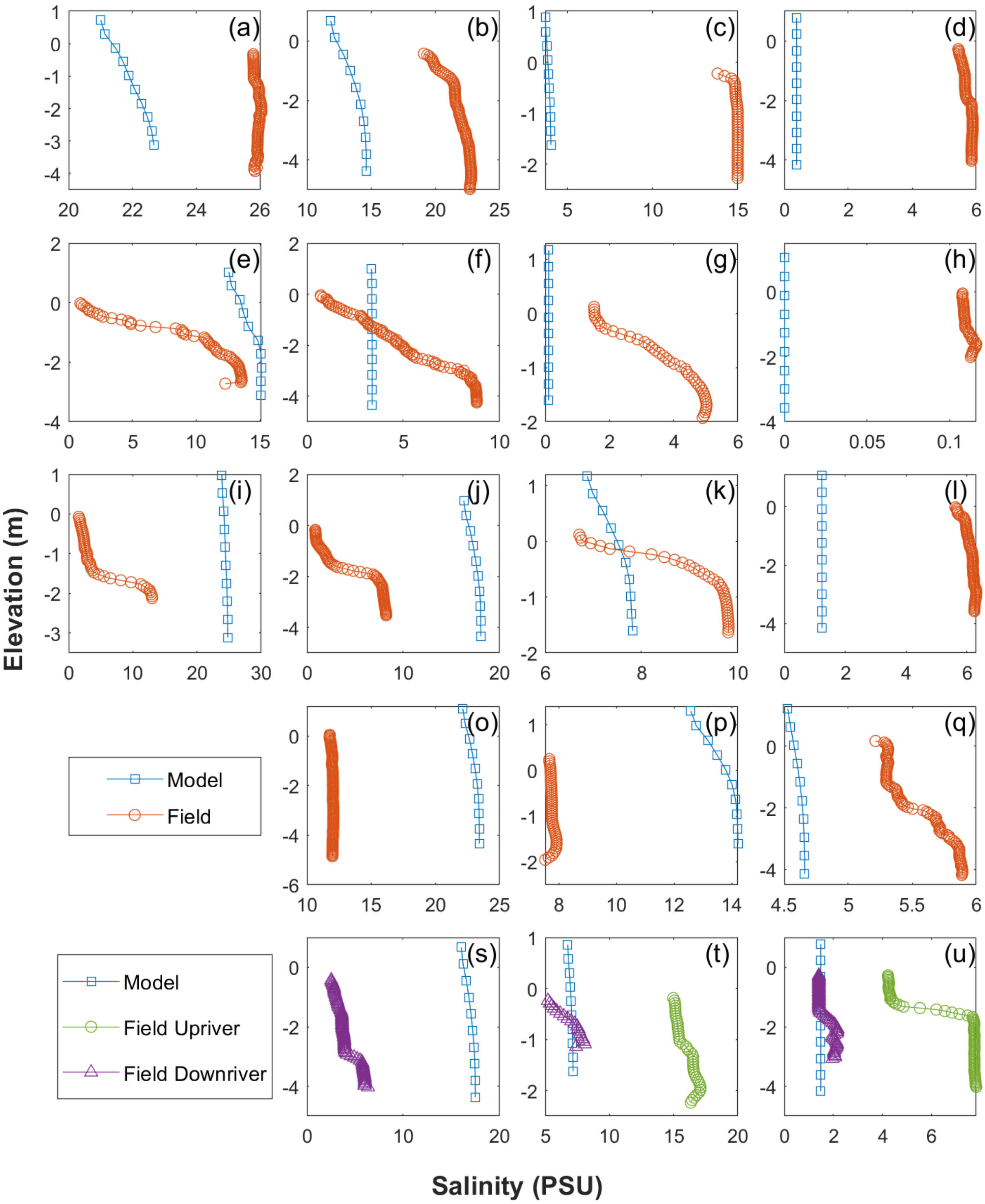

Figure 4.51: Salinity profiles for the original September model run (model 3) and survey 1, from the time of maximum salinity extent (14:54), not corresponding with field data time and location. Columns left to right show profiles corresponding to distances of: 2,000 m (a, e, i), 4,000 m (b, f, j, m, s), 6,000 m (c, g, k, o, q, t), 8,000 m (d, h, l, p, r, u). Rows correspond to surveys 1 to 5 (top to bottom: September, December, January, March, April upstream, April downstream) with survey 5 being split into upriver and downriver sections (rows 5 and 6).

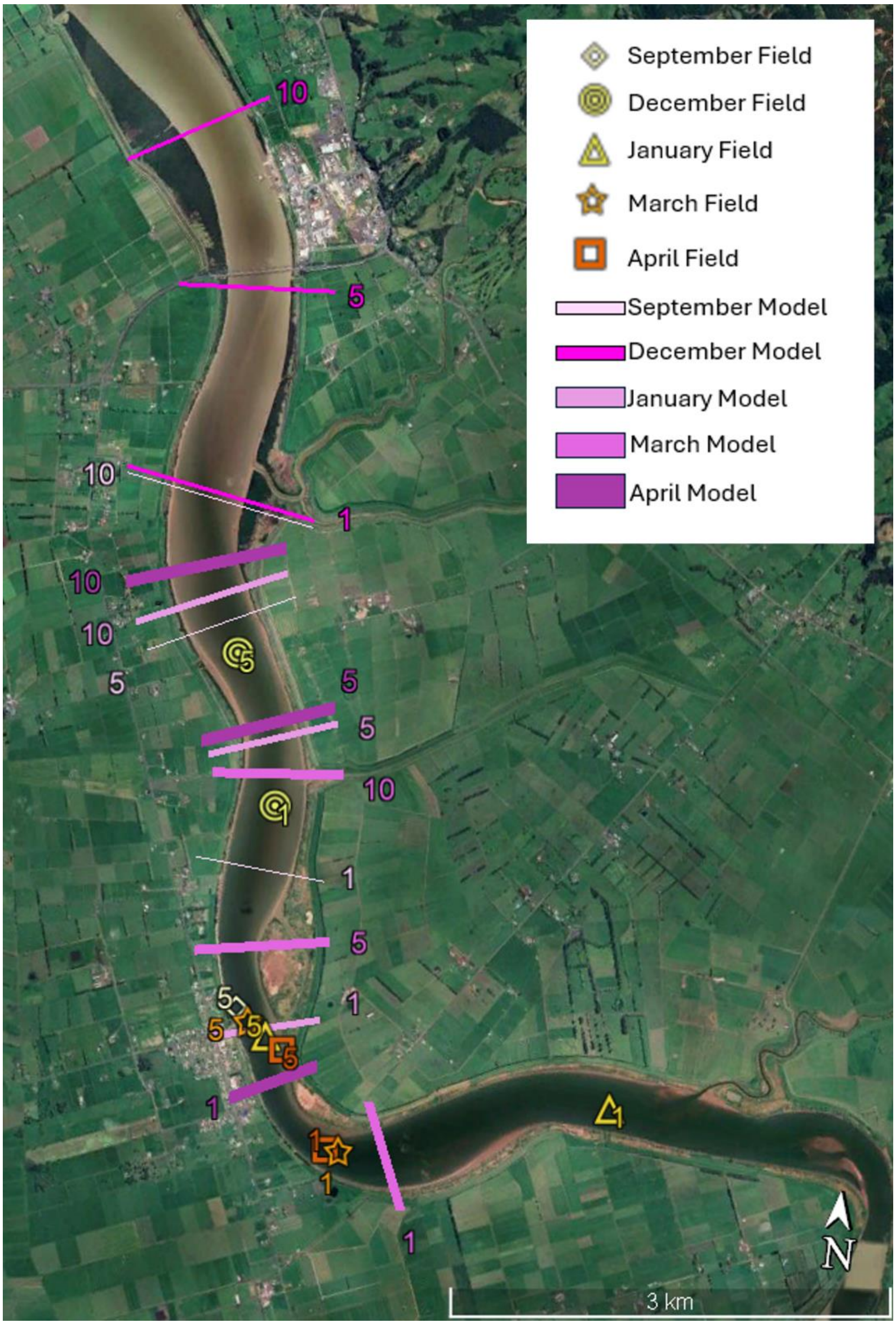

Figure 4.52: Salinity intrusion 10 PSU, 5 PSU, and 1 PSU maximum extents from the original 3D model runs, and points of salinity intrusion from the field surveys 5 PSU and 1 PSU maximum extents.

Figure 4.52 shows a summary of the extent of salinity intrusion calculated by the model and points of salinity intrusion from the field surveys. In general, it appears that the 3D model underpredicted salinity values and the distance of maximum salinity intrusion.

For the survey 1 (September) model run, 10 PSU reached 5.1 km upstream, 5 PSU reached 5.9 km, which is 2.5 km shorter than the field measurements, and 1 PSU reached 7.7 km upstream from the mouth of the river. For the December model run, 10 PSU reached 2.46 km upstream, 5 PSU reached 3.6 km, 1 PSU reached 5.1km upstream from the mouth of the river. There is a 2.1 km difference between the field measurement and the model results for 1 PSU. For the January model run, 10 PSU reached 5.8 km upstream, 5 PSU reached 6.8 km, 1 PSU reached 8.8 km upstream. There was a 3 km difference between the field measurement and the model data for 1 PSU. For the March model run, 10 PSU reached 7.0 km upstream, 5 PSU reached 8.2 km, 1 PSU reached 10.2 km upstream. 5 PSU and 1 PSU are very similar between the field measurement and model results, however, there is a 1.5 km difference between the field measurement and model results for 10 PSU with the model being further upstream than the field measurement. For the April model run, 10 PSU reached 5.5 km upstream, 5 PSU reached 6.7 km, 1 PSU reached 9.2 km upstream. There was a 2.2 km difference between the field measurement and the model data for 5 PSU and a 0.6 km difference for 1 PSU.

Table 4.2 Summary table of the approximate Delft 3D numerical modelling results, depicting how far the salinity intruded upriver as calculated by the model, compared to approximate salinity intrusion distances from the surveys.

Day	**Model 20 PSU**	**Field 20 PSU**	**Model 10 PSU**	**Field 10 PSU**	**Model 5 PSU**	**Field 5 PSU**	**Model 1 PSU**	**Field 1 PSU**	**Model 0.1 PSU**	**Field 0.1 PSU**
September (km)	2.4	4.7	5.1	7.4	5.9	8.5	7.7		9.5	
December (km)			2.4	4.53	3.6	6.19	5.1	7.2	6.3	7.7
January (km)			5.8	7.3	6.8	8.8	8.8	11.8	10.3	12.5
March (km)			7.0	5.3	8.2	8.7	10.2	9.8	12.2	
April (km)			5.5	7.5	6.7	8.9	9.2	9.75-10	11.1	

4.3.4 Adjusted parameter results

For the following model run results, the Horizontal Eddy Viscosity and Diffusivity were changed for each model run with the aim of improving model predictions, relative to the field data. Table 3.2 sets out the changed parameters for the following model runs.

Model 8 (Table 3.2) had very little difference compared to the original model (model 3), except salinity intruded less by 0.86 km. Model 9 salinity intrusion penetrated 0.5-1 km further upstream compared to the original run, and profiles had slightly more exaggerated haloclines. Model 10 salinity intrusion was slightly less than model 9 with 0.3-0.5 km difference compared to the original model. Lastly model 11 salinity intrusion was greater than the other models, with 0.7-2.7 km difference from the original run, and the profiles had similar haloclines to the model 9 results.

Ultimately the horizontal eddy diffusivity was found to exert the largest influence on the characteristics and distance of the salinity intrusion. Figures 4.53 and 4.54 show the final model 11 results, with a decreased horizontal eddy diffusivity of 0.1 $m^2\ s^{-1}$, which had the best model performance.

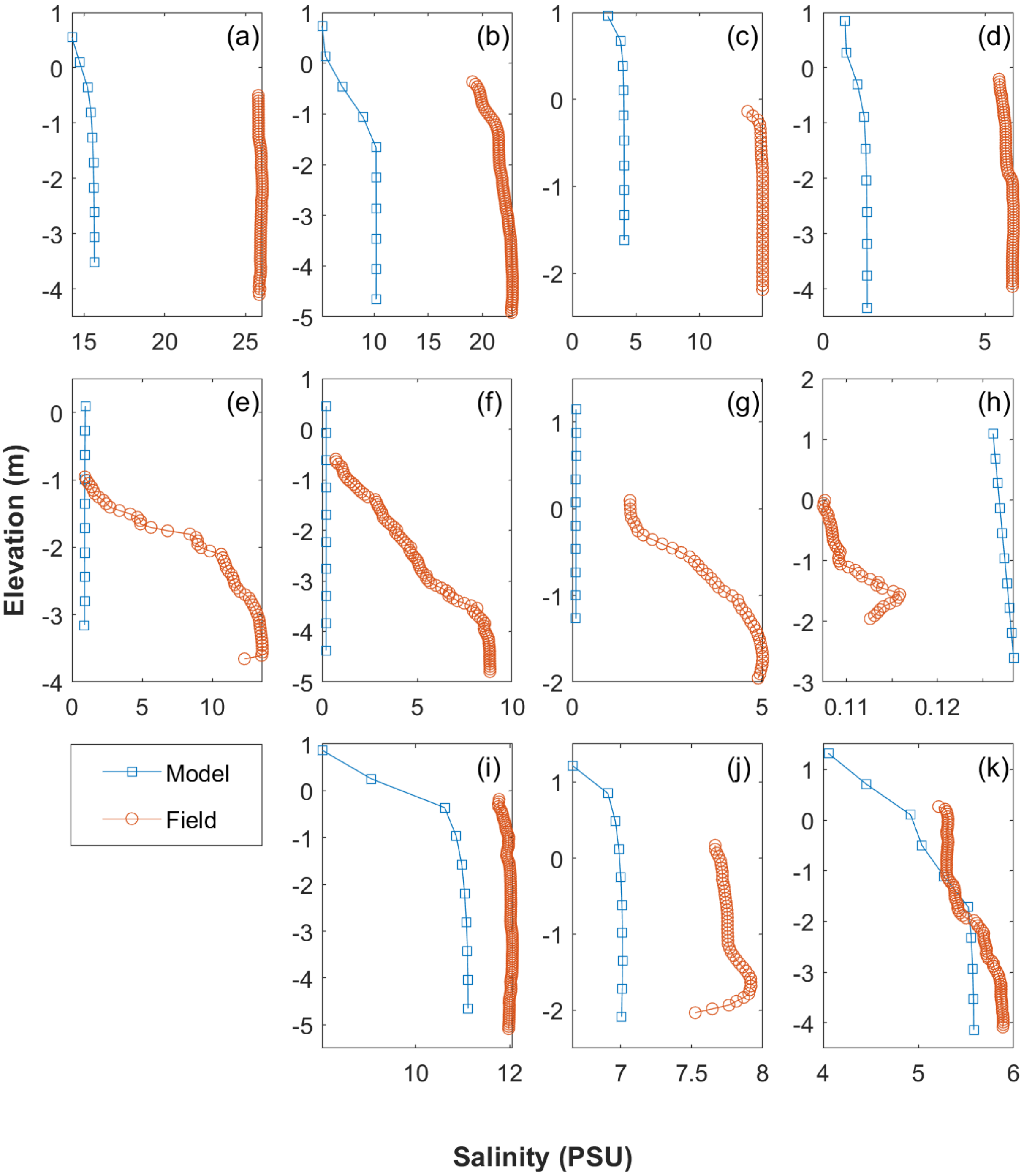

Figure 4.53: Salinity profiles from the adjusted model results (models 11, 12, 13) and survey 1, corresponding with the same time and location as the field data. Columns left to right show profiles corresponding to distances of: 2,000 m (a, e), 4,000 m (b, f, i), 6,000 m (c, g, j), 8,000 m (d, h, k). Rows correspond to surveys 1, 2, and 4 (top to bottom: September, December, March).

Although there is much improvement compared to the original model runs, the salinity intrusion still falls short to that observed in the field surveys. There is a 4-15 PSU difference between the September model and the field data, 2-13 PSU difference between the December model and field data, and 1-5 PSU difference between the March model and field data.

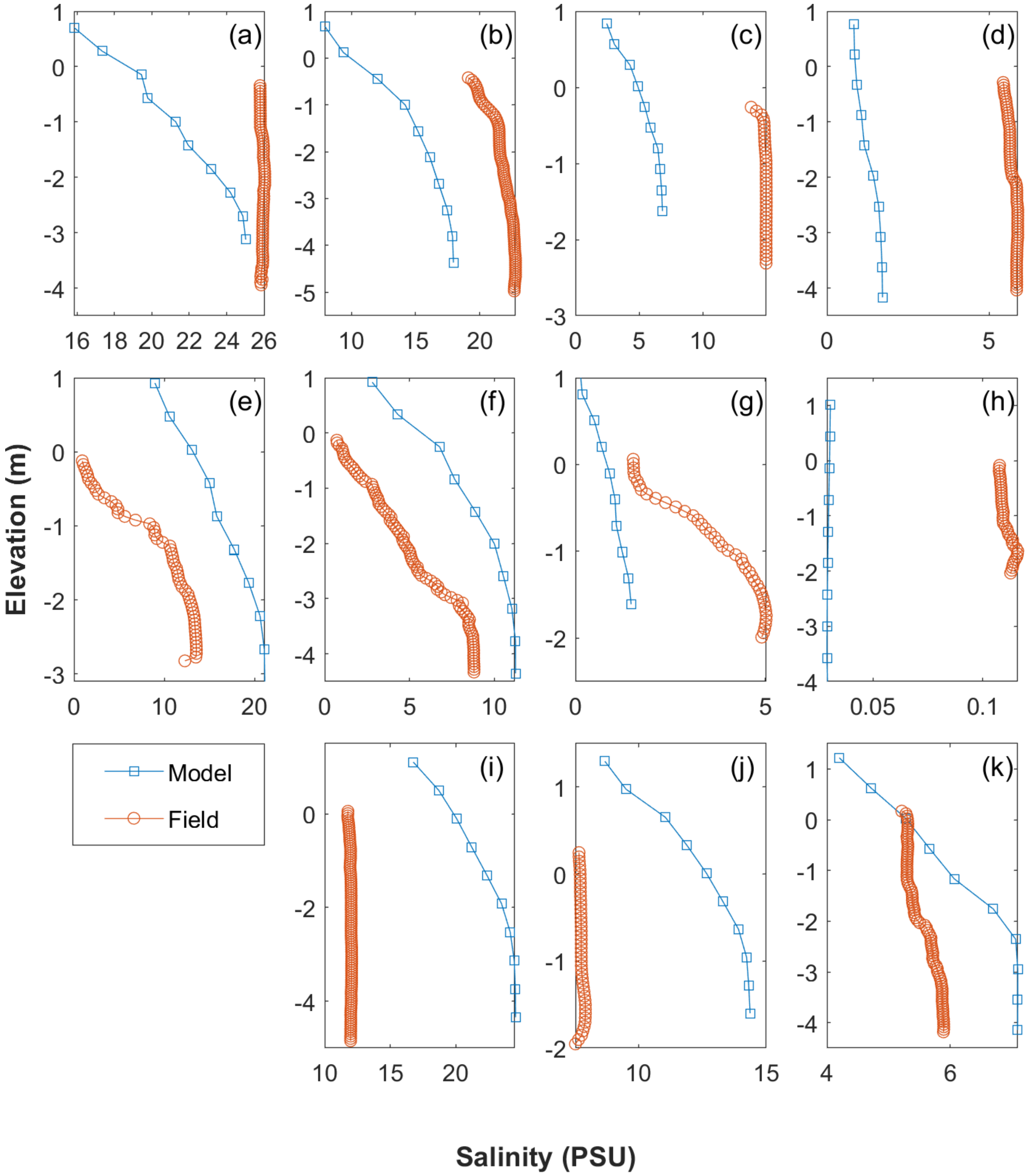

Figure 4.54: Salinity profiles from the adjusted model results (models 11, 12, 13) and survey 1, from the time of maximum salinity extent, not corresponding with the time and location of the field data. Columns left to right show profiles corresponding to distances of: 2,000 m (a, e), 4,000 m (b, f, i), 6,000 m (c, g, j), 8,000 m (d, h, k). Rows correspond to surveys 1, 2, and 4 (top to bottom: September, December, March).

The salinities in the profiles in Figure 4.54 (at maximum extent) are closer to the observed (Figure 4.44), than in Figure 4.53 (taken at the same times). The haloclines in the model data also show closer resemblance to the field data. This result indicates that the there is a lag time between the model and field data, owing to the slower speeds of the intrusion in the model than in the field.

Summary figures can be found in the appendix (Figures A.3 and A.4) which show salinity profiles of each adjusted parameter model run, Table 4.3 shows a summary of the results.

Table 4.3 Summary of results from the changed parameter Delft 3D model runs compared to the original model run and the field results. Table shows approximate distance of salinity intrusion upriver from the mouth.

	How far salinity reached upstream from the mouth of the river				
Model run	**20 PSU**	**10 PSU**	**5 PSU**	**1 PSU**	**0.1 PSU**
Sep Field	4.8	7.4	8.5		
Sept19_03	2.4	5.2	5.9	7.8	9.5
Sept19_04	2.4	5.1	5.9	7	9.2
Sept19-05	3.6	5.7	6.6	8.4	10.6
Sept19_06	3.1	5.3	6.5	8.8	10.7
Sept19_08	3.2	6.3	6.9	9.4	12.4
Mar Field		5.4	8.7	9.8	
Mar13_03	4.9	7	8.2	10.2	12.2
Mar13_04	5.1	7.3	8.9	11.1	13.3
Dec Field		4.5	6.2	7.3	7.8
Dec19_03		2.5	3.6	5.1	6.5
Dec19_04	2.1	4.5	5.6	6.7	8

Chapter 5: Discussion

5.1 Structure of salinity intrusions within the Waihou River

Measurements across different days revealed that the salinity structure of the Waihou River estuary was in the form of a mixed estuary for four out of five field surveys (September, January, March, and April). This similarity between the salinity structure between surveys is perhaps unsurprising given tidal conditions and river flows were relatively similar (see Table 4.1), with relatively small ratios of river to tidal volume. However, for the second survey (December), measurements showed that towards the seaward end of the estuary, a salt wedge shape with a strong halocline was present. When the salt wedge was present, the salinity intrusion penetrated less far landwards up the river than in cases when the river was mixed. This change in distance of penetration and change in mixing of the estuary, is likely predominately owing to the differences in river discharge rather than differences in tides. The December field visit had substantially a higher river flow of 83.8 m^3 s^{-1} recorded in Te Aroha compared to other field visits where the Waihou River had a flow of 32-41.2 m^3 s^{-1} recorded in Te Aroha. According to Krvavica et al. (2021), a strong river flow into an estuary is able to hold a forcing gradient against tidal mixing and wind induced turbulence, allowing there to be a steady pycnocline and salt wedge shape, compared to low river flows which don’t have enough force against the tidal currents to prevent vertical and horizontal mixing (Geyer & Farmer, 1989; Krvavica et al., 2021). The lower river flow on the other four surveys allows there to be increased shear, turbulence, and therefore, vertical mixing (Krvavica et al., 2021). The shape of an estuary can also influence mixing of the water types. In this case, as the estuary is a category B, a salt wedge patterns would be expected regularly if the estuary/river were deep enough (Hume et al., 2007); however, since the river is not that deep (1-7m, deepest at 9m in one location), a salt wedge only occurs intermittently.

In their study, McBride et al. (2016) concluded that the primary control on the distance of salt intrusion was sea level. However, given the difference between spring and neap tides, our results suggest that river flow may actually be the primary driver affecting the intrusion length of the salt water. During survey 2, the river flow was considerably larger than the river flow during surveys 1, 3, 4, and 5, which all had very similar flow rates. The salinity front during survey 2 intruded considerably less far upriver compared to all other surveys. The tide appeared to thus be a secondary control on the salinity intrusion, as surveys 1 and 3 had similar river flows but survey 1 was during a neap tide and the salinity intrusion was less compared to survey 3. Surveys 4 and 5 had very similar river flows and tidal flows, and the salinity intrusion length was very similar.

5.2 Turbidity within the Waihou River

In general, the measurements show a reduction in suspended sediment concentration with distance upriver (e.g. Figure 4.23 and 4.31a). Moreover, repeated casts from the same locations during flood tide also show a gradual increase in SSC (Figure 4.24 panels a to f), and similarly repeated casts in the same location during ebb tide in general show an increase in SSC (Figure 4.41) possibly due to the ETM receding past the measurement point. These patterns suggest that in the lower reaches of the river, the sediment is predominantly supplied from the Firth of Thames, rather than being transported down river.

Winds drive clockwise and anti-clockwise residual circulation in the southern end of the FOT which historically trapped river-borne fine sediments (rhyolitic glass that transforms to smectite-rich muds after it is deposited) within the tidal flats and river delta (Swales et al., 2015), and in the mangrove forests which line the river mouth (Vundavilli et al., 2021). These sediments are then resuspended by incoming tidal currents, and waves (and at the forest fringe region, by turbulence within the mangrove pneumatophores, e.g. Norris et al., 2019, 2021) and advected upriver by tidal currents. Local resuspension of bed sediments may also contribute.

The import of sediments from seaward to landward regions is also supported by the measurements showing larger SSC at the bottom of the water column. This vertical gradient is also expected to be enhanced by gravity acting on sediments and causing settling through the water column. Within the salt intrusion at the bottom of the water column, several opposing processes may be occurring. Salinity and turbulence can encourage flocculation of fine grained suspended particulate matter (chemically and physically), and these flocs will settle more rapidly than single particles. However, we observe greater turbidity within the salinity intrusion than in the freshwater further upstream, which likely reflects either the presence of sufficient shear instability to drive break-up of flocs or sufficient vertical mixing within the lower water column to retain even larger flocs in suspension (as observed by Dejeans, 2023). Such an import of sediments into the river driven by exchange flow, tidal processes and local resuspension has also been observed during low-flow conditions in bigger rivers such as the Mekong (Nowacki et al. 2015).

The tidal pumping and residual gravitational circulation transporting the sediments upriver forms an estuarine turbidity maximum (ETM) (Manning et al., 2010), which is found in the lower estuary. The lower estuary ETM is possibly controlled by the salt intrusion limit during low tide rather than high tide. Our results show that the highest turbidity was recorded between 0-7 km upstream from the mouth of the river, which match with time series measurements from Roche (2022), who found that turbidity was highest up to ~6.5-7 km upstream. These locations for the ETM are at a smaller distance upstream than those reported that Vant, (2011), who found the ETM 10-20 km upstream from the mouth of the river. The difference in location of the ETM between former and the present survey may be attributed to changing sediment loads and distribution within the catchment over time, or perhaps differences in river flows (owing to, for example, flood control works). Of note is suspended sediment concentrations reached maximum values of ~7,000 mg.L^{-1} (Figure 4.40) and ~9,000 mg.L^{-1} (Figure 4.17) near the bed, implying the existence of fluid mud.

Measurements from a moving platform such as the ones presented in this thesis provide new information which cannot be captured by Eulerian (fixed point) data; for example, in general the data offer better spatial resolution which allows for resolution of variability over smaller length-scales. Moreover, the use of profiling instruments allows for measurement of (close to) the full water column. However, it is worth noting that data which change in both and space and time (yet are not truly flow-following), adds significant complexity to both data processing and the interpretation of results. A better approach would be to combine both time-series measurements at fixed points with boat-mounted profile measurements; however, such an experiment would likely be expensive and logistically challenging in the energetic riverine environment. Additionally, co-located measurements of velocity and suspended sediments would be required to more carefully identity controls on the transport of sediments and to obtain robust estimates of advective fluxes.

The characteristics and distance of the salt intrusion are also correlated with other water quality variables. Profiles show that pH also tended to decrease with fresh water/distance upstream (7.2-7.6 in fresh compared to 7.25-8.2 within salinity intrusion) (Figure 4.13, 4.33 and 4.42) during upriver measurements. Chlorophyll measurements were observed to be higher within the salinity intrusion, while the fDOM measurements were lower within the salinity intrusion (Figure 4.13, 4.19, 4.25, 4.33 and 4.42).

5.3 Assessment of model performance

In general, when run with default parameters (model simulations 3-7, a horizontal eddy viscosity of 1 m^2.s^{-1}, and a horizontal eddy diffusivity of 10 m^2.s^{-1}), the numerical model did not perform well in terms of predictions of the length of the salt intrusion upriver. For all surveys except for survey 4, the model underpredicted the length of the intrusion by around 0.8-3 km, while for survey 4, the model overpredicted by 0.4 km. We note also that the while the model intrusion lengths for specified isohaline levels can be determined with relatively high accuracy (to within one timestep), the field observations only provide a lower bound for the distances as the sampling continued to move upstream. Thus, the discrepancy between model and field data provided is a minimum. Our results contrast to previous 3D hydrodynamic modelling of the system reported in Schueder et al. 2017, in which salinity intrusions lengths were overpredicted, which they attributed to inaccuracies in the forcing by river discharge. In our case, the model was forced with measured water levels (from Te Aroha and Tararu, FOT) and there are only relatively small stream inputs below this location, so it is likely that the upstream boundary condition is not a primary contributor to the discrepancy. Several other physical processes were neglected within the model, such as wind forcing and waves were not included. These processes could potentially affect mixing dynamics in particular at the river mouth. While temperature variations were neglected, field data indicates that the marine water was warmer than the freshwater during the observational period. However, vertical temperature differences throughout the system were small, therefore any temperature and buoyancy-driven component of mixing would also be small.

The model also exhibited deficiencies in predictions of the salinity stratification. In most cases, model predictions showed a well-mixed estuary, or partially mixed estuary with only a slight halocline. Thus, we conclude the model was over-mixing and therefore salt intrusion lengths were under-predicted. Indeed, model performance improved with horizontal eddy diffusivities changed from 10 to 0.1 $m^2.s^{-1}$. In these cases, the profiles had a much more exaggerated halocline than the original model run, and predictions of salt intrusion length were closer to observed (for the simulation of survey 1, the salt intrusion length was 6.9 km for 5 PSU, a 1 km increase from the original model run). The model also applied a free-slip bottom boundary condition – which reduces mixing at the sea/river floor. Given the majority of the river-bed is soft mud (Roche, 2022), this assumption is likely reasonable (moreover, changing to a non-slip boundary condition would further enhance mixing).

Delft3D uses a Reynolds-Averaged Navier- Stokes (RANS) based approach, which has been shown in past work to exhibit deficiencies in performance in predicting flows in rivers, particularly secondary flows in the regions of bends (Dejeans et al., 2022). However, such previous models show underprediction of turbulence in these regions of high curvature, so these deficiencies are therefore likely not responsible for the over-mixing.

Inability of the model to accurately depict the dynamics of salt intrusion into the Waihou River estuary may have negative consequences for the management of the river. While predictions of effects of climate change may therefore provide an indication of trends, predictions of the magnitudes of changes should be interpreted with caution. Further sensitivity analysis and model improvement should be undertaken to allow for robust predictions and development of strategies to mitigate hazards of climate change, such as intrusion of salinity into near-by aquifers, predicting water quality changes due to sediment and nutrient transport. Salinity intruding further upstream could have consequences on communities that have coastal aquifers, as saltwater lateral intrusion may occur, polluting the aquifers, making them undrinkable and unusable (Barlow & Reichard, 2009; McBride et al., 2016). A drier climate could reduce precipitation events and therefore reduce the river flow. This reduction in turn may cause salt water to intrude further upstream, altering ecology and sediment and therefore bathymetry and morphology of the river (Gugliotta et al., 2017). A lower river flow may also cause the estuary to become mixed rather than having a salt wedge during high tide (McKeon et al., 2020). Alternatively, there may be more significant rainfall events due to change in climate which could cause flash flooding and high river flows. During these events, a salt wedge may be present and possibly intrude less far upstream than during low flows (McKeon et al., 2020).

5.4 Comparison with other systems

Here, we provide a few comparisons with studies of other river systems to set the present results into context of rivers of different sizes globally. Tanshui river system, in Taiwan, is 327.6 km long and has a catchment area of 2,726 km^2. A study was undertaken to identify the influence of river discharge on the salinity intrusion in the estuary through 2D modelling, validated by observed timeseries (Liu et al., 2001). Their results demonstrated that the Tanshui estuary is predominantly partially mixed, but well-mixed at hightide and stratified at low tide, and that the salinity is very sensitive to river discharge. The salt intrusion limit was defined as a 1 PSU isohaline. The study found that significant stratification was found up to 10 km upstream, as the downstream end of the river is the deepest. Higher river flow pushed the salinity intrusion further downstream than weak river flow. The study found that there is a balance between tidal mixing and baroclinic circulation, and this balance determines the salinity structures (Liu et al., 2001). These results are somewhat similar to the results obtained in this thesis. It was found that river discharge plays an important role in the vertical structure of the salinity and salt intrusion length.

James and Chickahominy (CHK) rivers feed into Chesapeake Bay, USA. A study was conducted on these rivers, focusing on the effects of climate change and sea level rise on saltwater intrusion up the rivers through 3D hydrodynamic modelling, validated by observed water quality measurements from Chesapeake Bay. Through their research, they found that several studies indicated that sea level rise increases saltwater intrusion, resulting in changes to stratification and estuarine circulation (Rice et al., 2012). The James River is 560 km long, the lower reaches are up to 15 m deep, and salinity found near the river mouth is 25 PSU. The CHK river is a tributary of the James River entering at 75 km upstream of James' River's mouth. The CHK river is 140 km long. When James River's has a low flow salinity of 7 PSU can intrude into the CHK River. Their results showed that, for the James River, salinity increases as the sea level rises, and that when there is a low flow, salinity increases further than when the river has average flow. 50 cm sea level rise by 2100 has an increase of 8 km upstream (dry year) and 3 km upstream (typical year). There is also a change in vertical salinity structures with sea-level rise, as the 10 PSU isohaline moved significantly more upstream compared to the distance that 5 and 20 PSU moved (Rice et al., 2012). For the CHK river, salinity also increases with sea-level rise, with greater effect during dry/low flow years. A 50 cm sea-level increase by 2100 would cause 5 PSU to reach 23 km upstream (dry year), and 14 km upstream (typical year) from the mouth of the river (Rice et al., 2012). These findings are consistent with my observations, that river discharge had such a large impact on salinity intrusion that sea-level rise, and tidal influence had an impact (although smaller) on salinity intrusion.

The Cape Fear River located in North Carolina, USA is 307 km long. A study was conducted on the river and estuary that the river led into, to explore their hydrodynamic behaviour and investigate the relationship between salinity intrusion and discharge using field measurements and different regression models (Becker et al., 2010). The estuary has semi-diurnal tides with a range of 1.3 m, and ranges from partially mixed to well mixed. Their results showed that the tidal variation had effects on the salinity structure within the estuary. During low flows the estuary was well-mixed at the mouth and stratified mid estuary and further upstream. Stratification increases during ebbing tides and breaks down during flooding tides (Becker et al., 2010). They found that the strength of the river flow is important in determining the salinity structure. Density driven baroclinic circulation is associated with the horizontal density gradient which resulted from the two inputs of fresh and salt water. The baroclinic circulation increases stratification, and the salinity structure changes depending on the relative strength of the river flow and tidal flow forcing a momentum balance (Becker et al., 2010). Turbulence differences between flood and ebb tides may also control dynamics of the salt intrusion. Tidal straining causes changes in stratification due to vertical shear and density gradients. There is usually more stratification during the ebb tide because the river flow is stronger than the saltwater, and less stratification during flooding tides (Becker et al., 2010). This tidal straining can be seen in my results on the field visits that measurements were also taken while travelling downstream with the ebbing tide. It can be seen in the results that stratification increases in March and April when the tide is flowing back out of the estuary, compared to hightide, when the estuary is mixed.

The Cape Fear River estuary showed evidence of tidal straining during low river flow conditions, weaker tidal forcing increases patterns of stratification, while increased tidal forcing decreased stratification and had an increase in mixing. Stronger mixing resulted in stronger horizontal salinity gradients, and salinity intruded up to 55 km upstream (Becker et al., 2010). This result is consistent with what was observed during my studies, when the estuary was mixed, the salinity intrusion penetrated slightly further upstream than when the estuary was strongly stratified (salt wedge), and during high river flow conditions in the Cape Fear River estuary, there is quite a significant decrease in distance of salinity intrusion (Becker et al., 2010).

Chapter 6: Conclusions

This thesis presented a new set of field data of water properties from the lower Waihou River in the North Island of New Zealand. In particular, the observations were used to identify the extent and structure of the tidal salt intrusion. Subsequently, a previously calibrated numerical model of the system was adapted, and model predictions compared to observations. The major findings are summarised here:

1. In general, the 1 PSU isohaline reached around 7 – 12 km upriver of the mouth. Flows within the river were generally partially or well-mixed during flood tide, while the salinity intrusion took the form of a salt wedge during one survey. The river flow appeared to be the primary control on salinity intrusion length, while the tidal amplitude appeared to have a smaller effect. These conclusions differ to previous work which identified sea-level as the dominant driver for the salt intrusion. However, the relationship between river flow and salinity intrusion length and intensity of stratification was consistent with previous studies on rivers of similar size.
2. Turbidity was found to be linked with the salinity intrusion, as turbidity was larger within the sea-water front. Similarly, the difference between marine and fresh water also influenced the along-river distributions of pH, chlorophyll, dissolved oxygen, and fluorescent dissolved organic matter.
3. Overall, the numerical model did not well resolve the salt intrusion (either in vertical structure or extent). The extent of the intrusion was underpredicted compared to field measurements, which was attributed to the representation of mixing in the model. However, model performance improved with smaller values for the horizontal eddy diffusivity parameter.

6.1 Future research avenues

The observations taken in the present work were restricted to a relatively narrow range of conditions. Ideally future work would widen the parameter space. It would be beneficial to both undertake similar measurements across a larger range of river flows (including flood conditions) and across the full tidal range (including high spring tides which were not included in the present data set), and also to combine these moving surveys with some Eulerian (fixed point) time series measurements. Fixed point measurements of velocities would assist in resolving fluxes of material and may also shed light on whether some model deficiencies could be attributed to poor predictions of the velocity structure within the river.

While the present work identified several areas in which the model performed poorly, it would be instructive to perform a more detailed sensitivity analysis to the different parameters (which was outside of the scope of the present work), and also to include omitted processes such as winds and wave-driven mixing, particularly in the vicinity of the river mouth. If the model could be improved to the point at which the predictions of 3D hydrodynamics were considered reasonable, then it would be worth including morphological module and sediment transport processes.

References

Ahmed, T. (2020). *Distribution of Mine Waste Along the Waihou Rive Flood Plains* [MSc Thesis]. https://hdl.handle.net/10289/13344

Barbier, E. B., Koch, E. W., Silliman, B. R., Hacker, S. D., Wolanski, E., Primavera, J., Granek, E. F., Polasky, S., Aswani, S., Cramer, L. A., Stoms, D. M., Kennedy, C. J., Bael, D., Kappel, C. V., Perillo, G. M. E., & Reed, D. J. (2008). Coastal Ecosystem-Based Management with Nonlinear Ecological Functions and Values. *Science*, 319(5861), 321–323. https://doi.org/10.1126/science.1150349

Barlow, P. M., & Reichard, E. G. (2009). Saltwater intrusion in coastal regions of North America. *Hydrogeology Journal*, *18*, 247–260. https://doi.org/10.1007/s10040-009-0514-3

Becker, M. L., Luettich Jr., R. A., & Mallin, M. A. (2010). Hydrodynamic behavior of the Cape Fear River and estuarine system: A synthesis and observational investigation of discharge–salinity intrusion relationships. Estuarine, *Coastal and Shelf Science*, 88(3), 404–418. https://doi.org/10.1016/j.ecss.2010.04.022

Bogucki, D. J., Jones, B. H., & Carr, M.-E. (2005). Remote Measurements of Horizontal Eddy Diffusivity. *Journal of Atmospheric and Oceanic Technology*, 22(9), 1373–1380. https://doi.org/10.1175/jtech1794.1

Chappell, P. R. (2013). The Climate and Weather of Waikato 2nd edition. NIWA. https://niwa.co.nz/static/Waikato%20ClimateWEB.pdf

Clement, A. J. H., Nováková, T., Hudson-Edwards, K. A., Fuller, I. C., Macklin, M. G., Fox, E. G., & Zapico, I. (2017). The environmental and geomorphological impacts of historical gold mining in the Ohinemuri and Waihou river catchments, Coromandel, New Zealand. *Geomorphology*, *295*, 159–175. https://doi.org/10.1016/j.geomorph.2017.06.011

Costanza, R., d’Arge, R., de Groot, R., Farber, S., Grasso, M., Hannon, B., Limburg, K., Naeem, S., O’Neill, R. V., Paruelo, J., Raskin, R. G., Sutton, P., & van den Belt, M. (1997). The value of the world’s ecosystem services and natural capital. *Nature*, 387(6630), 253–260. https://doi.org/10.1038/387253a0

Dalrymple, R. W., Baker, E. K., Harris, P. T., & Hughes, M. G. (2003). Sedimentology and stratigraphy of a tide-dominated, foreland-basin delta (Fly River, Papua New Guinea). *SEPM (Society for Sedimentary Geology)*, 147–173. https://doi.org/10.2110/pec.03.76.0147

Déjeans, B. S. (2023). Lagrangian observations and numerical modelling of hydrodynamics, turbulence, and sediment transport in a tidal river [PhD Thesis].

Déjeans, B. S., Mullarney, J. C., & MacDonald, I. T. (2022). Lagrangian Observations and Modeling of Turbulence Along a Tidally Influenced River. *Water Resources Research*, 58(1). https://doi.org/10.1029/2020wr027894

Deltares systems. (2017). *Delft3D-FLOW User Manual Hydro-Morphodynamics*. Deltares.

Deltares systems. (2017). *Delft3D Functional Specifications*. Deltares.

Department of Conservation. (n.d.). *Whitebait - migratory galaxiids*. Www.doc.govt.nz. Retrieved October 31, 2022, from https://www.doc.govt.nz/nature/native-animals/freshwater-fish/whitebait-migratory-galaxiids/

Fish & Game Auckland/Waikato. (2022). *Lower Waihou River and feeder Streams*. Fish & Game. https://fishandgame.org.nz/auckland/freshwater-fishing-in-new-zealand/fishing-locations-and-access/trout-fishing-coromandel-ranges/lower-waihou-river-and-feeder-streams/

Geyer, W. R., & Farmer, D. M. (1989). Tide-Induced Variation of the Dynamics of a Salt Wedge Estuary. *Journal of Physical Oceanography*, *19*(8), 1060–1072. https://doi.org/10.1175/1520-0485(1989)019%3C1060:tivotd%3E2.0.co;2

GNS Science. (2011). Update of the national groundwater volume stock account: 1994 to 2020. In *Stats NZ*. https://www.stats.govt.nz/

GNS Science letter report prepared for Stats NZ Tatauranga Aotearoa

Gugliotta, M., Saito, Y., Nguyen, V. L., Ta, T. K. O., Nakashima, R., Tamura, T., Uehara, K., Katsuki, K., & Yamamoto, S. (2017). Process regime, salinity, morphological, and sedimentary trends along the fluvial to marine transition zone of the mixed-energy Mekong River delta, Vietnam. *Continental Shelf Research*, *147*, 7–26. https://doi.org/10.1016/j.csr.2017.03.001

Hicks, D. M., Shankar, U., McKerchar, A. I., Basher, L., Lynn, I., Page, M., & Jessen, M. (2011). Suspended sediment yields from New Zealand rivers. *Journal of Hydrology (New Zealand)*, *50*(1), 81–142. https://www.jstor.org/stable/43945015

Horstman, E. M., Lundquist, C. J., Bryan, K. R., Bulmer, R. H., Mullarney, J. C., & Stokes, D. J. (2018). The Dynamics of Expanding Mangroves in New Zealand. *Coastal Research Library*, *25*, 23–51. https://doi.org/10.1007/978-3-319-73016-5_2

Hume, T. M., Snelder, T., Weatherhead, M., & Liefting, R. (2007). A controlling factor approach to estuary classification. *Ocean & Coastal Management*, *50*, 605–929. https://doi.org/10.1016/j.ocecoaman.2007.05.009

Krvavica, N., Gotovac, H., & Lončar, G. (2021). Salt-wedge dynamics in microtidal Neretva River estuary. *Regional Studies in Marine Science*, *43*. https://doi.org/10.1016/j.rsma.2021.101713

Kurup, G. R., Hamilton, D. P., & Patterson, J. C. (1998). Modelling the Effect of Seasonal Flow Variations on the Position of Salt Wedge in a Microtidal Estuary. *Estuarine, Coastal and Shelf Science*, *47*(2), 191–208. https://doi.org/10.1006/ecss.1998.0346

La Croix, A. D., & Dashtgard, S. E. (2015). A Synthesis of Depositional Trends In Intertidal and Upper Subtidal Sediments Across the Tidal–Fluvial Transition In the Fraser River, Canada. *Journal of Sedimentary Research*, *85*(6), 683–698. https://doi.org/10.2110/jsr.2015.47

La Croix, A. D., Dashtgard, S. E., & MacEachern, J. A. (2019). Using a modern analogue to interpret depositional position in ancient fluvial-tidal channels: Example from the McMurray Formation, Canada. *Geoscience Frontiers*, *10*(6), 2219–2238. https://doi.org/10.1016/j.gsf.2019.03.008

Land Information New Zealand. (n.d.). *Waihou River and Firth of Thames*. Toitū Te Whenua Land Information New Zealand. Retrieved December 13, 2023, from https://www.linz.govt.nz/our-work/new-zealand-geographic-board/place-name-stories/place-names-cooks-voyages/waihou-river-and-firth-thames

Lesser, G. R., Roelvink, J. A., van Kester, J. A. T. M., & Stelling, G. S. (2004). Development and validation of a three-dimensional morphological model. *Coastal Engineering*, *51*(8-9), 883–915. https://doi.org/10.1016/j.coastaleng.2004.07.014

Liu, W.-C., Hsu, M.-H., Kuo, A. Y., & Kuo, J.-T. (2001). The Influence of River Discharge on Salinity Intrusion in the Tanshui Estuary, Taiwan. *Journal of Coastal Research*, *17*(3), 544–552. https://www.jstor.org/stable/4300207

Loisel, H., Mangin, A., Vantrepotte, V., Dessailly, D., Dat Ngoc Dinh, Philippe Garnesson, Sylvain Ouillon, Lefebvre, J.-P., Mériaux, X., & Phan, T. (2014). Variability of suspended particulate matter concentration in coastal waters under the Mekong’s influence from ocean color (MERIS) remote sensing over the last decade. *Remote Sensing of Environment*, *150*, 218–230. https://doi.org/10.1016/j.rse.2014.05.006

Manning, A. J., Langston, W. J., & Jonas, P. J. C. (2010). A review of sediment dynamics in the Severn Estuary: Influence of flocculation. *Marine Pollution Bulletin*, *61*(1), 37–51. https://doi.org/10.1016/j.marpolbul.2009.12.012

McBride, G., Reeve, G., Pritchard, M., Lundquist, C., Daigneault, A., Bell, R., Blackett, P., Swales, A., Wadhwa, S., Tait, A., & Zammit, C. (2016). The Firth of Thames and Lower Waihou River. *Synthesis Report RA2, Coastal Case Study. Climate Changes, Impacts and Implications (CCII) for New Zealand to 2100,* MBIE contract C01X1225. 50pp.

McDougall, T. J., & Barker, P. M. (2011). Getting started with TEOS-10 and the Gibbs Seawater (GSW) Oceanographic Toolbox. SCOR/IAPSO. http://www.teos-10.org/

McKeon, M. A., Horner-Devine, A. R., & Giddings, S. N. (2020). Seasonal changes in structure and dynamics in an urbanized salt wedge estuary. *Estuaries and Coasts*, *44*, 589–607. https://doi.org/10.1007/s12237-020-00788-z

McLeod, I. M., Parsons, D. M., Morrison, M. A., Le Port, A., & Taylor, R. B. (2012). Factors affecting the recovery of soft-sediment mussel reefs in the Firth of Thames, New Zealand. *Marine and Freshwater Research*, *63*(1), 78. https://doi.org/10.1071/mf11083

Naish, T. R., Nelson, C. S., & Hodder, A. P. W. (1993). Evolution of Holocene sedimentary bentonite in a shallow-marine embayment, Firth of Thames, New Zealand. *Marine Geology*, *109*(3-4), 267–278. https://doi.org/10.1016/0025-3227(93)90065-4

Norris, B. K., Mullarney, J. C., Bryan, K. R., & Henderson, S. M. (2019). Turbulence Within Natural Mangrove Pneumatophore Canopies. *Journal of Geophysical Research: Oceans*, *124*, 2263–2288. https://doi.org/10.1029/2018jc014562

Norris, B. K., Mullarney, J. C., Bryan, K. R., & Henderson, S. M. (2021). Relating millimeter-scale turbulence to meter-scale subtidal erosion and accretion across the fringe of a coastal mangrove forest. *Earth Surface Processes and Landforms*, *46*(3), 573–592. https://doi.org/10.1002/esp.5047

Nowacki, D. J., Ogston, A. S., Nittrouer, C. A., Fricke, A. T., & Van, P. D. T. (2015). Sediment dynamics in the lower Mekong River: Transition from tidal river to estuary. *Journal of Geophysical Research: Oceans*, *120*(9), 6363–6383. https://doi.org/10.1002/2015jc010754

NZ Fishing. (n.d.). *Waihou River*. Nzfishing.com. Retrieved December 13, 2023, from https://nzfishing.com/auckland-waikato/where-to-fish/waihou-river/

Poggioli, A. R., & Horner-Devine, A. R. (2015). The sensitivity of salt wedge to channel geometry. *Journal of Physical Oceanography*, *45*(12), 3169–3183. https://doi.org/10.1175/JPO-D-14-0218.1

Potter, B. (2007, February 28). *Estuaries*. NIWA. https://niwa.co.nz/education-and-training/schools/students/estuaries#whati

Rice, K. C., Hong, B., & Shen, J. (2012). Assessment of salinity intrusion in the James and Chickahominy Rivers as a result of simulated sea-level rise in Chesapeake Bay, East Coast, USA. *Journal of Environmental Management*, *111*, 61–69. https://doi.org/10.1016/j.jenvman.2012.06.036

Roche, B. (2022). *Sedimentologic and hydrodynamic trends along a modern fluvial to marine transition zone: Mud deposition in the Lower Waihou River, Aotearoa-New Zealand* [MSc Thesis]. https://hdl.handle.net/10289/15607

Roskoden, R. R., Bryan, K. R., Schreiber, I., & Kopf, A. (2019). Rapid transition of sediment consolidation across an expanding mangrove fringe in the Firth of Thames New Zealand. *Geo-Marine Letters*, *40*(2), 295–308. https://doi.org/10.1007/s00367-019-00589-9

Schofield, J. C. (1966). Waihou River. In *An Encyclopedia of New Zealand*. Te Ara - the Encyclopedia of New Zealand. http://www.teara.govt.nz/en/1966/waihou-river

Schueder, R., Pires, M. D., & Meijers, E. (2017). *Piako and Waihou River estuaries, New Zealand*. Deltares.

Sierra, J. P., Sánchez-Arcilla, A., González Del RíoJ., Flos, J., Movellán, E., Mösso, C., MartínezR., Rodilla, M., Falco, S., & Romero, I. (2002). Spatial distribution of nutrients in the Ebro estuary and plume. *Continental Shelf Research*, *22*(2), 361–378. https://doi.org/10.1016/s0278-4343(01)00061-9

Statistics New Zealand. (2006). *New Zealand Official Yearbook 2006* (B. Hutching, P. Cavanagh, & M. Smith, Eds.). David Bateman Ltd.

Swales, A., Bentley, S. J., & Lovelock, C. E. (2015). Mangrove-forest evolution in a sediment-rich estuarine system: opportunists or agents of geomorphic change? *Earth Surface Processes and Landforms*, *40*(12), 1672–1687. https://doi.org/10.1002/esp.3759

Swales, A., Bentley, S. J., Lovelock, C., & Bell, R. G. (2007). Sediment Processes and Mangrove-Habitat Expansion on a Rapidly-Prograding Muddy Coast, New Zealand. *Coastal Sediments '07*. https://doi.org/10.1061/40926(239)111

Victoria Government Department of Sustainability and Environment. (2008). *Native Fish in Coastal Victoria* [Poster]. ISBN 978-1-74208-878-5

Virginia Department of Conservation and Recreation. (2021, March). *Tidal Mesohaline and Polyhaline Marshes*. Retrieved January 4, 2024, from https://www.dcr.virginia.gov/natural-heritage/natural-communities/ncea4#:~:text=Mesohaline%20conditions%20comprise%20salt%20concentrations

Vundavilli, H., Mullarney, J. C., MacDonald, I. T., & Bryan, K. R. (2021). The interaction of buoyant coastal river plumes with mangrove vegetation and consequences for sediment deposition and erosion in a tidal environment. *Continental Shelf Research*, 222, 104417–104417. https://doi.org/10.1016/j.csr.2021.104417

Waikato Regional Council. (n.d.). *Environmental monitoring data for Waihou River*. Land, Air, Water Aotearoa (LAWA). Retrieved October 31, 2022, from https://www.lawa.org.nz/explore-data/waikato-region/river-quality/waihou-river/

Waikato Regional Council. (2023). *Our groundwater resource*. Waikato Regional Council. https://www.waikatoregion.govt.nz/environment/water/groundwater/groundwater-around-the-region/

Webster, J. G. (1995). Chemical processes affecting trace metal transport in the Waihou River and estuary, New Zealand. *New Zealand Journal of Marine and Freshwater Research*, *29*(4), 539–553. https://doi.org/10.1080/00288330.1995.9516686

Wells Aotearoa New Zealand. (n.d.). Wellsnz.teurukahika.nz. Retrieved January 5, 2024, from https://wellsnz.teurukahika.nz/wells/map

Zhang, Y., Ren, J., Zhang, W., & Wu, J. (2021). Importance of salinity-induced stratification on flocculation in tidal estuaries. *Journal of Hydrology*, *596*. https://doi.org/10.1016/j.jhydrol.2021.126063

Appendices

Table A.1: Observation point names, M and N coordinates from Delft 3D, X and Y coordinates and Longitude and Latitude coordinates.

Observation Point Name	**M**	**N**	**X**	**Y**	**Longitude**	**Latitude**
Tararu Tide	8	35	1823761.5	5887802.5	175 31 08.05297 E	37 07 45.84467 S
OP0	39	30	1825464.1	5883720	175 32 21.41696 E	37 09 56.72477 S
OP1	48	27	1826816.3	5882213	175 33 17.83809 E	37 10 44.40171 S
Kopu Bridge	55	30	1827549.1	5881068	175 33 48.78274 E	37 11 20.87912 S
OP2	63	30	1827286.6	5879826	175 33 39.50692 E	37 12 01.37292 S
OP3	76	32	1827908.6	5877245.5	175 34 07.55163 E	37 13 24.48179 S
Turua	79	29	1827832.5	5875989	175 34 05.84896 E	37 14 05.28196 S
OP4	93	31	1829328.5	5875354	175 35 07.20654 E	37 14 24.54650 S
OP5	106	35	1831114	5875587.5	175 36 19.34154 E	37 14 15.38938 S
OP6	137	26	1831236.4	5873347	175 36 26.80814 E	37 15 27.91018 S
OP7	224	25	1831595.8	5868353	175 36 46.98257 E	37 18 09.47721 S
Puke Bridge	395	29	1834581.9	5862445	175 38 54.87968 E	37 21 18.29300 S
Tirohia	754	29	1833447.3	5853247	175 38 19.26142 E	37 26 17.47881 S
Up-estuary	1978	30	1839127.8	5841279	175 42 24.17364 E	37 32 40.17635 S

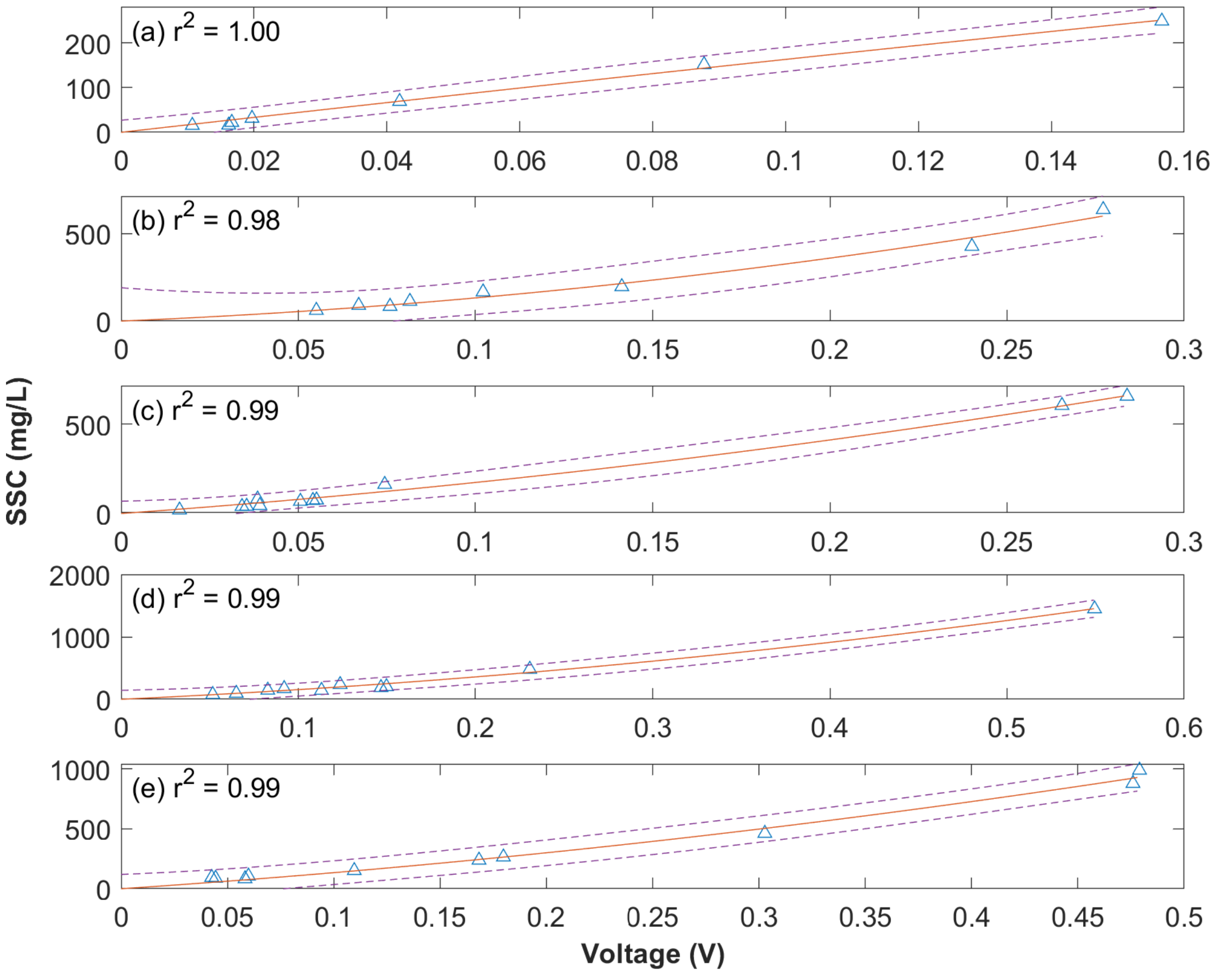

Figure A.1: Calibration curves of suspended sediment concentration from water samples collected during each field visit against CTD data voltage 1.

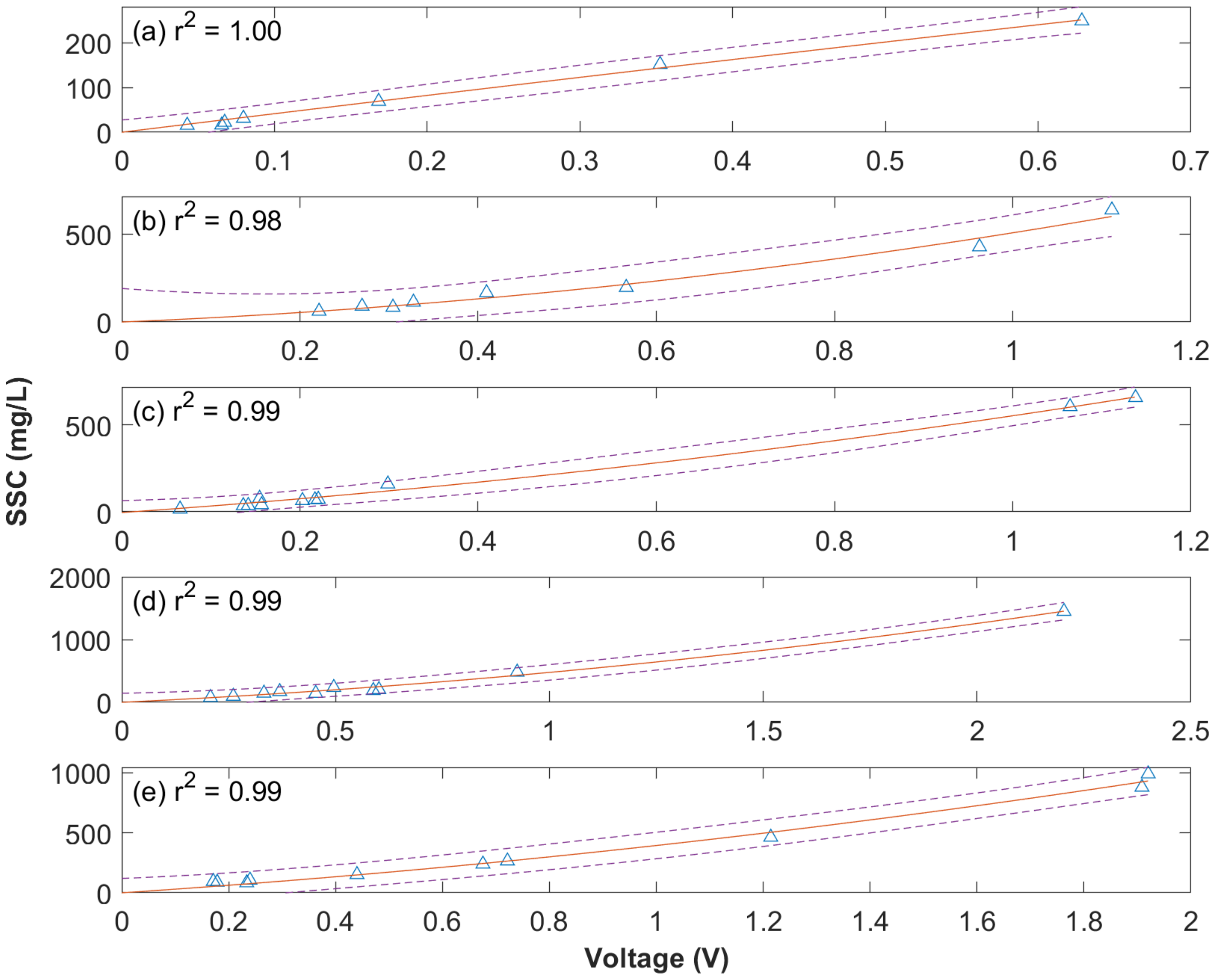

Figure A.2: Calibration curves of suspended sediment concentration from water samples collected during each field visit against CTD data voltage 2.

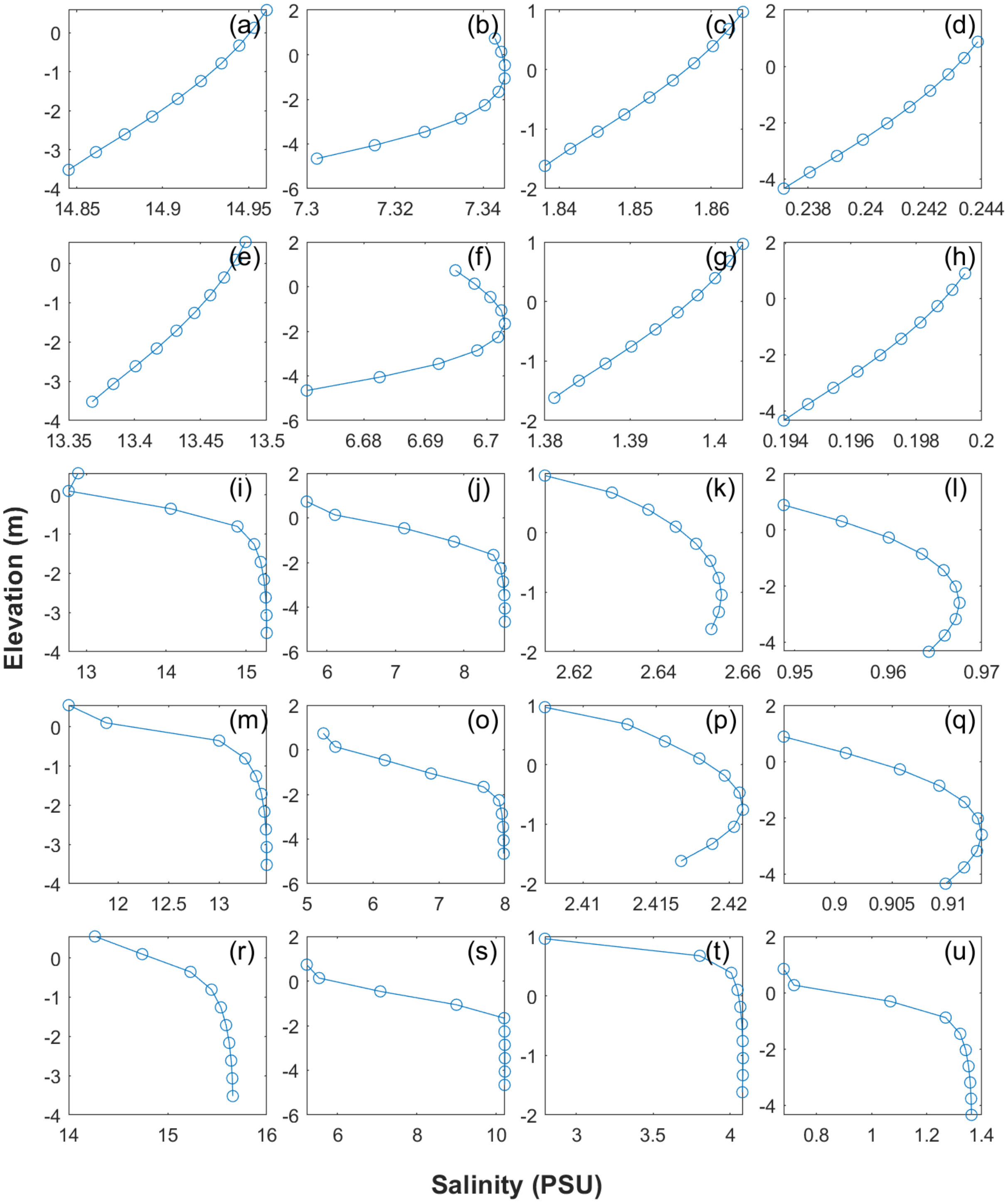

Figure A.3: September model data adjusted parameter salinity profiles. Corresponding with field location and time. Columns left to right: 2,000 m, 4,000 m, 6,000 m, 8,000 m from the mouth of the river. Rows top to bottom: model 3 (original model), model 8, model 9, model 10, model 11.

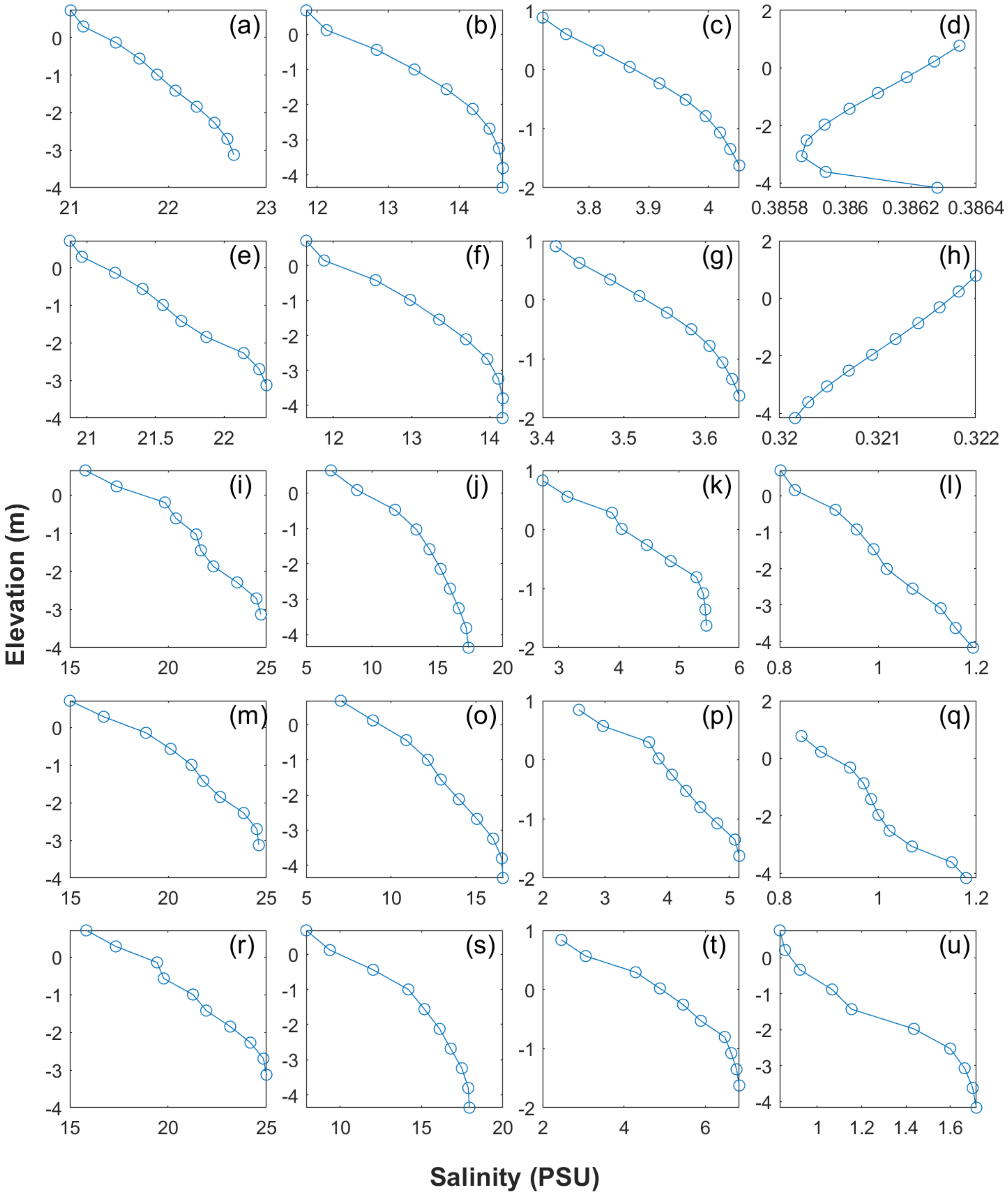

Figure A.4: September model data adjusted parameter salinity profiles. Time of profiles is that time of maximum salinity extent in the model, not corresponding with field location and time. Columns left to right: 2,000 m, 4,000 m, 6,000 m, 8,000 m from the mouth of the river. Rows top to bottom: model 3 (original model), model 8, model 9, model 10, model 11.